ABSTRACT

STUDIES OF TWO-PHASE FLOW WITH SOLUBLE SURFACTANT

by
Ryan Atwater

Numerical methods are developed for accurate solution of two-phase flow in the zero Reynolds number limit of Stokes flow, when surfactant is present on a drop interface and in its bulk phase interior. The methods are designed to achieve high accuracy when the bulk Péclet number is large, or equivalently when the bulk phase surfactant has small diffusivity.

In the limit of infinite bulk Péclet number the advection-diffusion equation that governs evolution of surfactant concentration in the bulk is singularly perturbed, indicating a separation of spatial scales. A hybrid numerical method based on a leading order asymptotic reduction in this limit, that scales out the Péclet number dependence, is adapted to resolve the drop interior flow, the bulk surfactant evolution, and the transfer of surfactant between the bulk and surface phases.

A more traditional numerical method that solves the full governing equations without the asymptotic reduction is also developed. This is designed to achieve high accuracy at large Péclet number by use of complex variable techniques that map the evolving drop shape and flow velocity onto the fixed domain of the unit disk, where a Chebyshev-Fourier spectral method is developed to resolve the bulk phase surfactant evolution.

Results of the two methods are compared for two-dimensional simulations of drop dynamics, when the drop is stretched or deformed in either a strain flow or in a shear flow. Recirculation of the interior flow and surfactant exchange on the interior of the drop induce more intricate dynamics than when bulk surfactant is present in the exterior phase.

STUDIES OF TWO-PHASE FLOW WITH SOLUBLE SURFACTANT

by
Ryan Atwater

A Dissertation
Submitted to the Faculty of
New Jersey Institute of Technology and
Rutgers, The State University of New Jersey – Newark
in Partial Fulfillment of the Requirements for the Degree of
Doctor of Philosophy in Mathematical Sciences

Department of Mathematical Sciences
Department of Mathematics and Computer Science, Rutgers-Newark

December 2020

APPROVAL PAGE

STUDIES OF TWO-PHASE FLOW WITH SOLUBLE SURFACTANT

Ryan Atwater

Michael Booty, Ph.D., Dissertation Co-Advisor — Date
Professor of Mathematical Sciences, NJIT

Michael Siegel, Ph.D., Dissertation Co-Advisor — Date
Professor of Mathematical Sciences, NJIT

Shahriar Afkhami, Ph.D., Committee Member — Date
Professor of Mathematical Sciences, NJIT

Linda Cummings, Ph.D., Committee Member — Date
Professor of Mathematical Sciences, NJIT

Pushpendra Singh, Ph.D., Committee Member — Date
Professor of Mechanical and Industrial Engineering, NJIT

BIOGRAPHICAL SKETCH

Author: Ryan Atwater

Degree: Doctor of Philosophy

Date: December 2020

Undergraduate and Graduate Education:

- Doctor of Philosophy in Mathematical Sciences,
  New Jersey Institute of Technology, Newark, NJ and Rutgers-Newark, NJ, 2020
- Master of Science in Mathematics,
  Towson University, Towson, MD, 2014
- Bachelor of Arts in Mathematics,
  University of Maryland, Baltimore County, Baltimore, MD, 2012

Major: Mathematical Sciences

I would like to thank my family for their endless encouragement and support. To my parents, Peter and Gail, there are no words that can describe how thankful I am for your advice, patience, and love throughout my academic journey; this dissertation is dedicated to you.

ACKNOWLEDGMENT

First and foremost, I would like to extend my deepest thanks to my dissertation advisors Professor Michael Booty and Professor Michael Siegel. The completion of this dissertation would not have been possible without their support, guidance, and patience.

I would also like to thank my committee members Professor Shahriar Afkhami, Professor Linda Cummings, and Professor Pushpendra Singh for their significant contributions and helpful suggestions.

I am deeply indebted to all of the professors with whom I had taken classes at NJIT, especially Professor David Shirokoff, Professor Brittany Hamfeldt, Professor Shidong Jiang, Professor Richard Moore, and Professor Amitabha Bose. Their excellence in teaching was instrumental in my development as a mathematician.

Thanks also to all my fellow graduate students whom I have gotten to know over the past five years. Thank you to Ryan Allaire, Brandon Behring, Chao Cheng, Yinbo Chen, Keyang Zhang, Yan Zhang, Guanyuan Liao, Zhongchen Lin, Subha Datta, and Ziyan Guo for sharing both the joys and the struggles of graduate life with me.

Finally, I would like to thank the Department of Mathematical Sciences that granted me a teaching assistantship to help fund my education. This work was supported in part by National Science Foundation grants DMS-1412789 and DMS-1909407.

TABLE OF CONTENTS

TABLE OF CONTENTS
(Continued)

Chapter **Page**

LIST OF TABLES

Table **Page**

LIST OF FIGURES

Figure **Page**

LIST OF FIGURES
(Continued)

Figure **Page**

LIST OF FIGURES
(Continued)

Figure **Page**

LIST OF FIGURES
(Continued)

Figure **Page**

CHAPTER 1

INTRODUCTION

The word surfactant is a contraction of surface active agent, but it means specifically a chemical compound or substance that reduces the surface tension between two phases that are immiscible, or do not mix. The immiscible phases could be liquid-liquid, such as oil and water, liquid-gas, such as water and air, or liquid-solid, such as a drop of water on glass. The most common context in practice and the one thought of here is liquid-liquid.

The molecular structure of a typical surfactant is amphiphilic, meaning that its molecule has two distinct components or ends. One component is a relatively small polar head group. It has an electrostatic dipole moment, similar to a water molecule, and the polar head is termed hydrophilic because this end of the surfactant molecule is attracted to other polar molecules such as water or a similar aqueous phase. The other end is a relatively long, large hydrocarbon chain or tail that is attracted to the similar hydrocarbon molecular structure of oils and is repelled by a polar aqueous phase, so that it is termed hydrophobic. The amphiphilic structure of a surfactant molecule means that it is energetically favored or inclined to be at the interface between an aqueous phase and an immiscible hydrocarbon phase.

It is the dissimilar molecular structure of polar aqueous and non-polar oil phases that leads to their being immiscible or distinct in the first place, with a surface or interface between them that has an energy barrier that is difficult for molecules to cross by, for example, excess thermal kinetic energy. The energy barrier between immiscible phases manifests itself physically as surface tension. The presence of surfactant molecules that straddle or sit across an interface lowers the height of the energy barrier and reduces surface tension.

Many surfactants are synthesized or man-made but they also occur in nature. Some surfactants are chemically toxic but others are benign. The most common domestic surfactants are used in detergents or soaps, where they enable dispersal or removal of aliphatic compounds and other components. One such domestic surfactant is sodium dodecyl sulfate (or sodium lauryl sulfate), which is also present in low concentrations in toothpaste and other products and enables them to foam during use. Surfactants are used as emulsifiers to maintain suspensions of oil in water or water in oil, they are used in the processing of foods, and to prevent coagulation and separation of the components of polymers in water-based paint. They are used to disperse oil spills in the environment and to improve oil extraction from the ground. Pulmonary surfactant occurs naturally and plays an important role in maintaining the lungs' ability to absorb oxygen, so much so that it is classified by the World Health Organization as an essential medicine. Chemically similar surfactants are sometimes used to aid in the opening of an infant's lungs in the first moments after childbirth. More generally, surfactants are in such widespread use that their world market value has been estimated at $30 billion in 2016, [28].

The subject of this dissertation is the role of surfactants in drop deformation when surfactant is present in its adsorbed phase on the drop surface or interface and in its dissolved or bulk phase in the drop interior. The study uses a combination of modeling, analysis, and numerical simulation that is carried out in 2D (i.e., two space dimensions) as an example of a proof of concept for a theoretical approach to the simulation of free and moving boundary problems when narrow diffusive boundary layers are present.

The fundamental cause for occurrence of a boundary layer here is the large size and shape of a typical surfactant molecule relative to the size of its host solvent molecules. Surfactant molecules have a size range from around 200 a.m.u to 2,000 a.m.u with many types at the higher weight end, whereas many oils are of 200 a.m.u.

or less, and an aqueous phase molecule is around 20 a.m.u. The mass and shape of surfactant molecules means that they have low mobility or diffuse very slowly in either the bulk or at an interface. If D denotes the diffusivity of a surfactant in water and a is a length scale, such as a typical drop radius, and U is a typical flow speed, then a typical diffusion speed is D/a, and the ratio of flow speed to diffusion speed Ua/D is the Péclet number Pe. In many applications, including those at the small scale of microfluidics, the Péclet number is of order 10^6 to 10^8.

In the bulk, surfactant is advected and diffuses as a passive scalar, and therefore satisfies an advection-diffusion equation, in which the inverse of the Péclet number Pe^{-1} is a dimensionless diffusion coefficient. The equation that governs the evolution of the bulk surfactant concentration C is $(\partial_t + \boldsymbol{u} \cdot \nabla)C = (Pe)^{-1}\nabla^2 C$. The diffusion coefficient Pe^{-1} is small, of order 10^{-6} to 10^{-8}, but multiplies the highest order spatial derivatives present in the Laplacian, ∇^2. The equation is therefore referred to as singularly perturbed, because narrow regions or layers may occur where the diffusion term, although multiplied by a small coefficient, is sufficiently large that diffusion can not be neglected relative to advection. This is a more or less mathematical explanation as to how spatially small regions of large spatial gradients, termed boundary layers, may develop.

During the deformation of a drop, which with its surroundings is almost completely incompressible, the drop volume is fixed but its surface area can change. If a drop is initially at rest then it has a spherical shape because of surface tension at its interface, and the concentration of surfactant on the drop interface and the concentration of surfactant in the bulk are in equilibrium. But the change in surface area during deformation puts the surface and bulk phase concentrations out of equilibrium. For example, over regions where the interface shrinks or contracts, the surface concentration increases relative to that in the bulk nearby, so that surfactant tends to desorb from the interface to go into solution in the bulk phase. However,

since it diffuses very slowly in the bulk this process is impeded, and large spatial gradients in the bulk phase concentration occur. The departure from equilibrium between the bulk and surface phase concentrations caused by deformation is the physical mechanism that induces a boundary layer to occur.

The type of layer structure that occurs is described here as a transition layer, in preference to boundary layer, since it occurs next to a free and moving interface, where the bulk concentration undergoes a rapid transition. The dynamics in the transition layer influence the concentration of surfactant that is on the interface, and hence the local surface tension and shape of the drop. The change in shape in turn implies a change in the surrounding flow, so that the flow field and surfactant fields are mutually coupled.

Two methods of solution are applied in this study. The hybrid method is based on a matched asymptotic treatment of the singularly perturbed advection-diffusion equation for the evolution of the bulk surfactant concentration C. This is a leading order model that is derived in the limit $Pe \to \infty$. It is hybrid in the sense that it combines asymptotic methods, introduced to resolve the spatial stiffness of the transition layer, with numerical methods. The second method is a traditional method in the sense that it solves the full advection-diffusion equation for C, without the asymptotic reduction. To enable solution at large values of Pe, the traditional method uses a conformal map to map the evolving drop boundary in the z-plane to the fixed unit circle in the ζ-plane, where high accuracy can be achieved because of the simpler fixed geometry.

The hybrid method was introduced in [4] and has been developed in later studies, such as [38, 39] and [37]. A difficulty that is encountered in the study of this dissertation, where bulk surfactant is present in the drop interior as opposed to its exterior, that was not encountered in other studies using the hybrid method, is the continual recirculation of the interior flow. This presents new challenges that are

both physical and technical. They are mentioned briefly here and are taken up in more detail throughout the dissertation.

As already noted, the influence of soluble or bulk surfactant on drop dynamics occurs via its exchange with the adsorbed or surface phase of surfactant on the interface, where it changes the interfacial surface tension. With exterior bulk surfactant present in a spatially uniform or constant ambient concentration, a Lagrangian or material fluid volume that approaches and passes adjacent to the interface always brings this same ambient value to the exchange process. During the exchange process the bulk concentration carried by the fluid volume evolves, and this continues until the volume begins to leave the neighborhood of the interface, at which point it carries a final bulk concentration, different from its initial ambient value, back into the bulk flow but never to return to interact again with the drop. This feature has been noted in simulations reported in the previously cited references [4, 37, 38, 39]. However, with interior bulk surfactant, when recirculation of the drop interior flow occurs, a fluid volume that leaves a neighborhood of the interface carrying a non-ambient bulk concentration acquired during an interaction with the interface can return at a later time to present this acquired, non-ambient concentration to a different part of the interface. Further, this process can repeat indefinitely. Description of this physical effect is taken up in Section 5.1 and sketched in Figure 5.1. Interior recirculation is particularly evident for a low-viscosity drop in a strain flow.

It turns out that with exterior bulk surfactant, in the $Pe \to \infty$ limit of the hybrid method, the fluid velocity only needs to be known on the interface in order to resolve the adjacent transition layer dynamics. A surface-based Stokes flow solver, such as a boundary integral method, can therefore be used, since there is no need to find off-surface data. This is not the case when bulk surfactant is present in the interior. A traditional method requires off-surface evaluation of the fluid velocity to

find the bulk surfactant concentration when it is present in either the exterior or interior phase. However, because of the physical mechanism for surfactant exchange with recirculating interior flow, as just described, the hybrid method also requires off-surface velocity data to track the bulk surfactant concentration on an interior drop 'core' that is diffusion-free at leading order as $Pe \to \infty$.

Evaluation of off-surface velocity data using a boundary integral equation Stokes flow solver is possible, by using surface data and the integral representation for the flow velocity, but it is prohibitively slow numerically. In two space dimensions, by using both a Goursat representation for Stokes flow and a conformal map from the evolving z-plane drop to the fixed ζ-plane unit disk, off-surface evaluation of the fluid velocity can be found by analytic continuation of the Goursat functions from the circle $|\zeta| = 1$ onto the disk interior $|\zeta| < 1$ using a fast Fourier transform (FFT). This is extremely quick and numerically stable. It is impeded slightly by the occurrence of a singularity of one of the Goursat functions on $|\zeta| = 1$, but this is circumvented by a procedure that is described in Section 3.5. A similar method for calculation of off-surface velocity data was introduced in [4], but it has been necessary to adapt and extend it here, and this is a novel feature of this study.

There is a long history of studies on drop deformation, both theoretical and experimental, that is too extensive to review here. The work of G. I. Taylor [32] was published in 1934, and reviews that contain references to work by many authors since then have been given by for example Rallison [27], Stone [31], and more recently by Anna [2]. Of these, many studies also include the influence of surfactants. A short book on aspects of interfacial fluid dynamics that contains many references to the role of surfactants is given by de Gennes et al. [8]

This dissertation is organized as follows. The governing equations and boundary conditions are given in Chapter 2, and Chapter 3 describes the complex variables techniques that are used. These include the Goursat representation for Stokes flow,

the boundary integral equation Stokes flow solver, the conformal map and its use in, for example, mapping the advection-diffusion equation for C. A reader familiar with the subject matter of these two chapters could enter the dissertation at Chapter 4, which summarizes the initial boundary value problem, presents the hybrid method, and describes the numerical implementation. The results of the numerical simulations are given in Chapter 5, which is a major component of this study. Conclusions are given in Chapter 6. The Appendices contain additional supporting details that are referenced at relevant points in the text.

CHAPTER 2

GOVERNING EQUATIONS

2.1 Governing Equations in Dimensional Form

The development of the governing equations, the interface and boundary conditions, and the geometrical configuration are given here. It begins with the equations for two-phase flow. Conservation of surface surfactant, i.e., adsorbed surfactant that is confined to the interface S, is introduced next, followed by conservation of bulk surfactant, i.e., dissolved surfactant away from the interface. Exchange of surfactant between the surface and bulk phases is described by interfacial boundary conditions, and the influence of surface surfactant on surface tension is described by a surface equation of state. Far-field conditions that give the imposed flow field and bulk surfactant distribution at infinity complete the description.

Conservation of Mass and Momentum. Let Ω_1 be the drop interior with fluid viscosity μ_1, Ω_2 be the unbounded drop exterior with fluid viscosity μ_2, and the interface of the drop be denoted by S. The flow is governed by the incompressible Stokes equations

$$\mu_i \nabla^2 \boldsymbol{u} = \nabla p, \quad \nabla \cdot \boldsymbol{u} = 0, \quad \boldsymbol{x} \in \Omega_i, \ i = 1, 2\,, \tag{2.1}$$

written in dimensional form. These are found in the zero Reynolds number or inertia-free limit of the Navier-Stokes equations for an incompressible Newtonian fluid.

Continuity of Velocity and the Kinematic Boundary Condition on S. The fluid velocity is continuous across S and evolves according to the kinematic boundary condition, so that

$$[\boldsymbol{u}]_1^2 = 0, \quad \frac{d\boldsymbol{x}}{dt} = (\boldsymbol{u} \cdot \boldsymbol{n})\boldsymbol{n}, \quad \boldsymbol{x} \in S\,, \tag{2.2}$$

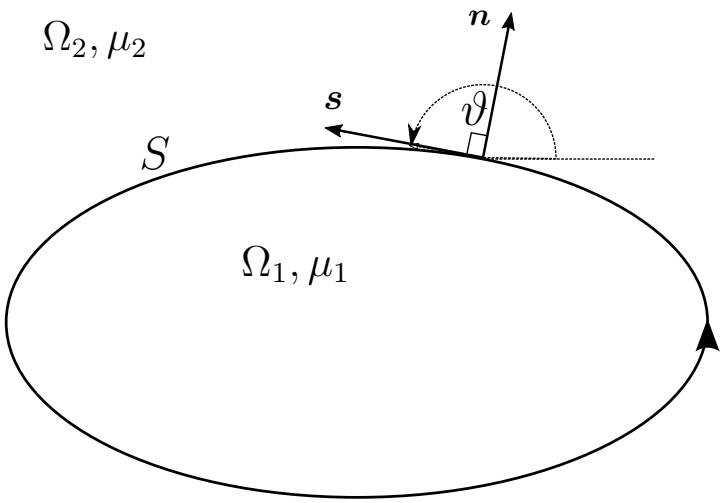

Figure 2.1 A fluid drop with viscosity μ_1 occupies the region Ω_1, it is surrounded by an immiscible fluid with viscosity μ_2 that occupies the unbounded region Ω_2, and S is the interface between the two fluids. The drop is deformed by an imposed far-field flow. The interface S is traversed in the counter-clockwise direction, it has unit tangent vector $\boldsymbol{s}$ and outward unit normal $\boldsymbol{n}$. The angle ϑ is measured counter-clockwise positive from the positive x_1-axis to the unit tangent vector, and if s is arc length on S then S has curvature $\kappa = \frac{\partial \vartheta}{\partial s}$.

where $[\cdot]_1^2$ denotes the jump or difference in a quantity across S, i.e., the exterior limit minus the interior limit, and $\boldsymbol{n}$ is the outward unit normal on S.

A sketch of the configuration is shown in Figure 2.1. For the most part, the geometrical configuration and analysis will be in two space dimensions.

Stress-Balance Boundary Condition on S. The net hydrodynamic traction on S due to the fluid on either side is equal to the net force due to surface tension on S. The equivalence of these forces is known as the stress-balance boundary condition, which is

$$[\boldsymbol{\sigma}]_1^2 \cdot \boldsymbol{n} = -(p_2 - p_1)\boldsymbol{n} + 2(\mu_2 \boldsymbol{e}_2 - \mu_1 \boldsymbol{e}_1) \cdot \boldsymbol{n} = \sigma\kappa\boldsymbol{n} - \nabla_s \sigma, \quad \boldsymbol{x} \in S\,. \tag{2.3}$$

Here, a subscript indicates the region, Ω_1 or Ω_2, from which $\boldsymbol{x}$ approaches S, i.e., it denotes the interior or exterior limit, $\boldsymbol{\sigma}$ is the stress tensor, e_i $(i = 1, 2)$ is the rate-of-strain tensor, σ is the surface tension at the interface, κ is the curvature of S

(or the sum of the principal curvatures in 3D), and $\nabla_s = \nabla - \boldsymbol{n}(\boldsymbol{n}\cdot\nabla)$ is the surface gradient operator.

On the right-hand side of equation (2.3), the first term, $\sigma\kappa\boldsymbol{n}$, is called the capillary stress and it acts in the direction normal to S. In the absence of surfactant, the surface tension σ is a constant, or a material constant for the two immiscible fluids in Ω_1 and Ω_2. In the second term, $\nabla_s\sigma$ is called the Marangoni stress and it acts tangentially to S. In the presence of surfactant, there is usually a gradient of surface surfactant concentration, which in turn causes a non-zero Marangoni stress. A derivation of the right-hand side of equation (2.3) is given in Appendix A.1, and the direction of the Marangoni stress is discussed in Appendix A.2.

Surface Equation of State. The surface tension σ depends on the surface concentration of surfactant Γ according to a surface equation of state $\sigma = \sigma(\Gamma)$. The nonlinear equation

$$\sigma = \sigma_c + RT\Gamma_\infty \ln\left(1 - \frac{\Gamma}{\Gamma_\infty}\right) \tag{2.4}$$

is often used, and is described as a Langmuir-type surface equation of state [11], the Frumkin surface equation of state [6], or the Szyszkowski surface equation of state [18]. The linearized version, when $\Gamma \ll \Gamma_\infty$, is also used,

$$\sigma = \sigma_c - RT\Gamma\,. \tag{2.5}$$

Here, σ_c denotes the surface tension in the absence of surfactant or "clean" state, Γ_∞ is a theoretical maximum monolayer surface surfactant concentration, R is the gas constant and T is temperature.

Conservation of the Surface Concentration of Surfactant. The surface surfactant concentration Γ satisfies the conservation law

$$\left.\frac{\partial\Gamma}{\partial t}\right|_n + \nabla_s\cdot(\Gamma\boldsymbol{u}_s) + \Gamma\kappa u_n = D_s\nabla_s^2\Gamma \pm D\,\boldsymbol{n}\cdot\nabla C|_S\,, \quad \boldsymbol{x}\in S. \tag{2.6}$$

Here, the left-hand side is the time rate of change of the surface concentration Γ on a Lagrangian interface element, i.e., on an infinitesimal patch of material particles that lie on the interface for all time as the patch moves and deforms. In the three terms that make up the left-hand side, reading from left to right, the time derivative $\partial_t|_n$ is taken in the direction of the outward normal along the moving interface. The term $\nabla_s \cdot (\Gamma \boldsymbol{u}_s)$ describes the change in Γ due to advection along the interface with tangential fluid velocity $\boldsymbol{u}_s = \boldsymbol{u} - (\boldsymbol{u}\cdot\boldsymbol{n})\boldsymbol{n}$, and the term $\Gamma\kappa u_n$ describes the change in Γ due to the local change in area of an element of the interface that occurs when the interface is non-planar (i.e., $\kappa \neq 0$) and has a non-zero normal velocity component $u_n = \boldsymbol{u}\cdot\boldsymbol{n} \neq 0$. As in (2.3) κ is the curvature of S in 2D or the sum of the principal curvatures in 3D.

On the right-hand side of equation (2.6), the first term describes the change in Γ due to surface diffusion, where D_s is the surface diffusion coefficient and ∇_s^2 is the surface Laplacian or Laplace-Beltrami operator. The last term is the "surfactant exchange term" which describes the transfer of surfactant between the interface S, where it has surface concentration Γ, and the bulk in Ω_1 or Ω_2, where it has bulk or dissolved concentration C. The parameter D is the diffusivity of bulk surfactant. With the convention that $\boldsymbol{n}$ is the outward unit normal on S (i.e., pointing from the interior Ω_1 to the exterior Ω_2), the sign that multiplies the surfactant exchange term is $+$ for bulk surfactant in Ω_2 and $-$ for bulk surfactant in Ω_1.

Conservation of Bulk Surfactant. Away from the interface, in Ω_1 and Ω_2, surfactant is advected with the flow and diffuses as a passive scalar with diffusivity D and bulk concentration C that satisfies

$$\frac{\partial C}{\partial t} + \boldsymbol{u}\cdot\nabla C = D\nabla^2 C, \quad \boldsymbol{x} \in \Omega_1 \text{ or } \Omega_2\,. \tag{2.7}$$

Bulk-Interface Exchange of Surfactant. The exchange of surfactant between the bulk and the interface satisfies the boundary condition

$$\pm D\,\boldsymbol{n}\cdot\nabla C|_S = \kappa_a(\Gamma_\infty - \Gamma)C|_S - \kappa_d\Gamma\,, \quad \boldsymbol{x}\in S\,. \tag{2.8}$$

The basis for this phenomenological relation is explained in detail in [11] and in the review [6]. Both sides of the relation express the surfactant exchange flux, which has dimensions moles per unit area per unit time (i.e., mol $L^{-2}T^{-1}$). The left-hand side is the Fick's law diffusive flux of bulk surfactant at the interface, where, as noted after (2.6), since $\boldsymbol{n}$ is the outward unit normal on S, the sign is + when bulk surfactant is present in Ω_2 and − when it is present in Ω_1. This is equal to, on the right-hand side, the rate of adsorption onto the interface minus the rate of desorption from the interface. The rate of adsorption depends on the availability of bulk surfactant at the interface, where the concentration is $C|_S$, and the availability of surface area that is not occupied by surface surfactant, which is proportional to $\Gamma_\infty - \Gamma$. The adsorption rate is modeled as the product of these two quantities times an adsorption coefficient, κ_a. The rate of desorption from the interface is assumed to be independent of the adjacent bulk concentration and to depend linearly on the surface concentration Γ with a rate constant κ_d of dimensions T^{-1}.

Initial and Far-Field Conditions. The initial distribution of bulk surfactant is assumed to be spatially uniform, with the bulk and interface surfactant concentrations in equilibrium, and the flow is started impulsively from rest.

When surfactant is present only in the drop interior Ω_1, and the initial bulk surfactant concentration there is C_0, the initial conditions are

$$\boldsymbol{u}(\boldsymbol{x},0) = \boldsymbol{0}\,, \quad p = \begin{cases} p_2 & \boldsymbol{x}\in\Omega_2 \\ p_2 + \sigma_0/a & \boldsymbol{x}\in\Omega_1 \end{cases}, \tag{2.9a}$$

$$C(\boldsymbol{x},0) = C_0\,,\ \Gamma(\boldsymbol{x},0) = \Gamma_0 = \frac{\Gamma_\infty\kappa_a C_0}{\kappa_d + \kappa_a C_0}\,. \tag{2.9b}$$

The expression for $\Gamma(\boldsymbol{x}, 0)$ follows since the surfactant exchange rate in equation (2.8) is zero in equilibrium, and a 0-subscript denotes initial values which are also related by the surface equation of state. If surfactant is present in the exterior Ω_2, the initial bulk concentration is equal to the constant value in the far-field, i.e., as $|\boldsymbol{x}| \to \infty$.

The flow field and drop deformation are driven by an imposed linear velocity field. In the reference frame of the drop, which is centered at $\boldsymbol{x} = \boldsymbol{0}$, the fluid velocity at infinity, or far-field flow, consists of this imposed linear velocity field plus a correction that decays far from the drop and accounts for the disturbance caused by the drop's presence. Since the flow is incompressible, i.e., $\nabla \cdot \boldsymbol{u} = 0$, the most general flow field that is linear in $\boldsymbol{x}$ can be expressed by a matrix that has zero trace. This gives the far-field condition for the velocity,

$$\boldsymbol{u}(\boldsymbol{x}, t) \to \boldsymbol{u}_\infty = \begin{pmatrix} Q & B + G/2 \\ B - G/2 & -Q \end{pmatrix} \cdot \boldsymbol{x} + \mathcal{O}(|\boldsymbol{x}|^{-2}) \quad \text{as} \quad |\boldsymbol{x}| \to \infty \,. \tag{2.10}$$

The parameters Q and B define the symmetric part of the matrix and therefore correspond to pure strains: Q, with flow $Q(x_1, -x_2)$, has principal axes or eigenvectors $\boldsymbol{e}_1 = (1, 0)$ and $\boldsymbol{e}_2 = (0, 1)$, and B, with flow $B(x_2, x_1)$, has principal axes $(1, 1)$ and $(1, -1)$. The parameter G, with flow $G/2(x_2, -x_1)$, is a rotation (clockwise for $G > 0$) with vorticity $\boldsymbol{\omega} = \nabla \times \boldsymbol{u} = -G\boldsymbol{e}_3$. The remainder term in equation (2.10) represents the far-field perturbation to the imposed linear flow that is caused by the presence of the drop, and for incompressible flow with no mass sources in 2D this is $\mathcal{O}(|\boldsymbol{x}|^{-2})$ as $|\boldsymbol{x}| \to \infty$.

2.2 Nondimensionalization

The length scale for nondimensionalization is the initial equilibrium drop radius, a, and the scale for fluid velocity is the capillary velocity $U \equiv \sigma_c/\mu_2$. Their ratio a/U is the scale for time, the scale for the pressure is $\mu_2 U/a$, and the scale for surface tension is the surfactant-free value σ_c. The surface surfactant concentration is made

nondimensional by the maximum monolayer surface concentration Γ_∞, and the bulk surfactant concentration is made nondimensional by a reference value C_∞, such as an ambient far-field value, or initial value, or the critical micelle concentration $C_{\rm cmc}$. Since the formation of micelles in the bulk [11] is not included in this study, the specific choice of reference value made here is more or less arbitrary. For ease of reference, the variable names and flow parameters (Q, B, G) with the scales for their nondimensionalization are listed in Table 2.1.

Table 2.1 The Independent Variables, the Dependent Variables, and the Imposed Flow Parameters, with the Scale for Their Nondimensionalization.

Variable	*Dimensional scale*	*Variable*	*Dimensional scale*
$\boldsymbol{x}$	a, initial drop radius	σ	σ_c, surfactant-free surface tension
$\boldsymbol{u}$	$U = \sigma_c/\mu_2$, capillary velocity	Γ	Γ_∞, maximum surface concentration
t	a/U	C	C_∞, reference bulk concentration
p	$\mu_2 U/a$	Q, B, G	$U/a = \sigma_c/\mu_2 a$

In nondimensional form, the governing equations contain a total of seven dimensionless groups. These are defined and listed in Table 2.2 together with the dimensionless version of the imposed flow parameters. Note that the dimensional and nondimensional version of the variables and parameters are denoted by the same

symbols: $\boldsymbol{x}, t, \boldsymbol{u}, p$, etc., and the interpretation of the dimensionless groups is described in more detail where they appear in the description of Section 2.3 below.

Table 2.2 The Dimensionless Groups and Flow Parameters.

Symbol and Definition	*Description*	*Symbol and Definition*	*Description*
Q, B, G	dimensionless imposed flow parameters	$Pe = Ua/D$	bulk Péclet number
$\lambda = \mu_1/\mu_2$	viscosity ratio	$J = DC_\infty/U\Gamma_\infty$	surfactant phase exchange coefficient
$E = RT\Gamma_\infty/\sigma_c$	elasticity number	$Bi = \kappa_d a/U$	Biot number
$Pe_s = Ua/D_s$	surface Péclet number	$K = \kappa_a C_\infty/\kappa_d$	equilibrium partition coefficient

2.3 Governing Equations in Nondimensional Form

In nondimensional form, the governing equations, interface boundary conditions and far-field conditions are:

The Stokes Flow Equations and Related Interface Boundary Conditions.

The equations for Stokes flow are

$$\lambda \nabla^2 \boldsymbol{u} = \nabla p, \quad \nabla \cdot \boldsymbol{u} = 0, \quad \boldsymbol{x} \in \Omega_1\,, \tag{2.11a}$$

$$\nabla^2 \boldsymbol{u} = \nabla p, \quad \nabla \cdot \boldsymbol{u} = 0, \quad \boldsymbol{x} \in \Omega_2\,, \tag{2.11b}$$

where $\lambda = \mu_1/\mu_2$ is the ratio of the interior to the exterior (reference) viscosity. The related interfacial boundary conditions on S are continuity of velocity, the kinematic condition and the stress-balance boundary condition, which respectively are

$$[\boldsymbol{u}]_1^2 = 0, \quad \frac{d\boldsymbol{x}}{dt} = (\boldsymbol{u}\cdot\boldsymbol{n})\boldsymbol{n}\,, \quad \boldsymbol{x}\in S\,, \tag{2.12a}$$

$$-(p_2-p_1)\boldsymbol{n} + 2(\boldsymbol{e}_2 - \lambda\boldsymbol{e}_1)\cdot\boldsymbol{n} = \sigma\kappa\boldsymbol{n} - \nabla_s\sigma, \quad \boldsymbol{x}\in S\,. \tag{2.12b}$$

These are the underlying flow equations and interface boundary conditions. For a given imposed far-field flow, if the surface tension σ is known for all $\boldsymbol{x}$ on S and $t > 0$ these give a closed well-posed problem for the flow field and the location of the moving interface or free boundary S. However, in the presence of surfactant, the surface tension depends on the local concentration of surfactant that is adsorbed on the interface, $\Gamma(\boldsymbol{x}, t)$.

Evolution of Surface Surfactant and the Surface Equation of State.

In nondimensional form, the Langmuir-type surface equation of state is

$$\sigma = 1 + E\ln(1-\Gamma)\,, \tag{2.13}$$

where the elasticity number E is defined in Table 2.2 and represents the sensitivity of the surface tension to changes in interfacial surfactant concentration. Typical values are in the range of 0.2 to 0.5. In the absence of surfactant on the interface, $\Gamma = 0$ and the surface tension takes the surfactant-free or "clean" constant value $\sigma = 1$.

In nondimensional form, the conservation law for evolution of the surface concentration Γ is

$$\left.\frac{\partial\Gamma}{\partial t}\right|_n + \nabla_s\cdot(\Gamma\boldsymbol{u}_s) + \Gamma\kappa u_n = \frac{1}{Pe_s}\nabla_s^2\Gamma \pm J\,\boldsymbol{n}\cdot\nabla C|_S\,, \quad \boldsymbol{x}\in S. \tag{2.14}$$

The parameters Pe_s and J are defined in Table 2.2. Of these, Pe_s is a surface Péclet number and $1/Pe_s$ is a dimensionless measure of the surface diffusivity of surfactant on the interface. Typical values of this dimensionless surface diffusivity are of the order of 10^{-6} or less. Under almost all circumstances, near-discontinuities or "shocks" in Γ do not occur, because the direction of the Marangoni stress term $\nabla_s\sigma$ in the stress-balance boundary condition (2.12b) inhibits their formation. This point is developed in Appendix A.2. As a result, the influence of surface diffusion can usually be neglected, with Pe_s set to infinity or $1/Pe_s = 0$.

The parameter $J = DC_\infty/U\Gamma_\infty$ in (2.14) is a measure of the change in Γ due to transfer or exchange of surfactant between the surface and bulk phases relative to its change due to advection on the interface, C is the local concentration of bulk surfactant, and $\boldsymbol{n}\cdot\nabla C|_S$ is its outward normal derivative on S. In the limit when $J = 0$, or when there is no surfactant present in the bulk phase so that $C = 0$, the influence of surfactant solubility is absent. The governing equations and interface conditions (2.11) to (2.14), with a given imposed flow, then form a closed problem for the flow and moving boundary position S. When $J > 0$ and $C > 0$ the term $J\,\boldsymbol{n}\cdot\nabla C|_S$ is a source term in the equation for evolution of Γ and represents the influence of surfactant solubility.

Recall that the sign that multiplies the surfactant exchange term is + for bulk surfactant in Ω_2 and − for bulk surfactant in Ω_1, and it is the latter case that is considered here.

If the interface has parameterization $\boldsymbol{x} = \boldsymbol{X}(\boldsymbol{\xi}, t)$ where $\boldsymbol{\xi} = (\xi_1, \xi_2)$ are parametric surface coordinates on S, the time derivative in the normal direction is given by $\partial_t|_n = \partial_t|_{\boldsymbol{\xi}} - \partial_t\boldsymbol{X}|_{\boldsymbol{\xi}}\cdot\nabla_s$. This has been explained in [36] and is taken up in Appendix C.2 at equation (C.19). When reference to the interface parameterization is included, the conservation law given by equation (2.14) becomes

$$\left.\frac{\partial\Gamma}{\partial t}\right|_{\boldsymbol{\xi}} - \left.\frac{\partial\boldsymbol{X}}{\partial t}\right|_{\boldsymbol{\xi}}\cdot\nabla_s\Gamma + \nabla_s\cdot(\Gamma\boldsymbol{u}_s) + \Gamma\kappa u_n = \frac{1}{Pe_s}\nabla_s^2\Gamma \pm J\,\boldsymbol{n}\cdot\nabla C|_S\,, \quad \boldsymbol{x}\in S. \tag{2.15}$$

Evolution of Bulk Surfactant and Bulk-Interface Exchange of Surfactant.

The conservation law for bulk or dissolved surfactant is

$$\frac{\partial C}{\partial t} + \boldsymbol{u} \cdot \nabla C = \frac{1}{Pe} \nabla^2 C \,, \quad \boldsymbol{x} \in \Omega_1 \text{ or } \Omega_2 \,, \tag{2.16}$$

The parameter $Pe = Ua/D$ is the bulk Péclet number. Since values of the bulk and surface diffusivities of surfactant are small and of the same order of magnitude [6], the dimensionless bulk diffusivity $1/Pe$, like the dimensionless surface diffussivity $1/Pe_s$, is of the order of 10^{-6} or less.

The interface boundary condition for exchange of surfactant between the bulk (dissolved) and the surface (adsorbed) phases is

$$\pm J \, \boldsymbol{n} \cdot \nabla C|_S = Bi \left(K(1-\Gamma) C|_S - \Gamma \right) \,, \quad \boldsymbol{x} \in S \,. \tag{2.17}$$

The role of the phase exchange parameter J and the choice of sign on the left-hand side of this relation are as described for equation (2.14). On the right-hand side, $Bi = \kappa_d a/U$ is the ratio of the surfactant exchange rate (or specifically, the rate of desorption, κ_d) and the flow rate U/a, and $K = \kappa_a C_\infty/\kappa_d$ is the ratio of the rate of adsorption to desorption of surfactant and is often referred to as an equilibrium partition coefficient.

As a boundary condition for the evolution equation (2.16) for C, (2.17) is a third kind or Robin type boundary condition in general. In commercial engineering processes, the drop size and flow rate are such that the Biot number can be very large. In the limit $Bi \to \infty$ with $J = O(1)$ and $K = O(1)$ fixed, the adsorption and desorption processes are in equilibrium, and the boundary condition is of Dirichlet type,

$$C|_S = \frac{\Gamma}{K(1-\Gamma)} \quad \boldsymbol{x} \in S \,. \tag{2.18}$$

This is the limit of diffusion-controlled transport [6, 11] in which the description of K as an equilibrium partition coefficient is more clear. In microfluidic contexts, the length scale a is smaller and the flow rate U/a is typically larger, so that the Biot number although possibly large is taken to be finite and the full, third kind boundary condition is kept. This is referred to as the diffusion-kinetic or mixed kinetic model. Values of K can vary greatly for different surfactants and fluid systems [6, 10].

Initial and Far-Field Conditions.

In nondimensional form, the initial equilibrium conditions are

$$\boldsymbol{u}(\boldsymbol{x},0)=\boldsymbol{0}\,,\quad p=\begin{cases} p_2 & \boldsymbol{x}\in\Omega_2 \\ p_2+\sigma_0 & \boldsymbol{x}\in\Omega_1 \end{cases}, \tag{2.19a}$$

$$C(\boldsymbol{x},0)=C_0\,,\ \Gamma(\boldsymbol{x},0)=\Gamma_0=\frac{KC_0}{1+KC_0}\,, \tag{2.19b}$$

where the initial values C_0 and Γ_0 are related by (2.13).

The imposed flow at infinity remains formally unchanged, that is,

$$\boldsymbol{u}(\boldsymbol{x},t)\to\boldsymbol{u}_\infty=\begin{pmatrix} Q & B+G/2 \\ B-G/2 & -Q \end{pmatrix}\cdot\boldsymbol{x}+O(|\boldsymbol{x}|^{-2})\quad\text{as}\quad|\boldsymbol{x}|\to\infty\,, \tag{2.20}$$

but where the parameters (Q,B,G) have been made nondimensional by the scale $U/a=\sigma_c/\mu_2 a$ noted in table 2.1. Two specific examples that are standard or canonical, and can be set up readily in an experiment are:

(i) A pure strain or uniaxial extension, given when $B=G=0$, for which the vorticity is zero and Q is the capillary number, with dominant part

$$\boldsymbol{u}_\infty=Q(x_1,-x_2)\,. \tag{2.21}$$

(ii) A simple or linear shear flow, given when $Q=0$ and $B=G/2$. This is a combination of a pure strain ($B\neq 0$) and a rotation ($G\neq 0$), which has vorticity

$\boldsymbol{\omega} = \nabla \times \boldsymbol{u} = -G\boldsymbol{e}_3$ and dominant part

$$\boldsymbol{u}_\infty = G(x_2, 0)\,. \tag{2.22}$$

The sign for G in the matrix of (2.20) follows [39]; in [38] the sign of G is reversed.

To conclude this chapter, we revisit some comments that have already been made above. The presence of a small parameter that multiplies the highest order derivatives in an ordinary or partial differential equation implies that the equation is "singularly perturbed" and is an indication that its solution may, and typically does, contain near-discontinuities with respect to coordinates of the highest derivative. Expressions that are often used and are examples of a near-discontinuity are boundary layer, shock, or internal layer. Both equations for the evolution of surfactant, (2.14) for the surface concentration Γ and (2.16) for the bulk concentration C, are singularly perturbed, because the respective diffusivities or inverse Péclet numbers $1/Pe_s$ and $1/Pe$ are small. However, the direction of the Marangoni stress, which is toward regions of higher interfacial surface tension, tends to inhibit the formation of near-discontinuities in the surface concentration Γ, so that the surface diffusivity $1/Pe_s$ can usually be set to zero. This point is taken up further in Appendix A.2.

Neverthless, near-discontinuities in the bulk concentration can be expected to occur, especially when the drop undergoes deformation. The mechanism for this was pointed out in the Introduction and is restated here. During deformation, the surface area of a region or an element of material particles on the interface can change in time, that is, it is compressible - its surface area can either expand or contract. In the absence of surface diffusion and solubility effects, the right-hand side of equation (2.14) is zero and the total amount of surfactant on the element $\int_S \Gamma dS$ is conserved, so that the change in area causes a change in the surface concentration Γ, which tends to take it away from equilibrium with the local bulk concentration $C|_S$. This causes a near-discontinuity in C to form adjacent to the interface, with large gradients in

the direction normal to the interface, and for the gradient to be resolved the bulk diffusivity $1/Pe$ and diffusion term that it multiplies in equation (2.16) must be kept. The influence of surface diffusion and surfactant solubility both tend to restore local equilibrium between the surface and bulk surfactant concentrations.

CHAPTER 3

COMPLEX VARIABLE FORMULATION: THE STOKES FLOW SOLVER AND THE CONFORMAL MAP

3.1 Overview

Complex variable techniques are used in two components of this study. In the first component, the velocity field and pressure of Stokes flow are written in terms of a stream function that satisfies the biharmonic equation, with suitable boundary conditions, and in 2D this is solved by introducing a pair of complex Goursat functions [5]. The two Goursat functions in turn can be expressed as integrals of a single complex density over the fluid boundaries. The stress-balance boundary condition at the fluid-fluid interface then requires that the density satisfies a particular Fredholm second kind integral equation, which is referred to as a Sherman-Lauricella integral equation. This Sherman-Lauricella formulation provides the basic Stokes flow solver for flow without surfactant. Since it is a surface-based solver, it can readily be adapted to include the effects of surfactant that is adsorbed on the interface, or insoluble. It can then be adapted further, to include the effects of soluble or dissolved surfactant in the limiting $Pe \to \infty$ asymptotic model of the hybrid method, and this is a central topic of this dissertation.

To test the validity of the $Pe \to \infty$ hybrid method, a traditional method is developed together with or alongside it. The traditional method uses the same Sherman Lauricella Stokes flow and surface surfactant solvers as the hybrid method, but solves the full conservation law, equation (2.16), for the bulk surfactant concentration C including its bulk diffusion term at large but finite bulk Péclet number, $Pe < \infty$, without the asymptotic reduction of the $Pe \to \infty$ limit. When bulk surfactant is dissolved in the drop interior, the traditional method is therefore designed to solve equation (2.16) with the surfactant exchange boundary condition

(2.17) throughout the evolving drop interior Ω_1, and to enable comparison with the hybrid method, it must achieve high accuracy at large Pe. To achieve this accuracy on an evolving domain, a conformal map is introduced that maps Ω_1 onto the fixed interior of the unit disk, where the bulk concentration is found by a spectral method. Construction and use of the conformal map introduces a second application of complex variable techniques to this study, separate from the Sherman-Lauricella formulation.

The Sherman-Lauricella formulation and the conformal map are combined at one point in the traditional and hybrid methods. Since bulk surfactant is dissolved everywhere in the drop interior Ω_1, the fluid velocity $\boldsymbol{u}$ must be found at and away from the interface to resolve its evolution there. The velocity field is needed to solve the full advection-diffusion equation (2.16) at finite Pe for the traditional method, and it is needed to solve the reduced diffusion-free or transport only version of equation (2.16) for the $Pe \to \infty$ hybrid method. To find the velocity field away from the interface S the Goursat functions are continued analytically, via the confomal map, away from the boundary of the unit disk onto its interior, where the solution for C is constructed. The velocity field and bulk surfactant concentration can then be mapped back from the unit disk to the drop interior Ω_1 for visualization.

3.2 The Goursat Representation

This section is a review of fundamental background material that is included to make the presentation self-contained, and some of its results are needed in the development below. The material can be found in many places in the literature, for example [5] (pages 180-182) and [21], and the notation here closely follows that of [39].

All of the dependent variables and related quantities depend on time t as well as position $\boldsymbol{x}$ but, unless it is considered necessary, the time dependence is suppressed in this and other sections to make the presentation more concise.

In terms of 2D Cartesian coordinates (x_1, x_2), the Cartesian components of the velocity $\boldsymbol{u} = (u_1, u_2)$ can be expressed in terms of a stream function $\psi(x_1, x_2)$ by

$$(u_1, u_2) = (\partial_{x_2}\psi, -\partial_{x_1}\psi)\,, \tag{3.1}$$

which automatically satisfies the relation $\nabla\cdot\boldsymbol{u} = 0$ of the Stokes flow equations (2.11). The curl of the Stokes flow momentum equation then implies that

$$\nabla^4\psi = 0\,, \tag{3.2}$$

that is, ψ satisfies the biharmonic equation.

To construct the Goursat representation for $\psi(x_1, x_2)$ note that from equation (3.2) $\nabla^2\psi$ is a harmonic function, so that

$$\nabla^2\psi = Re\,(H(z))\,, \tag{3.3}$$

where $H(z) = P(x_1, x_2) + iQ(x_1, x_2)$ is an analytic function of $z = x_1 + ix_2$ with real and imaginary parts $P(x_1, x_2)$ and $Q(x_1, x_2)$. Introduce

$$f(z) = a(x_1, x_2) + ib(x_1, x_2) = \frac{1}{4}\int H(z)\,dz\,, \tag{3.4}$$

so that $f(z)$ is analytic with real and imaginary parts $a(x_1, x_2)$ and $b(x_1, x_2)$. Then, from the Cauchy-Riemann equations and the expression for $f(z)$ in terms of $H(z)$,

$$\frac{\partial a}{\partial x_1} = \frac{\partial b}{\partial x_2} = \frac{P}{4} \quad \text{and} \quad \frac{\partial a}{\partial x_2} = -\frac{\partial b}{\partial x_1} = -\frac{Q}{4}\,. \tag{3.5}$$

It can now be verified directly that $\psi - x_1 a - x_2 b = \psi - Re\,(\bar{z}f(z))$ is harmonic, so that it in turn can be written as $\psi - Re\,(\bar{z}f(z)) = Re\,(h(z))$ for an analytic function $h(z)$. This gives the Goursat representation for $\psi(x_1, x_2)$,

$$\psi = Re\,(\bar{z}f(z) + h(z))\,, \tag{3.6}$$

where an overbar denotes the complex conjugate. If

Since the primitive variables u and p, and physical quantities such as the vorticity and rate of strain tensor that are derived from them, can be written in terms of derivatives of the stream function ψ, see for example equation (3.1), these quantities can all be expressed in terms of a pair of analytic functions, referred to as the Goursat functions, $f(z)$ and $g(z) = h'(z)$. For example, the velocity components are given by

$$-u_2 + iu_1 = f(z) + z\overline{f'(z)} + \overline{g(z)}\,. \tag{3.7}$$

Expressions for the physical quantities in terms of the Goursat functions can be found in for example [21, 38], and are collected for reference in Appendix B.1.

3.3 The Sherman-Lauricella Integral Equation

Since the equations of Stokes flow and the interface boundary conditions are linear in the velocity $\boldsymbol{u}$ and the pressure p, both these dependent variables and the Goursat functions that are used to represent them can be decomposed into the sum of two parts, of which one corresponds to the imposed linear flow, which is itself an exact solution of the Stokes equations in the absence of the drop, and the other part corresponds to the modification to the flow caused by the presence of the drop. It is shown in Appendix B.2 (equations (B.27)) that the Goursat functions are defined on Ω_1 and Ω_2 by

$$f(z,t) = \frac{1}{2\pi i}\int_S \frac{\omega(\xi,t)}{\xi - z}d\xi + \frac{G}{4}z + H(t)\,, \tag{3.8a}$$

$$g(z,t) = \frac{1}{2\pi i}\int_S \frac{-\overline{\omega(\xi,t)}d\xi + \omega(\xi,t)\overline{d\xi}}{\xi - z} - \frac{1}{2\pi i}\int_S \frac{\overline{\xi}\omega(\xi,t)}{(\xi - z)^2}d\xi - (B + iQ)z - \overline{H(t)}\,. \tag{3.8b}$$

Here, $\omega(z,t)$ is the complex density, which is to be found. The integrals around the interface S that contain $\omega(z,t)$ and its complex conjugate correspond to the flow

induced by the presence of the drop, while the terms that are linear in z correspond to the imposed flow field.

The Goursat functions defined by equations (3.8) are analytic on Ω_1 and Ω_2 but are not given by analytic continuation across S from one domain to the other. To see this, let τ denote an arbitrary point on the contour S and let $z \to \tau^+$ denote the exterior limit as z approaches $\tau \in S$ from the exterior domain Ω_2, and let $z \to \tau^-$ denote the interior limit as z approaches $\tau \in S$ from the interior domain Ω_1. This notation and terminology follow that of Appendix B.2, where more details are given. Then from the definition (3.8a) of $f(z,t)$, it follows from the Plemelj formulae and equations (B.30) of Appendix B.2 that, as z crosses S from Ω_2 to Ω_1, $f(z,t)$ has a discontinuity of $-\omega(\tau,t)$. In contrast, from the definition (3.8b) of $g(z,t)$, the first integral has two components, of which the first has discontinuity $\overline{\omega(\tau,t)}$ and the second is continuous as z crosses S from Ω_2 to Ω_1 (see the first of equations (B.29a) and (B.29b) of Appendix B.2). However, the second integral of (3.8b) diverges as $z \to \tau^{\pm}$, so that the Goursat function $g(z,t)$ is singular on S.

The Sherman-Laricella integral equation for the density $\omega(z,t)$ is constructed from the stress-balance boundary condition (2.12b). Details of the construction are given in Appendices B.1 and B.2 and are summarized here. The stress exerted on S by the fluid in Ω_1 and Ω_2 is expressed in terms of the Goursat functions, see equation (B.19) and the text that follows it. The contributions of the fluid stress and surface tension to the net stress-balance are each found to be perfect derivatives with respect to the arc length s along S, per equations (B.19) and (B.21). Consequently, an integrated form of the stress-balance boundary condition is used, which is

$$\lim_{z\to\tau^+}\left\{f(z,t) - z\overline{f'(z,t)} - \overline{g(z,t)}\right\} - \lambda \lim_{z\to\tau^-}\left\{f(z,t) - z\overline{f'(z,t)} - \overline{g(z,t)}\right\} = \frac{1}{2}\sigma\frac{\partial\tau}{\partial s}\,, \tag{3.9}$$

as can be found at equation (B.22). Reading from left to right, the terms correspond to the stress exerted by the fluid in Ω_2 and Ω_1 on the left-hand side, and the surface

tension forces on the right-hand side. These represent physical quantities and are therefore regular in the limits $z \to \tau^{\pm}$, despite the non-analyticity of $f(z,t)$ and $g(z,t)$ across S, and this observation will be useful later, in Section 3.5.

When the fluid stress terms are expressed as integrals over S that contain the density ω via relations (3.8) (see the result at equation (B.28)) and the exterior and interior limits $z \to \tau^{\pm}$ are formed (see equations (B.31) and (B.33)) the Sherman-Lauricella integral equation at (B.36) is found, namely

$$\omega(z,t) - \frac{\beta}{2\pi i}\int_S \omega(\xi,t)\, d\ln\frac{\xi - z}{\overline{\xi} - \overline{z}} - \frac{\beta}{2\pi i}\int_S \overline{\omega(\xi,t)}\, d\frac{\xi - z}{\overline{\xi} - \overline{z}} - \beta(B - iQ)\overline{z} - 2\beta H(t) = -\frac{\gamma}{2}\sigma(\Gamma)\frac{\partial z}{\partial s}\,, \tag{3.10}$$

where β and γ are given in terms of the viscosity ratio λ as

$$\beta = \frac{1-\lambda}{1+\lambda}\,, \qquad \gamma = \frac{1}{1+\lambda}\,. \tag{3.11}$$

Rank Deficiency When $\lambda = 0$ and $H(t)$

The function $H(t)$ entered the analysis in finding the far-field flow and the behavior of the Goursat function $f(z,t)$ for large $|z|$ at equations (B.23) and (B.24) of Appendix B.2, from which it also enters the expression (B.26) for the Goursat function $g(z,t)$. The function $H(t)$ is arbitrary, in the sense that under the map $f \mapsto f + H(t)$ and $g \mapsto g - \overline{H(t)}$ the representation of all physical quantities such as the fluid velocity, pressure, and stress in terms of the Goursat functions is independent of the choice of $H(t)$.

In solving the integral equation (3.10) the function $H(t)$ can therefore be set to zero, $H(t) = 0$, with one exception. When the drop interior fluid is inviscid, so that $\lambda = 0$ with the parameters of definitions (3.11) set to $\beta = 1$ and $\gamma = 1$, the integral equation is rank deficient or not invertible unless a solvability condition is introduced

[24, 25]. The choice

$$H(t) = \frac{1}{2}\int_S \omega(\xi, t)\, ds \tag{3.12}$$

was introduced by Kropinski [19] to remove the rank deficiency, and it turns out that $H(t) \equiv 0$ as a consequence of the conservation of area of the interior region Ω_1.

The Fluid Velocity on S

The Sherman Lauricella formulation of Stokes flow is referred to as indirect because the dependent variable or solution of the corresponding integral equation is a density, from which the primitive variables such as the fluid velocity can be found. In a direct formulation the dependent variable of the integral equation is itself a primitive variable, which is usually the fluid velocity [26].

Instead of presenting it here, the expression for the fluid velocity on S in terms of the density $\omega(z, t)$ is given in Section 3.7, at equations (3.69) and (3.70), when describing the time update of the interface position and the equal arc length frame.

3.4 The Conformal Map From the Unit Disk $|\zeta| \leq 1$ to the Drop Interior $\Omega_1 \cup S$

The method that is adopted for construction of the conformal map is referred to as James's method [17] and the most detailed accounts of it that are available, although brief, have been given by Halsey [14] and in the book by Kythe [20] (pp. 279-283). A comment on the literature and on a similar method due to Theodorsen [33] is included at the end of this section, but this section is mostly concerned with the map construction.

In modulus-argument form, a general point in the z-plane is $z = \rho e^{i\phi}$ and a general point in the ζ-plane is $\zeta = re^{i\theta}$. James's method constructs a conformal map $z = w(\zeta, t)$ from a point $\zeta = e^{i\theta}$ on the disk boundary $|\zeta| = 1$ to a point $z = \rho(\theta, t)e^{i\phi(\theta,t)}$ on the evolving drop interface or contour S. The map is then

continued analytically so that it maps the unit disk $|\zeta| \leq 1$ onto the drop interior and interface $\Omega_1 \cup S$ for all time $t \geq 0$. Since the map is to be conformal, the derivative $\frac{\partial w}{\partial \zeta}$ exists and is non-zero on $|\zeta| \leq 1$. We follow a common practice, in which freedom of choice in the Riemann mapping theorem enables construction of a map that sends origin to origin, so that $w(0,t) = 0$, and positive real axis $Re(\zeta) > 0$ to positive real axis $Re(z) > 0$, so that $w'(0,t) > 0$ is real and positive, where a prime denotes the derivative $' = \frac{\partial}{\partial \zeta}$. The map is then unique. It is constructed by introducing an auxiliary function, which for James's method is

$$h(\zeta, t) = \ln \frac{\partial z}{\partial \zeta}\,, \tag{3.13}$$

or equivalently $h(\zeta, t) = \ln w'(\zeta, t)$, which is also analytic on the unit disk.

Application of the chain rule, written in modulus-argument form, shows that on the disk boundary $\zeta = e^{i\theta}$

$$\frac{\partial z}{\partial \zeta} = \frac{\partial z}{\partial \theta} \div \frac{d\zeta}{d\theta} = \left(\rho \frac{\partial \phi}{\partial \theta} - i \frac{\partial \rho}{\partial \theta}\right) e^{i(\phi - \theta)}\,, \tag{3.14}$$

so that from the definition (3.13) of the auxiliary function

$$h(\zeta = e^{i\theta}, t) = \ln \sqrt{\left(\rho \frac{\partial \phi}{\partial \theta}\right)^2 + \left(\frac{\partial \rho}{\partial \theta}\right)^2} + i \tan^{-1}\left(\frac{-1}{\rho} \frac{\partial \rho}{\partial \phi}\right) + i(\phi - \theta)\,. \tag{3.15}$$

This can be simplified by recalling that on S, $ds^2 = d\rho^2 + (\rho d\phi)^2$ where s denotes arc length, and $\tan \psi = \frac{-1}{\rho} \frac{\partial \rho}{\partial \phi}$, where ψ is the angle at a point on S measured counterclockwise positive from the azimuthal direction to the tangent with ϕ increasing. Hence,

$$\left|\frac{\partial z}{\partial \zeta}\right| = \frac{\partial s}{\partial \theta}\,, \; \arg\left(\frac{\partial z}{\partial \zeta}\right) = \psi + \phi - \theta\,, \tag{3.16a}$$

$$\text{and } h(\zeta = e^{i\theta}, t) = \ln \frac{\partial}{\partial \theta} s(\theta, t) + i(\psi(\theta, t) + \phi(\theta, t) - \theta)\,. \tag{3.16b}$$

A sketch showing the angle ψ is given in Figure 3.1. Now, since $h(\zeta, t)$ is analytic on $|\zeta| \leq 1$, its real part $u(r, \theta, t)$ and imaginary part $v(r, \theta, t)$ are conjugate harmonic functions on the unit disk, and equation (3.16b) implies that their boundary values are

$$u(1, \theta, t) = \ln \frac{\partial}{\partial \theta} s(\theta, t) \quad \text{and} \quad v(1, \theta, t) = \psi(\theta, t) + \phi(\theta, t) - \theta \,. \tag{3.17}$$

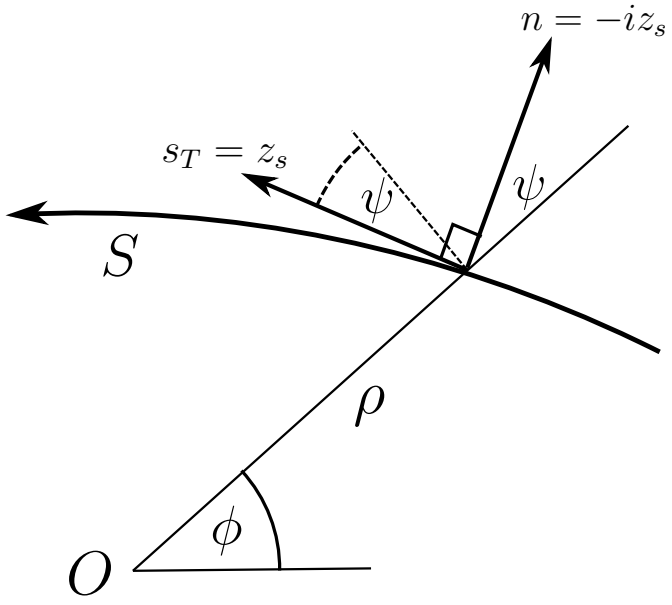

Figure 3.1 The interface S in the z-plane has polar equation $\rho = \rho(\phi)$. The angle ψ is measured counter-clockwise positive from the azimuthal direction $\boldsymbol{e}_\phi$ to the tangent vector, or equivalently from the radial direction $\boldsymbol{e}_\rho$ to the outward normal. The unit tangent and outward normal vectors have complex variable counterparts $s_T = \frac{\partial z}{\partial s}$ and $n = -i\frac{\partial z}{\partial s}$ respectively, where $z = \rho\, e^{i\phi}$ is a point on S.

In equation (3.17) both $u(1, \theta, t)$ and $v(1, \theta, t)$ are 2π-periodic functions of θ and therefore have Fourier series representations that are related by harmonic conjugation. Let

$$u(1, \theta, t) = a_0 + \sum_{n=1}^{\infty} a_n \cos n\theta + b_n \sin n\theta \,. \tag{3.18}$$

Then, to construct the conjugation operator K: $u(1, \theta, t) \mapsto v(1, \theta, t)$ we follow Delillo [9] and note first that the solution of the Dirichlet problem for $u(r, \theta, t)$ on the disk

interior is

$$u(r,\theta,t) = a_0 + \sum_{n=1}^{\infty} a_n r^n \cos n\theta + b_n r^n \sin n\theta \,. \tag{3.19}$$

The Cauchy-Riemann equations $\frac{\partial u}{\partial r} = \frac{1}{r}\frac{\partial v}{\partial \theta}$ and $\frac{\partial v}{\partial r} = -\frac{1}{r}\frac{\partial u}{\partial \theta}$ imply that the conjugation operator K maps eigenfunctions of the Laplacian so that

$$K\text{:}\;\; r^n \cos n\theta \mapsto r^n \sin n\theta \,, \tag{3.20a}$$

$$\text{and } K\text{:}\;\; r^n \sin n\theta \mapsto -r^n \cos n\theta \,, \tag{3.20b}$$

where constants of integration have been set to zero without loss of generality. Hence, on the disk interior and boundary the harmonic conjugate functions are

$$v(r,\theta,t) = Ku(r,\theta,t) = \sum_{n=1}^{\infty} a_n r^n \sin n\theta - b_n r^n \cos n\theta \,, \tag{3.21a}$$

$$\text{and} \qquad v(1,\theta,t) = Ku(1,\theta,t) = \sum_{n=1}^{\infty} a_n \sin n\theta - b_n \cos n\theta \,. \tag{3.21b}$$

The conjugation operator and its inverse are computed via fast Fourier transforms (FFTs).

In the discussion so far, time has only entered parametrically, but the map is updated at each time step by knowledge of the new interface position data. In the z-plane, let S be parameterized by $z = z(\alpha, t)$ where $\alpha \in [0, 2\pi)$ is the parameter. The interface position data at time $t + \Delta t$ consists of the location of N mesh points on S, and if these are chosen to be equally distributed in α,

$$z_{k,t+\Delta t} = z(\alpha_k, t + \Delta t), \quad \alpha_k = (k-1)h, \;\; k = 1, 2, \ldots N, \;\; \text{with } h = 2\pi/N. \tag{3.22}$$

In practice the parameter α is often taken to be the arc length s on S rescaled to lie in $[0, 2\pi)$, although other choices may be useful. Conversely, M mesh points are equally distributed around the fixed unit circle in the ζ-plane,

$$\zeta_j = e^{i\theta_j}, \quad \text{where } \theta_j = (j-1)\frac{2\pi}{M} \text{ and } j = 1, 2, \ldots M \,. \tag{3.23}$$

More details of the parameterization and time update of S are described in Section 3.7. Note that the mesh points $\{z_{k,t} : 1 \le k \le N\}$ of definition (3.22) are completely independent of the image of the mesh points $\{\zeta_j : 1 \le j \le M\}$ of definition (3.23) under the conformal map.

The map update consists of the following iterative procedure, which is similar to that described by Halsey [14]. First, an initial estimate is needed, which is the converged map data at the time t at the end of the previous time step, or the identity $z = \zeta$ for the first step:

1. The updated interface data $\{z_{k,t+\Delta t} : 1 \le k \le N\}$ of definition (3.22) is used to derive a set of curve-fit coefficients that at time $t + \Delta t$ give

$$\text{(i) polar angle vs. arc length } \phi = \phi(s, t + \Delta t) \text{ and} \tag{3.24a}$$

$$\text{(ii) polar distance vs. angle } \rho = \rho(\phi, t + \Delta t)\,. \tag{3.24b}$$

MATLAB's built-in cubic spline interpolation is used to find the curve-fit coefficients.

2. Use the current approximate values of $\left|\frac{\partial z}{\partial \zeta}\right|_j = \left(\frac{\partial s}{\partial \theta}\right)_j$ at the equispaced mesh points on the unit circle (3.23) to approximate the value s_j of s at the current map image of $\zeta_j = e^{i\theta_j}$. This is given by

$$s_j = \int_0^{\theta_j} \left|\frac{\partial z}{\partial \zeta}\right|_j d\theta\,, \tag{3.25}$$

and MATLAB's built-in trapezoidal rule is used for the integration.

3. Use the $t+\Delta t$ curve-fit of step (1) to determine the values ϕ_j and ρ_j that correspond to the current approximation of s_j. From this, construct the current approximate image $z_j = \rho_j e^{i\phi_j}$ of ζ_j, and the current approximate value of ψ_j from

$$\arg(\Delta z_j) \equiv \arg(z_{j+1} - z_j) = \psi_j + \phi_j + \frac{\pi}{2}\,. \tag{3.26}$$

4. Evaluate the current approximation of $\psi_j + \phi_j - \theta_j$, and use the inverse conjugation operator $K^{-1}v(1, \theta, t) = u(1, \theta, t)$ to update the current approximation of $\ln\left|\frac{\partial z}{\partial \zeta}\right|_j$.

That is, per equations (3.16) and (3.20), use FFTs to compute

$$\ln\left|\frac{\partial z}{\partial \zeta}\right|_j = K^{-1}(\psi_j + \phi_j - \theta_j)\,, \tag{3.27}$$

and exponentiate to update the current approximation of $\left|\frac{\partial z}{\partial \zeta}\right|_j = \left(\frac{\partial s}{\partial \theta}\right)_j$.

5. Repeat the procedure from steps (2) to (4) iteratively until the values of $\left|\frac{\partial z}{\partial \zeta}\right|_j$ converge.

Now the map $z = w(\zeta, t+\Delta t)$ is known in its discretized form $z_j = w(\zeta_j, t+\Delta t)$ on the unit circle $\zeta_j = e^{i\theta_j}$ via the converged data $z_j = \rho(\phi_j)e^{i\phi_j}$ where $\phi_j = \phi(\theta_j, t+\Delta t)$ is known for $1 \le j \le M$.

Analytic Continuation of The Map $z = w(\zeta, t)$ From $|\zeta| = 1$ Onto $|\zeta| \le 1$

Analytic continuation of a function from the unit circle $|\zeta| = 1$ onto the unit disk $|\zeta| \le 1$ can be achieved at no additional computational cost via Fourier transforms, since the coefficients of the complex Fourier series on the circle are exactly the coefficients of the Taylor series of the function when it is continued analytically onto the disk.

In the present context, the map $z = w(\zeta, t)$ is known on the unit circle $\zeta = e^{i\theta}$ for $\theta \in [0, 2\pi)$ and is necessarily 2π-periodic there. For its continuation onto $|\zeta| \le 1$ to be analytic, its complex Fourier series on the circle must be of the form

$$w(e^{i\theta}, t) = \sum_{k=0}^{\infty} c_k(t)e^{ik\theta} \quad \text{where} \quad c_k(t) = \frac{1}{2\pi}\int_0^{2\pi} w(e^{i\theta}, t)e^{-ik\theta}d\theta\,. \tag{3.28}$$

That is, for $k = -1, -2, \ldots$ the Fourier coefficients $c_k(t) = 0$ are all zero to avoid singularity at $\zeta = 0$.

In [9] Delillo points out that this result can be shown directly from the Cauchy integral formula. Namely, since $w(\zeta, t)$ is to be an analytic function of ζ in and on

$|\zeta| \leq 1$, for a point on the interior $|\zeta| < 1$,

$$w(\zeta,t) = \frac{1}{2\pi i}\int_{|\zeta'|=1} \frac{w(\zeta',t)}{\zeta'-\zeta}d\zeta' = \frac{1}{2\pi i}\int_{|\zeta'|=1} w(\zeta',t)\sum_{k=0}^{\infty}\left(\frac{\zeta}{\zeta'}\right)^k \frac{d\zeta'}{\zeta'}\,.$$

The parameterization $\zeta' = e^{i\theta}$ with $\theta \in [0, 2\pi)$ gives, on justifying interchange of the order of integration and summation,

$$z = w(\zeta,t) = \sum_{k=0}^{\infty}\left(\frac{1}{2\pi}\int_0^{2\pi} w(e^{i\theta},t)e^{-ik\theta}d\theta\right)\zeta^k = \sum_{k=0}^{\infty} c_k(t)\zeta^k\,. \tag{3.29}$$

Here, the Fourier coefficients $c_k(t)$ for $k = 0, 1, \ldots$ of definition (3.28) have been identified, and the last sum is the Taylor series of $w(\zeta, t)$ on $|\zeta| \leq 1$.

This result will be used in the analytic continuation of the Goursat functions in Section 3.5. Once the Fourier coefficients $c_k(t)$, $k = 0, 1, \ldots$, are known on the unit circle $\zeta = e^{i\theta}$ for $\theta \in [0, 2\pi)$ the continuation onto the disk $|\zeta| \leq 1$ is given simply by setting $\zeta = re^{i\theta}$ with $0 \leq r \leq 1$.

In the choice made earlier for uniqueness of the map: (i) It sends origin to origin, so that $w(0, t) = 0$ and hence $c_0(t) = 0$ in equations (3.28) and (3.29); (ii) $w'(0, t) > 0$, so that $c_1(t) > 0$. The map and auxiliary function are related by the equation $h(\zeta, t) = \ln \partial_\zeta z$, so that in terms of the map coefficients $\{c_k(t)\}$, $h(\zeta, t) = \ln c_1(t) + 2c_2(t)\zeta/c_1(t) + \mathcal{O}(\zeta^2)$ as $\zeta \to 0$. Then in terms of its real and imaginary parts $h(\zeta, t) = u(r, \theta, t) + iv(r, \theta, t)$, which implies that in expressions (3.18) and (3.19) the coefficient $a_0(t) = \ln c_1(t)$, and in expressions (3.21) the term $b_0(t) = 0$ is absent.

Comments on the Methods of James and Theodorsen

To conclude the section, in this synopsis the time dependence of the map and its image S are omitted. There are more accounts in the literature on conformal mapping of a method that is similar to James's method but which is due to Theodorsen [33],

and for Theodorsen's method there are also established bounds that appear to be sharp on the conditions for which it converges.

The purpose of both methods is the same: construction of a conformal map between a given plain simple smooth closed curve S, which is also called a Jordan curve, and the unit circle. As noted above equation (3.13), if the map $z = w(\zeta)$ between a curve S and the unit circle $|\zeta| = 1$ is to be conformal on the boundary curves and interior of the respective regions in the z and ζ-planes, and it is constrained to map origin to origin (i.e., $w(0) = 0$) and real axis to real axis (i.e., $w'(0) > 0$ is real and positive) then for a given curve S the map is unique. Therefore, between different methods, any difference concerns only the class of curves S for which the method can generate a solution, or converge, to the map.

James's method, as has just been shown, constructs the map $z = w(\zeta)$ from the auxiliary function $h(\zeta) = \ln(\frac{dz}{d\zeta})$ of equation (3.13), which leads to the relations (3.16) on the unit circle $\zeta = e^{i\theta}$. By way of contrast, Theodorsen's method constructs the map from the auxiliary function

$$h_{Th}(\zeta) = \ln\left(\frac{z}{\zeta}\right), \text{ which implies} \tag{3.30a}$$

$$h_{Th}(\zeta = e^{i\theta}) = \ln\rho(\theta) + i(\phi(\theta) - \theta) \tag{3.30b}$$

on the unit circle. The map constraints (i.e., $w(0) = 0$ and $w'(0)) > 0$) ensure that $h_{Th}(\zeta)$ is analytic in and on $|\zeta| \leq 1$, so that, for Theodorsen's method, the real part $u(1,\theta) = \ln\rho(\theta)$ and imaginary part $v(1,\theta) = \phi(\theta) - \theta$ of $h_{Th}(\zeta)$ on the unit circle are now the boundary values for the pair of conjugate harmonic functions on the unit disk.

Many accounts of Theodorsen's method, for example that of [5] (p. 177), express the conjugation operator K: $u(1,\theta) \mapsto v(1,\theta)$ as an integral operator on the unit circle that is constructed via the Cauchy integral formula (see, e.g., [5], p. 177 and p. 47).

This approach leads to Theodorsen's integral equation

$$\phi(\theta) - \theta = \frac{1}{2\pi} \int_0^{2\pi} \ln \rho(\phi(\theta')) \cot\left(\frac{\theta - \theta'}{2}\right) d\theta' \,, \tag{3.31}$$

in which, for given S, $\rho = \rho(\phi)$ is known, and the solution for $\phi = \phi(\theta)$ is to be found.

Delillo [9] applies a contraction mapping argument to the integral operator of equation (3.31) to show that a sufficient condition for an iterative scheme to converge to a solution for $\phi(\theta)$, and hence to a solution for the map, is that

$$\sup_{\phi \in [0, 2\pi)} \left| \frac{1}{\rho} \frac{d\rho}{d\phi} \right| < 1 \,. \tag{3.32}$$

This criterion for Theodorsen's method appears to be well-known, but an original derivation to cite for it has proved elusive. In geometric terms, it shows that convergence of Theodorsen's method is assured for Jordan curves S for which $|\psi| < \frac{\pi}{4}$, where the angle ψ was introduced immediately after equation (3.15) and is illustrated in Figure 3.1. The result appears to be sharp; an example from the same tutorial notes as well as computations of this study show that as the bound (3.32) is approached at any point of S the number of iterations needed to converge increases, and convergence fails if $|\psi| \geq \frac{\pi}{4}$ at any point.

Theodorsen's method is therefore not capable of constructing a conformal map to a curve S that is highly distorted from a circle, and for that reason it has not been used in this dissertation. James's method is capable of map construction for a much larger class of elongated and distorted curves S.

From a theoretical perspective, conjugation by the integral operator or by Fourier series are equivalent, and in the survey [9] conjugation by Fourier series is used for the practical numerical construction of maps. The study by Halsey [14] focuses explicitly on the comparison of Theodorsen's method with James's method for map construction by Fourier series conjugation, although in the context of airfoil mapping, where the exterior of S is mapped to the exterior of the unit disk. Halsey [14] notes

that James's method converges rapidly for examples of curves S that are sufficiently distorted from a circle that Theodorsen's method fails. The study also includes an extreme example of a "looped" curve S that is closed and can be traversed smoothly (i.e., it has a continuous, non-zero tangent vector) and which intersects itself, and is therefore not simple and not a Jordan curve, but which James's method can map successfully to the unit circle.

The literature on conformal mapping does not appear to contain any theoretical results on bounds for the convergence of James's method. It is conjectured in [14] that James's method enables map construction for a larger class of more distorted curves because (i) its auxiliary function (3.13) and conjugate harmonic parts (3.17) are expressed in terms of the intrinsic coordinates s and ψ of the image curve S, and (ii) the integral operator (3.25) tends to smooth out or reduce errors in the iterated values of $|\frac{dz}{d\zeta}|_j = \frac{ds}{d\theta}|_j$ prior to convergence. Recall again the auxiliary functions

$$h(\zeta) = \ln \frac{dz}{d\zeta} \quad \text{and} \quad h_{Th}(\zeta) = \ln\left(\frac{z}{\zeta}\right)$$

of James's and Theodorsen's methods, respectively. In James's method the argument $\frac{dz}{d\zeta}$ is the quotient of the tangent element dz at a point on S and its pre-image $d\zeta$, and both are readily expressed in terms of increments in the intrinsic coordinates on S and $|\zeta| = 1$, specifically

$$dz = ds\, e^{i(\psi+\phi+\frac{\pi}{2})} \quad \text{and} \quad d\zeta = d\theta\, e^{i(\theta+\frac{\pi}{2})}\,, \tag{3.33}$$

whereas the analog in Theodorsen's method is z/ζ, which is the quotient of the location of a point z on S and its pre-image. Other conformal mapping methods with the same purpose can be constructed, and one that is due to Friberg is mentioned in [5] (p. 177), which has auxiliary function $h_F = \ln(\frac{\zeta}{z}\frac{dz}{d\zeta})$. In chronological order, Theodorsen's method was introduced first, followed by Friberg's method, and later by James's method.

3.5 Analytic Continuation of the Goursat Functions to Find the Fluid Velocity on the Unit Disk $|\zeta| \leq 1$

To find the fluid velocity on the drop interior Ω_1 requires analytic continuation of the Goursat functions, which were defined earlier at equations (3.8) and are recalled here as

$$f(z,t) = \frac{1}{2\pi i}\int_S \frac{\omega(\xi,t)}{\xi - z}d\xi + \frac{G}{4}z + H(t)\,, \tag{3.34a}$$

$$g(z,t) = \frac{1}{2\pi i}\int_S \frac{-\overline{\omega(\xi,t)}d\xi + \omega(\xi,t)\overline{d\xi}}{\xi - z} - \frac{1}{2\pi i}\int_S \frac{\overline{\xi}\omega(\xi,t)}{(\xi - z)^2}d\xi$$
$$- (B + iQ)z - \overline{H(t)}\,. \tag{3.34b}$$

The density $\omega(z,t)$ is known on the evolving interface S, which is the boundary of Ω_1, since it is the solution of the Sherman-Lauricella integral equation. In principle, a direct evaluation of the contour integrals around S could therefore be implemented to find the Goursat functions at points $z \in \Omega_1$ but this would be prohibitively slow. If N computational mesh points are used for the discretization of S and M mesh points are introduced on Ω_1, where typically $M = \mathcal{O}(N^2)$, then $\mathcal{O}(MN)$ operations are required to evaluate the integrals around S at each point of Ω_1. Also, although $f(z,t)$ has an interior limit as $z \to \tau^-$ (i.e., as z approaches $\tau \in S$ from the interior domain Ω_1) which will be found below, $g(z,t)$ does not have an interior limit, since the second integral in its definition (3.34b) does not converge.

The procedure that is adopted for analytic continuation is first to evaluate $f(z,t)$ for $z \in S$ via definition (3.34a), and then to evaluate a combination of $f(z,t)$ and $g(z,t)$ that is bounded for $z \in S$ in order to extract the principal part of $g(z,t)$. These boundary values are then mapped onto the boundary $|\zeta| = 1$ of the unit disk in the ζ-plane using the conformal map $z = w(\zeta,t)$ of section 3.4 and analytic continuation onto the disk interior $|\zeta| < 1$ is achieved by fast Fourier transforms (FFTs). This is

computationally efficient and numerically stable. The map $z = w(\zeta, t)$ can be used to find the continuation of the Goursat functions onto Ω_1 in the z-plane, if needed.

The interior limit of the integral in the definition (3.34a) for $f(z,t)$ is given at equation (B.30b) of Appendix B.2. With z instead of τ as a representative point on S, this gives

$$f(z,t) = \frac{\omega(z,t)}{2} + \frac{1}{2\pi i}\fint_S \frac{\omega(\xi,t)}{\xi - z}d\xi + \frac{G}{4}z + H(t) \quad \text{for } z \in S\,, \tag{3.35}$$

where $\fint_S$ denotes a Cauchy principal value integral.

The combination $\overline{z}f'(z,t)+g(z,t)$ or its complex conjugate appears in expression (3.7) for the complex fluid velocity, which is now rewritten as

$$\overline{u} = u_1 - iu_2 = i(\overline{f(z,t)} + \overline{z}f'(z,t) + g(z,t))\,, \tag{3.36}$$

and it also appears in the fluid stress terms of equation (3.9). Since the fluid velocity components are continuous across S and the interior limit of $f(z,t)$ is at least bounded on S, the combination $\overline{z}f'(z,t) + g(z,t)$ is also bounded on S (but it is not analytic in a neighborhood of S since it contains a factor of $\overline{z}$). It follows from the definitions (3.34) that, after some re-arrangement (e.g., see identity (B.32b) of Appendix B.2)

$$\begin{aligned}\overline{z}f'(z,t) + g(z,t) = \frac{-1}{2\pi i}\int_S \frac{\overline{\omega(\xi,t)}\,d\xi}{\xi - z} + \frac{1}{2\pi i}\int_S \omega(\xi,t)\,d\left(\frac{\overline{\xi} - \overline{z}}{\xi - z}\right) \\ - (B + iQ)z + \frac{G}{4}\overline{z} - \overline{H(t)} \quad \text{for } z \in \Omega_1\,.\end{aligned} \tag{3.37}$$

To find the interior limit of this expression, with z as a general point on S, observe that, similar to forming the interior limit (3.35), the first integral on the right-hand side has a local contribution given by contour indentation around $z \in S$ per equation (B.30b), while the second integral is regular, as noted at equation (B.35), with both

results given in Appendix B.2. It follows that

$$\overline{z}f'(z,t)+g(z,t)=-\frac{\overline{\omega(z,t)}}{2}-\frac{1}{2\pi i}\oint_S\frac{\overline{\omega(\xi,t)}\,d\xi}{\xi-z}+\frac{1}{2\pi i}\int_S\omega(\xi,t)\,d\left(\frac{\overline{\xi}-\overline{z}}{\xi-z}\right)$$
$$-(B+iQ)z+\frac{G}{4}\overline{z}-\overline{H(t)}\quad\text{for } z\in S\,. \tag{3.38}$$

The result of equation (3.38) can also be found after some straightforward manipulation by combining equation (B.33) of Appendix B.2 for the interior limit of the fluid stress terms and equation (3.35) above.

The boundary data for $z\in S$ of equations (3.35) and (3.38) is now mapped onto the boundary $|\zeta|=1$ of the unit disk. That is,

$$f(z,t)\mapsto F(\zeta,t)\equiv f(w(\zeta,t),t)\,, \tag{3.39a}$$

$$\overline{z}f'(z,t)+g(z,t)\mapsto\quad\overline{w(\zeta,t)}\left(\frac{\frac{d}{d\zeta}F(\zeta,t)}{\frac{dw(\zeta,t)}{d\zeta}}\right)+g(w(\zeta,t),t)\,, \tag{3.39b}$$

on $|\zeta|=1$, which has parameterization $\zeta=e^{i\theta}$ for $\theta\in[0,2\pi)$. Analytic continuation onto the interior $|\zeta|<1$ is now straightforward and follows the procedure of [4]. That $F(\zeta,t)$ is analytic on $|\zeta|\le 1$ follows directly from the analyticity of $f(z,t)$ on $\Omega_1\cup S$ and the analyticity of $w(\zeta,t)$ on $|\zeta|\le 1$, so that $F(\zeta,t)$ has a Taylor series

$$F(\zeta,t)=\sum_{k=0}^{\infty}F_k(t)\zeta^k \tag{3.40}$$

about $\zeta=0$. On the boundary $|\zeta|=1$, the parameterization $\zeta=e^{i\theta}$ implies that $F(\zeta=e^{i\theta},t)$ is 2π-periodic in θ there, and therefore has the complex Fourier series representation

$$F(\zeta=e^{i\theta},t)=\sum_{k=0}^{\infty}F_k(t)e^{ik\theta}\quad\text{where}\quad F_k(t)=\frac{1}{2\pi}\int_0^{2\pi}F(\zeta=e^{i\theta},t)e^{-ik\theta}d\theta\,. \tag{3.41}$$

In other words, the known boundary data of equation (3.39a) gives the Fourier coefficients $\{F_k(t):k=0,1,2,\ldots\}$ of the series (3.41) which are also the coefficients

of the Taylor series (3.40). The procedure is well-posed or numerically stable, since it is directed from $|\zeta| = 1$ to $0 \leq |\zeta| = r < 1$, so that any error in the boundary data decreases with continuation onto the interior.

The derivatives $\frac{dF}{d\zeta}$, $\frac{dw}{d\zeta}$, and the complex conjugate $\overline{w(\zeta,t)}$ in the first group of terms on the right-hand side of equation (3.39b), that form the pre-image of $\overline{z}f'(z,t)$, can now be constructed in Fourier space directly from the Fourier series of $F(\zeta,t)$ and the map $w(\zeta,t)$ on $|\zeta| = 1$. They are then combined and subtracted to give boundary data on $|\zeta| = 1$ for the pre-image

$$G(\zeta,t) \equiv g(w(\zeta,t),t) \tag{3.42}$$

of the regular part of the Goursat function $g(z,t)$. Analytic continuation of $G(\zeta,t)$ onto $|\zeta| < 1$ then follows the same steps through equations (3.39a), (3.40), and (3.41) as described for the continuation of $F(\zeta,t)$, to give

$$G(\zeta,t) = \sum_{k=0}^{\infty} G_k(t)\zeta^k \quad \text{on } |\zeta| \leq 1\,, \tag{3.43a}$$

$$\text{where} \quad G_k(t) = \frac{1}{2\pi}\int_0^{2\pi} G(\zeta = e^{i\theta},t)e^{-ik\theta}d\theta\,. \tag{3.43b}$$

The pre-image of the fluid velocity in the ζ-plane can now be constructed. From the complex conjugate of expression (3.36), we have

$$u = u_1 + iu_2 = -i\left(F(\zeta,t) + w(\zeta,t)\frac{\overline{\partial_\zeta F(\zeta,t)}}{\overline{\partial_\zeta w(\zeta,t)}} + \overline{G(\zeta,t)}\right) \tag{3.44}$$

on $|\zeta| \leq 1$. Note that the real and imaginary parts of this expression are the Cartesian velocity components (u_1, u_2) at a point in the z-plane that has been mapped to the corresponding point $\zeta = w^{-1}(z,t)$ in the ζ-plane. In other words, the Cartesian velocity components on the drop interior Ω_1 are given by evaluating the right-hand side of equation (3.44) at (ζ,t) and mapping ζ back to z under the map $z = w(\zeta,t)$.

Computational overhead in constructing the velocity field can be reduced a little by recalling that the second integral on the right-hand side of the boundary data (3.38) is already known at each time step as the complex conjugate of an integral in the Sherman-Lauricella equation (3.10), specifically it is the second integral on the left-hand side of equation (3.10). Construction of the Cauchy principal value integrals in the boundary data of equations (3.35) and (3.38) is described in Appendix B.3.

To conclude this section, we observe that a useful check to verify the construction of the velocity components on the drop interior is to compare the fluid velocity $\boldsymbol{u} = (u_1, u_2)$ just inside the drop with its value at neighboring points that are on the interface S. The interface data is constructed separately, and is used for the time update of the evolving interface and the equal arc length coordinate frame.

3.6 Conservation of Bulk Surfactant on the Unit Disk $|\zeta| \leq 1$

Numerical solution of the initial boundary value problem for the bulk surfactant concentration C, for both the traditional method and for the hybrid method away from its transition layer, is carried out in the ζ-plane. This section describes transformation of the problem for C between the z-plane and the ζ-plane.

In the physical or z-plane, the evolution is governed by the advection-diffusion equation (2.16) which is

$$\frac{\partial C}{\partial t} + \boldsymbol{u} \cdot \nabla C = \kappa \nabla^2 C \,, \quad \boldsymbol{x} \in \Omega_1, \ t > 0 \,, \tag{3.45}$$

where $\kappa = Pe^{-1}$, and the boundary condition for bulk-surface surfactant exchange (2.17) which is

$$J\, \boldsymbol{n} \cdot \nabla C|_S = -\mathcal{F}(\boldsymbol{x}, t) \equiv -Bi \left(K(1-\Gamma) C|_S - \Gamma \right) \,, \quad \boldsymbol{x} \in S \,. \tag{3.46}$$

The initial condition that the bulk and surface surfactant concentrations are in equilibrium is given by setting the net exchange on the far right-hand side of equation

(3.67) to zero at $t = 0$, i.e., $C|_S(\boldsymbol{x}, 0) = \frac{\Gamma(\boldsymbol{x}),0}{K(1-\Gamma(\boldsymbol{x},0))}$. Here, κ and $\mathcal{F}$ have been introduced temporarily for convenience. The transformation occurs under the map of equation (3.29), namely

$$z = w(\zeta, t) = \sum_{k=0}^{\infty} c_k(t)\zeta^k \,, \tag{3.47}$$

or its inverse.

It is useful to alternate between 2D vector and complex representation, and the correspondence or equivalence of a quantity using either notation is denoted by $\leftrightarrow$. In the z-plane, position and fluid velocity are given by

$$\boldsymbol{x} = x_1\boldsymbol{e}_1 + x_2\boldsymbol{e}_2 \leftrightarrow z = x_1 + ix_2 \;\text{ and }\; \boldsymbol{u} = u_1\boldsymbol{e}_1 + u_2\boldsymbol{e}_2 \leftrightarrow u = u_1 + iu_2 \,, \tag{3.48}$$

where $\boldsymbol{e}_1$ and $\boldsymbol{e}_2$ are the standard Cartesian unit vectors of Cartesian coordinates (x_1, x_2) and have direction fixed or independent of position. Similarly, (u_1, u_2) are the Cartesian velocity components of $\boldsymbol{u}$. In the ζ-plane, position is denoted by (r, θ) polar coordinates, with

$$\text{standard unit vectors } \hat{\boldsymbol{e}}_r \text{ and } \hat{\boldsymbol{e}}_\theta \,, \text{ where } (r, \theta) \leftrightarrow \zeta = re^{i\theta} \tag{3.49}$$

and the polar standard unit vectors $\hat{\boldsymbol{e}}_r$ and $\hat{\boldsymbol{e}}_\theta$ depend on position.

The transformation is given by a change of variables between (x_1, x_2) and (r, θ) under the map. However, the map induces an orthogonal curvilinear coordinate system in the z-plane, with position $\boldsymbol{x} = \boldsymbol{x}(r, \theta)$ and increment

$$d\boldsymbol{x} = l_1 dr\boldsymbol{e}_r + l_2 d\theta\boldsymbol{e}_\theta = dx_1\boldsymbol{e}_1 + dx_2\boldsymbol{e}_2 \,, \tag{3.50a}$$

$$\text{where }\; \boldsymbol{e}_r = \frac{1}{l_1}\frac{\partial \boldsymbol{x}}{\partial r} \text{ with } l_1 = \left|\frac{\partial \boldsymbol{x}}{\partial r}\right|, \;\text{ and }\; \boldsymbol{e}_\theta = \frac{1}{l_2}\frac{\partial \boldsymbol{x}}{\partial \theta} \text{ with } l_2 = \left|\frac{\partial \boldsymbol{x}}{\partial \theta}\right| . \tag{3.50b}$$

Since the map is conformal, r and θ are orthogonal curvilinear coordinates in both the z-plane and the ζ-plane. In other words, the family of curves $\boldsymbol{x} = \boldsymbol{x}(r, \theta)$ with $r =$

constant, which are the image of circles $r =$ constant in the ζ-plane, are orthogonal everywhere to curves $\boldsymbol{x} = \boldsymbol{x}(r, \theta)$ with $\theta =$ constant, which are the image of rays $\theta =$ constant in the ζ-plane. Similarly, at each point, $\boldsymbol{e}_r$ is the image of $\hat{\boldsymbol{e}}_r$ and $\boldsymbol{e}_\theta$ is the image of $\hat{\boldsymbol{e}}_\theta$, with $\boldsymbol{e}_r \cdot \boldsymbol{e}_\theta = 0$ and $\hat{\boldsymbol{e}}_r \cdot \hat{\boldsymbol{e}}_\theta = 0$. This is sketched in Figure 3.2.

Transformation of the Fluid Velocity, $\boldsymbol{u}$.

Consider the fluid velocity in the z-plane and its components with respect to the basis vectors $(\boldsymbol{e}_r, \boldsymbol{e}_\theta)$ and $(\boldsymbol{e}_1, \boldsymbol{e}_2)$. Then

$$\boldsymbol{u} = u_r \boldsymbol{e}_r + u_\theta \boldsymbol{e}_\theta = u_1 \boldsymbol{e}_1 + u_2 \boldsymbol{e}_2 \,. \tag{3.51}$$

The dot product of the first of these equations with $\boldsymbol{e}_r$ and $\boldsymbol{e}_\theta$ in turn gives

$$u_r = \boldsymbol{u} \cdot \boldsymbol{e}_r = \boldsymbol{u} \cdot \frac{1}{l_1} \frac{\partial \boldsymbol{x}}{\partial r} \quad \text{and} \quad u_\theta = \boldsymbol{u} \cdot \boldsymbol{e}_\theta = \boldsymbol{u} \cdot \frac{1}{l_2} \frac{\partial \boldsymbol{x}}{\partial \theta} \,. \tag{3.52}$$

Although we see below that it is not necessary to do so, it is reassuring to express these relations using Cartesian components and basis vectors. To do so, put $\boldsymbol{x} = x_1 \boldsymbol{e}_1 + x_2 \boldsymbol{e}_2$ in the definitions (3.50b) to find that

$$\boldsymbol{e}_r = \frac{1}{l_1} \frac{\partial x_1}{\partial r} \boldsymbol{e}_1 + \frac{1}{l_1} \frac{\partial x_2}{\partial r} \boldsymbol{e}_2 \quad \text{and} \quad \boldsymbol{e}_\theta = \frac{1}{l_2} \frac{\partial x_1}{\partial \theta} \boldsymbol{e}_1 + \frac{1}{l_2} \frac{\partial x_2}{\partial \theta} \boldsymbol{e}_2 \,, \tag{3.53}$$

and use the Cartesian representation in equations (3.51), which gives

$$u_r = \frac{1}{l_1} \left(u_1 \frac{\partial x_1}{\partial r} + u_2 \frac{\partial x_2}{\partial r} \right) \quad \text{and} \quad u_\theta = \frac{1}{l_2} \left(u_1 \frac{\partial x_1}{\partial \theta} + u_2 \frac{\partial x_2}{\partial \theta} \right) . \tag{3.54}$$

To proceed to complex format, introduce the map $z = w(\zeta, t)$ explicitly where $\zeta = re^{i\theta}$, apply the chain rule, and if Cartesian components are used put $z = x_1 + i x_2$, to find that

$$\frac{\partial z}{\partial r} = \frac{\partial z}{\partial \zeta} \frac{\partial \zeta}{\partial r} = \frac{\partial w}{\partial \zeta} e^{i\theta} = \frac{\partial x_1}{\partial r} + i \frac{\partial x_2}{\partial r} \,, \tag{3.55a}$$

$$\frac{\partial z}{\partial \theta} = \frac{\partial z}{\partial \zeta} \frac{\partial \zeta}{\partial \theta} = \frac{\partial w}{\partial \zeta} i\zeta = \frac{\partial x_1}{\partial \theta} + i \frac{\partial x_2}{\partial \theta} \,. \tag{3.55b}$$

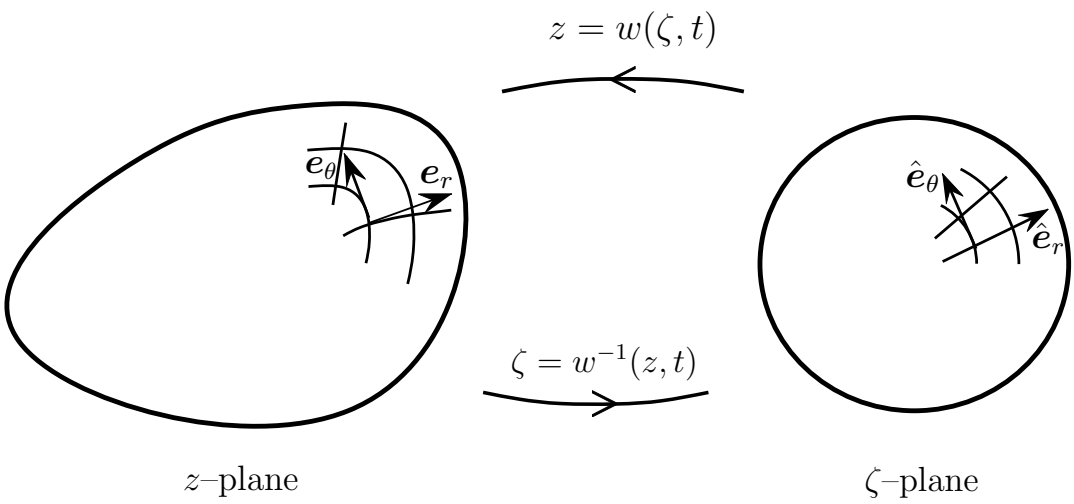

Figure 3.2 The drop interior Ω_1 and interface S in the z-plane are the image under the conformal map $z = w(\zeta, t)$ of the interior of the unit disk $|\zeta| < 1$ and the unit circle $|\zeta| = 1$ in the ζ-plane, with orientation preserved. The polar unit vectors $(\hat{\boldsymbol{e}}_r, \hat{\boldsymbol{e}}_\theta)$ are mapped to orthogonal unit vectors $(\boldsymbol{e}_r, \boldsymbol{e}_\theta)$. At each point ζ the map induces a magnification $|\partial_\zeta w|$ and counterclockwise rotation $\arg(\partial_\zeta w)$.

Use of these relations shows that the orthogonal basis $(\boldsymbol{e}_r, \boldsymbol{e}_\theta)$ of definitions (3.50b) has complex counterpart

$$e_r = \frac{1}{l_1}\frac{\partial z}{\partial r} \text{ with } l_1 = \left|\frac{\partial z}{\partial r}\right| = \left|\frac{\partial w}{\partial \zeta}\right|, \text{ and } e_\theta = \frac{1}{l_2}\frac{\partial z}{\partial \theta} \text{ with } l_2 = \left|\frac{\partial z}{\partial \theta}\right| = \left|\frac{\partial w}{\partial \zeta}\right| r \quad (3.56)$$

since, in the last expression for l_2, $|\zeta| = r$. Also, recall the identity that for vectors $\boldsymbol{a} = a_1\boldsymbol{e}_1 + a_2\boldsymbol{e}_2 \leftrightarrow a = a_1 + ia_2$ and $\boldsymbol{b} = b_1\boldsymbol{e}_1 + b_2\boldsymbol{e}_2 \leftrightarrow b = b_1 + ib_2$,

$$\boldsymbol{a} \cdot \boldsymbol{b} = a_1 b_1 + a_2 b_2 \leftrightarrow Re(a\bar{b}) \quad (3.57)$$

(and $\boldsymbol{b} \times \boldsymbol{a} \leftrightarrow Im(a\bar{b})$).

The velocity components u_r and u_θ can now be written in complex format by using the identity (3.57) with either the vector form (3.52) or the Cartesian component

form (3.54), together with results from relations (3.55) and (3.56), to find

$$u_r = \frac{1}{|\partial_r z|} Re\left(u\,\overline{\partial_r z}\right) = Re\left(u\,e^{-i\,arg(\partial_r z)}\right) = Re\left(u\,e^{-i(\theta+arg(\partial_\zeta w))}\right)\,, \tag{3.58a}$$

$$u_\theta = \frac{1}{|\partial_\theta z|} Re\left(u\,\overline{\partial_\theta z}\right) = Re\left(u\,e^{-i\,arg(\partial_\theta z)}\right) = Re\left(u\,e^{-i(\theta+arg(\partial_\zeta w)+\frac{\pi}{2})}\right)$$

$$= Im\left(u\,e^{-i(\theta+arg(\partial_\zeta w))}\right)\,. \tag{3.58b}$$

Hence,
$$u_r + iu_\theta = u\,e^{-i(\theta+arg(\partial_\zeta w))}\,. \tag{3.59}$$

Transformation of ∇C, $\boldsymbol{u}\cdot\nabla C$, and $\nabla^2 C$.

Since r and θ are orthogonal curvilinear coordinates in the z-plane, the gradient and Laplacian respectively are given in the z-plane by

$$\nabla C = \frac{\boldsymbol{e}_r}{l_1}\frac{\partial C}{\partial r} + \frac{\boldsymbol{e}_\theta}{l_2}\frac{\partial C}{\partial \theta}\,, \quad \text{and} \quad \nabla^2 C = \frac{1}{l_1 l_2}\left(\frac{\partial}{\partial r}\frac{l_2}{l_1}\frac{\partial}{\partial r} + \frac{\partial}{\partial \theta}\frac{l_1}{l_2}\frac{\partial}{\partial \theta}\right) C\,. \tag{3.60}$$

However $\boldsymbol{u} = u_r\boldsymbol{e}_r + u_\theta\boldsymbol{e}_\theta$ and relations (3.56) imply that $l_1 = |\partial_\zeta w|$ and $l_2 = r\,|\partial_\zeta w|$, so that the advection term is

$$\boldsymbol{u}\cdot\nabla C = \frac{1}{|\partial_\zeta w|}\left(u_r\frac{\partial C}{\partial r} + u_\theta\frac{1}{r}\frac{\partial C}{\partial \theta}\right) \tag{3.61}$$

where the transformed velocity components are given by equation (3.58). Similarly,

$$\nabla^2 C = \frac{1}{|\partial_\zeta w|^2}\left(\frac{1}{r}\frac{\partial}{\partial r} r \frac{\partial}{\partial r} + \frac{1}{r^2}\frac{\partial^2}{\partial \theta^2}\right) C\,. \tag{3.62}$$

It turns out that the transformed version of the field equation (3.45) takes a simple form on the unit disk in the ζ-plane, where in terms of polar coordinates $r \in [0,1)$ and $\theta \in [0, 2\pi)$ we have the familiar gradient and Laplacian operators, denoted by

$$\nabla_{(r,\theta)} = \hat{\boldsymbol{e}}_r\frac{\partial}{\partial r} + \hat{\boldsymbol{e}}_\theta\frac{1}{r}\frac{\partial}{\partial \theta}\,, \quad \text{and} \quad \nabla^2_{(r,\theta)} = \frac{1}{r}\frac{\partial}{\partial r} r \frac{\partial}{\partial r} + \frac{1}{r^2}\frac{\partial^2}{\partial \theta^2}\,. \tag{3.63}$$

The velocity $\hat{\boldsymbol{u}}$ defined by

$$\hat{\boldsymbol{u}} = u_r \hat{\boldsymbol{e}}_r + u_\theta \hat{\boldsymbol{e}}_\theta \tag{3.64}$$

is readily identified as the pre-image in the ζ-plane of the fluid velocity $\boldsymbol{u}$ in the z-plane. When equations (3.45) and (3.61) to (3.64) are pieced together the transformed advection-diffusion equation is found to be

$$\frac{\partial C}{\partial t} + \frac{1}{|\partial_\zeta w|}\hat{\boldsymbol{u}} \cdot \nabla_{(r,\theta)} C = \frac{\kappa}{|\partial_\zeta w|^2}\nabla^2_{(r,\theta)} C\,, \quad |\zeta| < 1\,,\ t > 0\,, \tag{3.65}$$

where $\kappa = Pe^{-1}$.

The Boundary Condition.

The conformal map $z = w(\zeta, t)$ is constructed so that the unit circle $|\zeta| = 1$ is mapped to the fluid interface $z \in S$ preserving orientation. The outward unit normal $\hat{\boldsymbol{e}}_r$ and unit tangent $\hat{\boldsymbol{e}}_\theta$ on $|\zeta| = 1$ are therefore mapped to the outward unit normal $\boldsymbol{e}_r$ and unit tangent $\boldsymbol{e}_\theta$ on S. Hence, the normal derivative in the boundary condition (3.67) is given by

$$\left.\frac{\partial C}{\partial n}\right|_S \equiv \boldsymbol{n} \cdot \nabla C|_S = \frac{1}{l_1}\left.\frac{\partial C}{\partial r}\right|_{|\zeta|=1} = \frac{1}{|\partial_\zeta w|}\left.\frac{\partial C}{\partial r}\right|_{|\zeta|=1}\,, \tag{3.66}$$

where l_1 is given at the relations (3.56). The boundary condition on $|\zeta| = 1$ is therefore

$$\frac{J}{|\partial_\zeta w|}\left.\frac{\partial C}{\partial r}\right|_{|\zeta|=1} = -\mathcal{F}(\theta, t) \equiv -Bi\left(K(1-\Gamma)C|_{|\zeta|=1} - \Gamma\right)\,. \tag{3.67}$$

3.7 Time Update of the Interface Position and the Two Coordinate Frames: the Equal Arc Length Frame and the Map Frame

Description of the time update of the interface position and the distribution of computational mesh points on it is included to make the account self-contained. It is similar to that of earlier work [38] and has been modified from [39] mostly to

accommodate changes in notation. The basic construction of the interface position is due to Hou, Lowengrub, and Shelley [16]. The description of the map frame continues the account of Section 3.4 and is specific to this dissertation.

The Interface Position and the Equal Arc Length Frame

The location of the time evolving interface S is determined by the normal component of the fluid velocity on it, per the kinematic boundary condition, which is the second of relations (2.12a). At an arbitrary point z in the interior of either fluid domain Ω_1 or Ω_2 that is away from the interface S, from equation (3.7) or (3.36), the fluid velocity is

$$u(z,t) = u_1 + iu_2 = -i\left(f(z,t) + z\overline{f'(z,t)} + \overline{g(z,t)}\right),$$

from which the definitions (3.8) of the Goursat functions $f(z,t)$ and $g(z,t)$ imply that, away from the interface S,

$$\begin{aligned} u(z,t) = u_1 + iu_2 = &-\frac{1}{2\pi}\int_S \omega(\xi,t)\left(\frac{d\xi}{\xi - z} + \frac{\overline{d\xi}}{\overline{\xi} - \overline{z}}\right) \\ &+ \frac{1}{2\pi}\int_S \overline{\omega(\xi,t)}\, d\left(\frac{\xi - z}{\overline{\xi} - \overline{z}}\right) + (Q + iB)\overline{z} - i\frac{G}{2}z\,. \end{aligned} \tag{3.68}$$

Now let z approach a general point on the interface, which is temporarily denoted by τ, and form either the interior limit as $z \to \tau^-$ from Ω_1 or the exterior limit as $z \to \tau^+$ from Ω_2. It was noted in Sections 3.3 and 3.5 with the details given in Appendix B.2 that the second integral on the right-hand side of equation (3.68) is regular in the limit when $z \in S$ (see equation (B.35)). In the first integral on the right-hand side, the two components of the first integral both generate local, simple pole contributions and Cauchy principal value integrals. However, application of the Plemelj formulae show that for both the interior and exterior limit the pole contributions sum to zero (see equations (B.30a) and (B.30b) for the interior limit and equations (B.30c) and (B.30d) for the exterior limit). The velocity on the interface

is therefore given by

$$u_1 + iu_2|_S = -\frac{1}{2\pi}\!\!\int\!\!\!\!\!\!-_S \omega(\xi,t)\left(\frac{d\xi}{\xi - z} + \frac{d\overline{\xi}}{\overline{\xi} - \overline{z}}\right) + \frac{1}{2\pi}\int_S \overline{\omega(\xi,t)}\, d\left(\frac{\xi - z}{\overline{\xi} - \overline{z}}\right) + (Q + iB)\overline{z} - i\frac{G}{2}z \quad z \in S\,, \tag{3.69}$$

and is automatically continuous across S. Computation of the Cauchy principal value integrals in equation (3.69) follows the same procedure described in Section 3.5 and Appendix B.3.

In terms of its normal and tangential components, u_n and u_s, the fluid velocity on the interface is $\boldsymbol{u} = u_n\boldsymbol{n} + u_s\boldsymbol{s}$, where the complex counterparts of the unit vectors $\boldsymbol{n}$ and $\boldsymbol{s}$ are n and s_T respectively, with $s_T = \partial_s z = in$. It follows that

$$u_n = Re\left\{(u_1 + iu_2)\,|_S\,\overline{n}\right\} \quad \text{and} \quad u_s = Im\left\{(u_1 + iu_2)\,|_S\,\overline{n}\right\} \tag{3.70}$$

on the interface.

The spatial parameterization of the interface S is written in terms of a general real parameter $\alpha \in [0, 2\pi)$ with orientation such that S is traversed counterclockwise as α increases, and a point z on the interface has Cartesian coordinates (x_1, x_2), so that $z = x_1(\alpha, t) + ix_2(\alpha, t)$. In complex form the unit tangent and normal are

$$s_T = \partial_s z = \frac{\partial_\alpha z}{\partial_\alpha s} \equiv e^{i\vartheta}\,, \quad \text{and} \tag{3.71a}$$

$$n = -is_T = -ie^{i\vartheta}\,, \quad \text{where} \quad \partial_\alpha s = |\partial_\alpha z| \tag{3.71b}$$

and ϑ denotes the angle from the positive real axis to the tangent s_T measured conterclockwise positive. In terms of the angles ϕ and ψ that are shown in Figure 3.1 of Section 3.4, $\vartheta = \phi + \psi + \frac{\pi}{2}$. A result that will be needed later follows from differentiating the relation $\partial_\alpha z = \partial_\alpha s\, e^{i\vartheta}$ with respect to time, which implies that

$$\partial^2_{\alpha t} z = \partial^2_{\alpha t} s\, e^{i\vartheta} + \partial_\alpha s\, \partial_t \vartheta\, ie^{i\vartheta}. \tag{3.72}$$

If z is a material point or Lagrangian coordinate on the interface its velocity is equal to the local fluid velocity, so that

$$\partial_t z = u_s e^{i\vartheta} - u_n i e^{i\vartheta} \,. \tag{3.73}$$

However, the shape of the evolving interface is determined by the normal velocity component u_n alone. Although u_s has physical meaning as the tangential component of the fluid velocity, if u_s is replaced by any other smooth periodic function $\varphi(\alpha, t)$ in equation (3.73) then z still lies on the interface but is no longer a material point. The role of $\varphi(\alpha, t)$ is simply to implement a specific choice of $z \in S$ and the interface parameterization via α, without changing the interface shape or evolution.

When u_s is replaced by $\varphi(\alpha, t)$ in equation (3.73), differentiation with respect to α gives a second relation for $\partial^2_{\alpha t} z$,

$$\partial^2_{\alpha t} z = \left(\partial_\alpha \varphi + u_n \partial_\alpha \vartheta\right) e^{i\vartheta} - \left(\partial_\alpha u_n - \varphi\, \partial_\alpha \vartheta\right) i e^{i\vartheta} \,. \tag{3.74}$$

Equating expressions (3.72) and (3.74) for $\partial^2_{\alpha t} z$, we have

$$\partial^2_{\alpha t} s = \partial_\alpha \varphi + u_n \partial_\alpha \vartheta \,, \tag{3.75a}$$

$$\partial_t \vartheta = \frac{1}{\partial_\alpha s} \left(\varphi\, \partial_\alpha \vartheta - \partial_\alpha u_n\right) \,, \tag{3.75b}$$

where S is now described parametrically by arc length $s = s(\alpha, t)$ and tangent angle $\vartheta = \vartheta(\alpha, t)$ instead of $x_1 = x_1(\alpha, t)$ and $x_2 = x_2(\alpha, t)$.

The parameterization used here takes $\alpha \in [0, 2\pi)$ to be a linearly rescaled arc length, so that $\partial_\alpha s$ is constant along the interface, although it varies in time. Hence, $\partial_\alpha s$ is always equal to its mean or average around the interface S, and so too is its time derivative $\partial^2_{\alpha t} s$. Taking the mean of equation (3.75a) around S by integrating with respect to $\alpha \in [0, 2\pi)$ and recalling that $\varphi(\alpha, t)$ is 2π-periodic, we find that

$$\partial^2_{\alpha t} s = \partial_\alpha \varphi + u_n \partial_\alpha \vartheta = \frac{1}{2\pi} \int_0^{2\pi} u_n \partial_{\alpha'} \vartheta \, d\alpha' \,. \tag{3.76}$$

Integration of the second of these equations with respect to α implies that

$$\varphi(\alpha,t) = \frac{\alpha}{2\pi}\int_0^{2\pi} u_n \partial_{\alpha'}\vartheta \, d\alpha' - \int_0^{\alpha} u_n \partial_{\alpha'}\vartheta \, d\alpha' \,, \tag{3.77}$$

where, since it is an arbitrary function of time, $\varphi(\alpha = 0, t)$ has been set to zero. This gives the required tangential velocity $\varphi(\alpha, t)$ of the equal arc length frame.

When (3.77) is substituted into (3.75a) and (3.75b), the system by which the dynamics of the interface is tracked becomes

$$\partial^2_{\alpha t} s = \frac{1}{2\pi}\int_0^{2\pi} u_n \partial_{\alpha'}\vartheta \, d\alpha' \,, \tag{3.78a}$$

$$\partial_t \vartheta = \frac{1}{\partial_\alpha s}\left(\partial_\alpha \vartheta \left\{\frac{\alpha}{2\pi}\int_0^{2\pi} u_n \partial_{\alpha'}\vartheta \, d\alpha' - \int_0^{\alpha} u_n \partial_{\alpha'}\vartheta \, d\alpha'\right\} - \partial_\alpha u_n\right) . \tag{3.78b}$$

At each time step equations (3.78a) and (3.78b) are integrated forward in time for each mesh point $\{\alpha_k\colon 1 \le k \le N\}$, and $(\partial_\alpha s, \vartheta)$ are mapped to the Cartesian coordinates (x_1, x_2) of points on S. The map is given by integration of $\partial_\alpha z = \partial_\alpha s \, e^{i\vartheta}$ with respect to α, which, since $\partial_\alpha s$ is a function of time alone and independent of α, gives

$$x_1(\alpha,t) = x_1(0,t) + \partial_\alpha s(t)\int_0^{\alpha} \cos\left(\vartheta(\alpha',t)\right) \, d\alpha' \tag{3.79a}$$

$$x_2(\alpha,t) = x_2(0,t) + \partial_\alpha s(t)\int_0^{\alpha} \sin\left(\vartheta(\alpha',t)\right) \, d\alpha' \,, \tag{3.79b}$$

where $(x_1(0,t), x_2(0,t))$ is the position of the point $\alpha = 0$ at time t, which is evolved from the kinematic condition and is given by equation (3.73) with the choice that $u_s(0,t) = 0$ for all times $t \ge 0$.

The mesh points of this construction,

$$z_{k,t} = z(\alpha_k, t), \quad \alpha_k = (k-1)h, \ k = 1, 2, \ldots N, \ \text{with } h = 2\pi/N \,, \tag{3.80}$$

were mentioned earlier, at equation (3.22). It is well known that, independent of the specific choice of parameterization of S or definition of $\alpha \in [0, 2\pi)$, since smooth single valued functions defined on S are 2π-periodic in α, their integrals around S can

be evaluated by the trapezoidal rule with spectral accuracy [35]. The specific choice made here, that $\alpha \in [0, 2\pi)$ is a linearly rescaled arc length, with $\partial_\alpha s$ constant along the interface but varying in time, is referred to as the equal arc length frame. This is the coordinate frame used here with trapezoidal rule quadratures for the numerical discretization of the Sherman-Lauricella integral equation and conservation of the surface surfactant phase.

The Map Frame

Recall that M mesh points equally distributed, or equispaced, around the fixed unit circle in the ζ-plane were introduced in Section 3.4 at equation (3.23), namely

$$\zeta_j = e^{i\theta_j}, \quad \text{where } \theta_j = (j-1)\frac{2\pi}{M} \text{ and } j = 1, 2, \ldots M\,. \tag{3.81}$$

This set of points $\{\zeta_j = e^{i\theta_j} : 1 \le j \le M\}$ is referred to as the map frame. Later, in Chapter 4, the term map frame will be generalized to include the points $\{\zeta_{j,l} = r_l e^{i\theta_j} : 1 \le j \le M, 1 \le l \le P\}$ on the disk $0 \le |\zeta| \le 1$, where $\{r_l : 1 \le l \le P\}$ is an ordered set of radial collocation points that is introduced to solve the PDE for the evolution of the bulk surfactant concentration C, but in this section it refers only to the M equispaced points of definition (3.81) on $|\zeta| = 1$.

The image of the map frame is the set of points in the z-plane

$$z_{j,t} = w(\zeta_j = e^{i\theta_j}, t) \;\text{ for } 1 \le j \le M \;\text{ that lie on } S \text{ at time } t\,. \tag{3.82}$$

Examples of the map frame image are shown in Figures 3.3 and 3.4. In both figures, the map frame consists of $M = 1024$ points, of which only 16 equispaced points on the unit disk, i.e., ζ_j with $j = 64m$ and integer $m = 0, 1, \ldots 15$, are shown in panel (a), which is the drop interface at time $t = 0$. The image of these 16 map frame points is shown at the subsequent times $t = 1.0, 2.5$, and 5.0 in both figures for a drop

with viscosity ratio $\lambda = 5$, but for a pure strain with $Q = 0.8$ (and $B = G = 0$) in Figure 3.3, and for a simple shear with $G = 2B = 1$ (and $Q = 0$) in Figure 3.4.

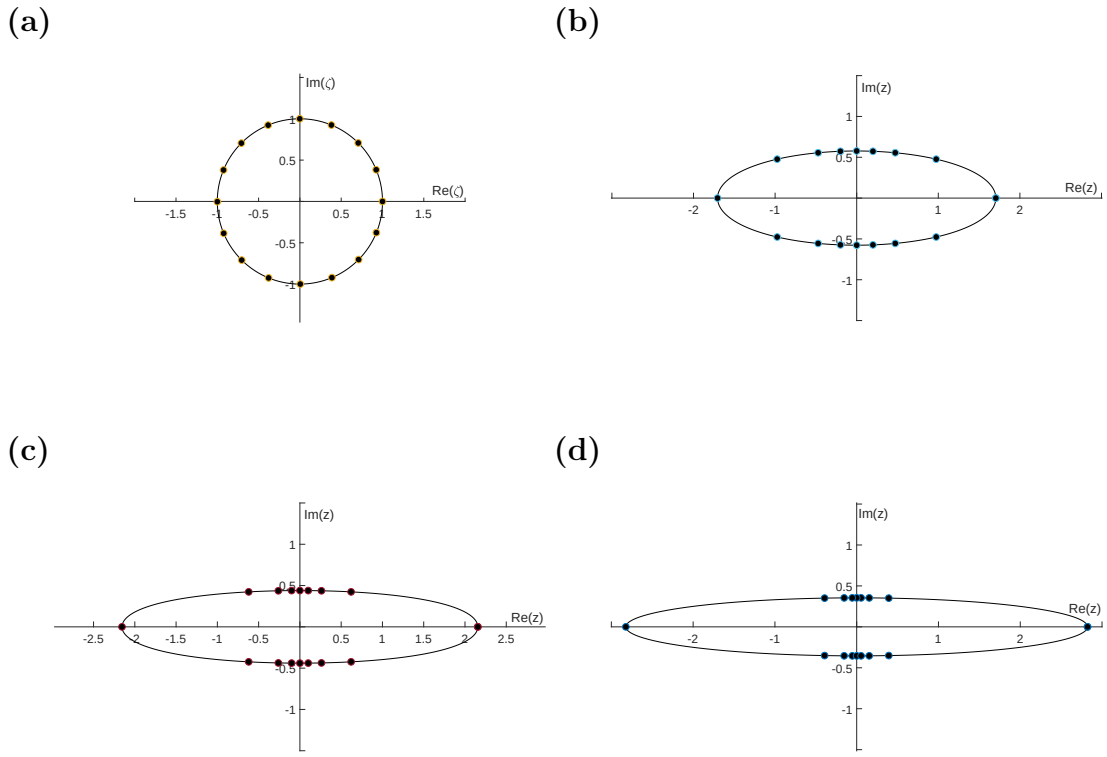

Figure 3.3 A viscous drop with $\lambda = 5$ is stretched in a pure strain with capillary number $Q = 0.8$ ($B = G = 0$). The image under the conformal map $z = w(\zeta, t)$ of equispaced points $\zeta_j = e^{i\theta_j}$ on the unit circle is shown, with $j = 64m$ and integer m, $0 \le m \le 15$, at the sequence of times: (a) t=0, (b) t=1.0, (c) t=2.5, (d) t=5.0. The interface S is the image of the unit circle. As time increases the image points $z_j = w(\zeta_j, t)$ of the map frame crowd to regions of low curvature on S.

In the computational runs for both figures the drop interface is completely surfactant-free, and for the simple shear data of Figure 3.4 the map frame points in the ζ-plane have all been rotated by an angle $\alpha(t)$ (i.e., $\zeta_j = e^{i\theta_j} \mapsto \zeta_j e^{i\alpha(t)} = e^{i(\theta_j + \alpha(t))}$) which is such that the point originally at $\zeta = 1$ at time $t = 0$ stays at the drop pole or 'nose' in the first quadrant of the z-plane for all time.

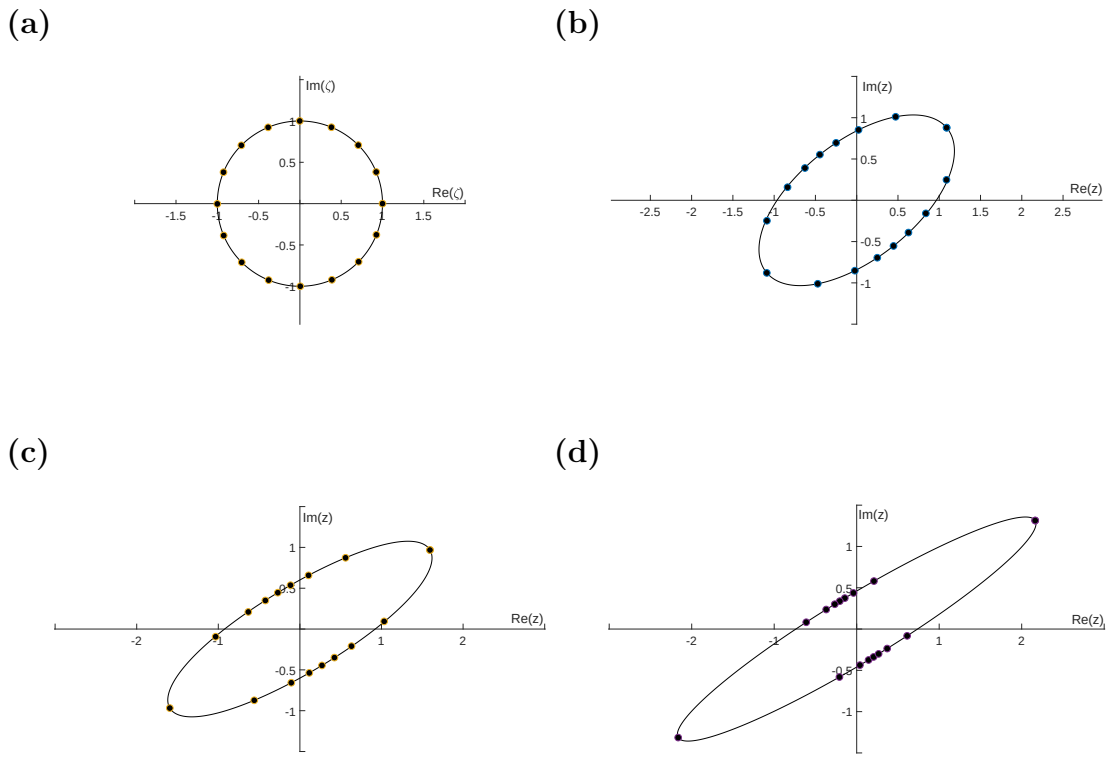

Figure 3.4 Similar to Figure 3.3 but for an imposed simple shear flow. A viscous drop with $\lambda = 5$ is stretched in a simple shear with $G = 2B = 1$ ($Q = 0$). The image under the conformal map $z = w(\zeta, t)$ of equispaced points $\zeta_j = e^{i(\theta_j + \alpha(t))}$ on the unit circle is shown, with $j = 64m$ and integer m, $0 \leq m \leq 15$, at the sequence of times: (a) t=0, (b) t=1.0, (c) t=2.5, (d) t=5.0. The angle $\alpha(t)$ is such that the image of the point at $\zeta = 1$ when $t = 0$ is at the drop pole for all $t \geq 0$. As time increases the image points $z_j = w(\zeta_j, t)$ of the map frame crowd to regions of low curvature on S.

The figures show the phenomenon of "crowding" of the image points in the z-plane, by which image points in the low curvature middle section of the interface S move closer together and conversely the image points near the high curvature poles become more sparse as time increases and the drop becomes more extended or deformed. This is a well known feature of conformal maps between Jordan curves and the unit disk, and the literature on numerical conformal mapping contains a number of estimates and bounds on crowding that are reviewed in [9], in which crowding is described as a form of ill-conditioning. While Figures 3.3 and 3.4 show crowding for

a subset of only 16 of the total 1024 points of the map frame, crowding still limits the resolution at which data can be displayed near the drop poles, even with the full set of map frame points.

To solve the problem at hand, the fluid velocity $\boldsymbol{u}$ and bulk surfactant concentration C need to be found throughout the drop interior Ω_1. Although the solution for $\boldsymbol{u}$ and C is constructed in the ζ-plane, using the map frame, the data is to be displayed in the z-plane. To facilitate this, at each time step, once the current equal arc length frame $\{z_{k,t} = z(\alpha_k, t)\colon 1 \le k \le N\}$ of definition (3.80) and the current conformal map $w(\zeta, t)$ have been found, the inverse map is used to find the pre-image of the equal arc length frame in the ζ-plane. The pre-image $\zeta_{k,t}$ of each equal arc length mesh point $z_{k,t}$ is given by solving

$$W(z, \zeta, t) \equiv z - w(\zeta, t) = 0 \tag{3.83}$$

by Newton-Raphson iteration. The iterates are given by

$$\zeta_{k,n+1} = \zeta_{k,n} + \frac{z_{k,t} - w(\zeta_{k,n}, t)}{\partial_\zeta w(\zeta_{k,n}, t)} \quad n = 0, 1, \dots , \tag{3.84}$$

where the initial estimate $\zeta_{k,0}$ is the converged value at the previous time step, and the map is known in terms of its Taylor series of equation (3.29), namely

$$w(\zeta, t) = \sum_{j=0}^{\infty} c_j(t)\zeta^j \, . \tag{3.85}$$

Here, since the inverse map is from points $z_{k,t}$ on the interface S, their pre-image $\zeta_{k,t}$ lies on the unit circle $|\zeta| = 1$ and can be written as $\zeta_{k,t} = e^{i\theta_{k,t}}$, but the scheme of equations (3.83) to (3.85) can be used to find the pre-image for any point z in the interior Ω_1 if required.

The pre-image of the equal arc length frame is shown in two examples. In the first example, Figure 3.5 shows data for the same pure strain as in Figure 3.3 (i.e., $Q = 0.8$, with $B = G = 0$). Now the equal arc length frame consists of $N = 1024$

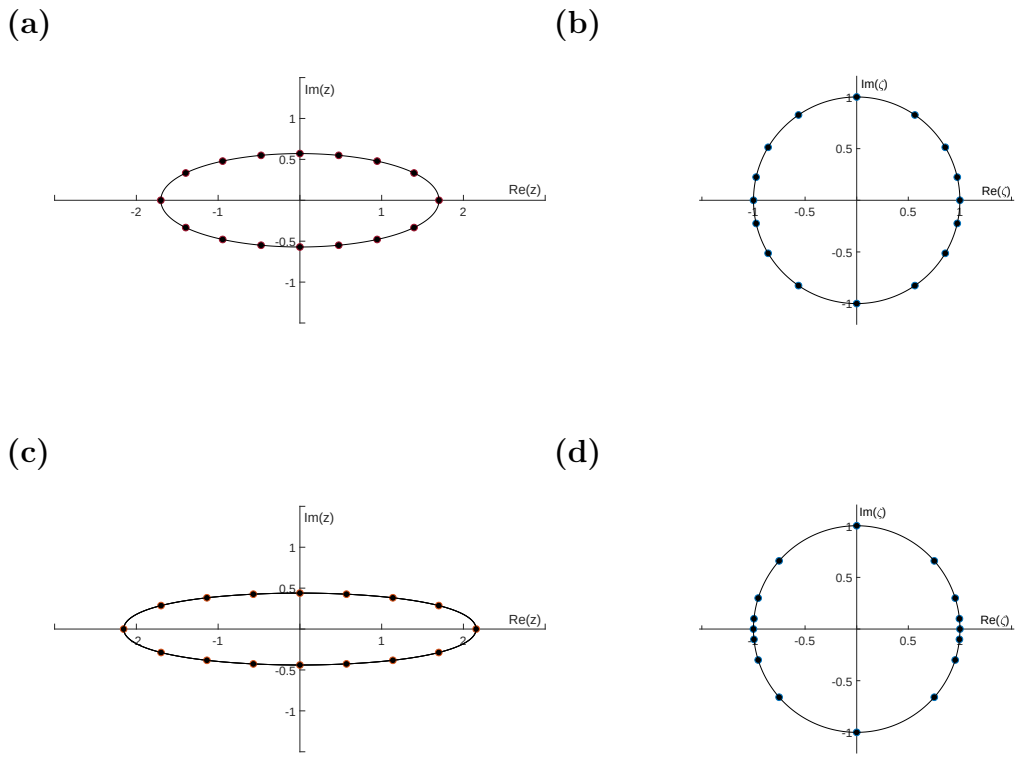

Figure 3.5 Similar to Figure 3.3 but showing the pre-image in the ζ-plane of equispaced points in the equal arc length frame. The viscosity ratio $\lambda = 5$ with strain $Q = 0.8$ ($B = G = 0$). A subset of 16 equispaced markers $z_{k,t}$ on the drop interface in the z-plane is shown with $k = 64n$ for integer n, $0 \leq n \leq 15$. (a) Interface and markers at time $t = 1.0$ with pre-image (b). (c) Interface and the same markers in the z-plane at time $t = 2.5$ with pre-image (d) in the ζ-plane. The inverse map $\zeta = w^{-1}(z, t)$ shows the crowding phenomenon in its converse form.

points $z_{k,t}$, of which only 16 equispaced points are shown with $k = 64n$ and integer $n = 0, 1, \ldots 15$. Panel (a) shows the interface S and 16 equispaced markers at time $t = 1.0$ with their pre-image shown in panel (b), while panel (c) shows S with the same 16 equispaced markers at time $t = 2.5$ with their pre-image in panel (d). These two times and drop profiles are the same as in Figure 3.3, panels (b) and (c). The crowding phenomenon still necessarily applies, only now in its converse form - the pre-image of markers $z_{k,t}$ from regions of high curvature on S become crowded together on the

unit circle while the pre-image from regions of low curvature are sparse, with the redistribution becoming only more noticeable as time increases.

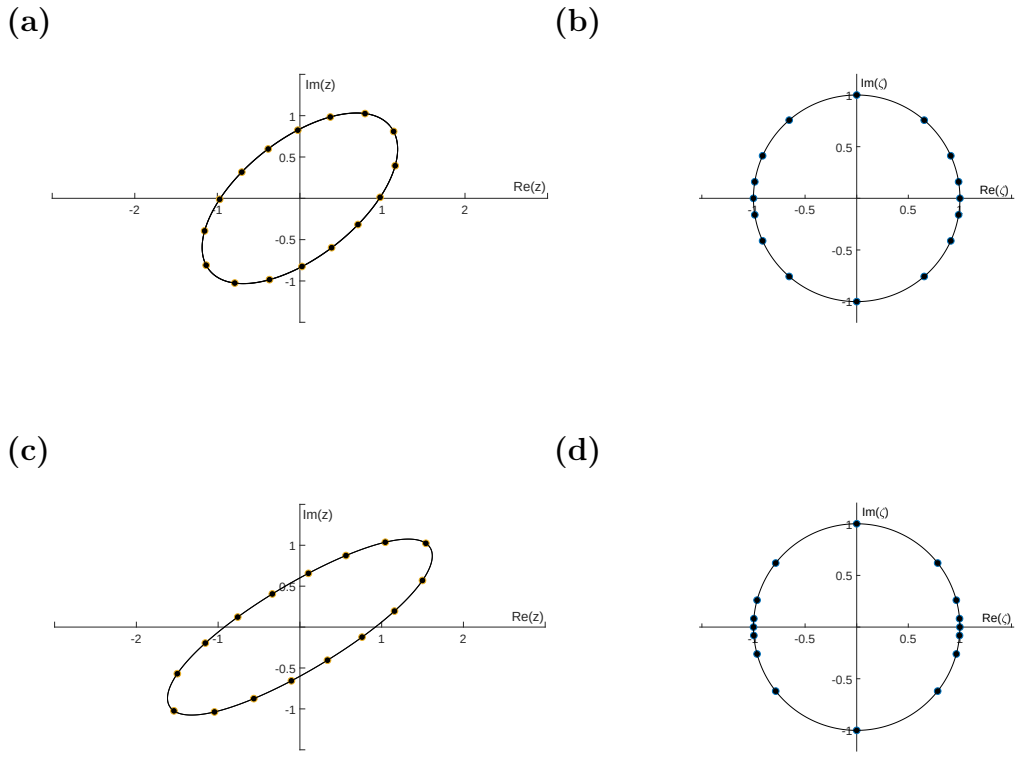

Figure 3.6 Similar to Figure 3.4 but showing the pre-image in the ζ-plane of 16 (out of a total 1024) equispaced markers $z_{k,t}$ in the equal arc length frame. The viscosity ratio $\lambda = 5$ with $G = 2B = 1$ ($Q = 0$). (a) Interface and markers $z_{k,t}$ shown at time $t = 1.0$ with their pre-image shown in (b). (c) Interface and markers $z_{k,t}$ shown at time $t = 2.5$ with their pre-image shown in (d). The redistribution of marker points under the inverse map follows the pattern observed for a strain in Figure 3.5.

Data for the second example is shown in Figure 3.6 for the simple shear of Figure 3.4 (i.e., $G = 2B = 1$, $Q = 0$). The same subset of 16 equispaced points from the total $N = 1024$ interface markers $z_{k,t}$ of the equal arc length frame are shown, with $k = 64n$ and integer $n = 0, 1, \ldots 15$. Panel (a) shows the 16 equispaced interface markers at time $t = 1.0$ with their pre-image shown in panel (b), while panels (c) and (d) show the interface markers and their pre-image (respectively) at the later time of

$t = 2.5$. The redistribution of points follows the same qualitative pattern that was observed in the previous examples. That is, the pre-image of markers $z_{k,t}$ from regions of high curvature on S are crowded together on the unit circle while the pre-image from regions of low curvature are more sparse, and the redistribution becomes more prominent with increasing time. The two times ($t = 1.0$ and 2.5) and drop profiles are the same as in Figure 3.4, panels (b) and (c) .

CHAPTER 4

THE HYBRID METHOD, THE TRADITIONAL METHOD, AND THE NUMERICAL SOLUTION PROCEDURE

4.1 Overview

The hybrid and traditional methods share the same underlying Stokes flow solver and method of solution for conservation of the adsorbed surfactant concentration Γ on the interface S. They differ in the method of solution for conservation of dissolved or bulk surfactant on the drop interior Ω_1.

4.2 Summary of the Initial Boundary Value Problems for the Hybrid and Traditional Methods and Their Numerical Implementation

The Stokes Flow Solver.

The main component of the Stokes flow solver is the Sherman-Lauricella integral equation of Section 3.3, equation (3.10), which is

$$\omega(z,t) - \frac{\beta}{2\pi i}\int_S \omega(\xi,t)\, d\ln\frac{\xi - z}{\overline{\xi} - \overline{z}} - \frac{\beta}{2\pi i}\int_S \overline{\omega(\xi,t)}\, d\frac{\xi - z}{\overline{\xi} - \overline{z}} - \beta(B - iQ)\overline{z} - 2\beta H(t) = -\frac{\gamma}{2}\sigma(\Gamma)\frac{\partial z}{\partial s} \quad \text{for } z \in S\,. \tag{4.1}$$

Here, B and Q are components of the imposed flow matrix (2.20), the parameters $\beta = (1-\lambda)/(1+\lambda)$ and $\gamma = 1/(1+\lambda)$ are known in terms of the viscosity ratio λ, and the function $H(t)$ can be set to zero unless $\lambda = 0$, when the integral equation is rank-deficient and $H(t)$ is given by equation (3.12). The dependent variable $\omega(z,t)$ is a complex density, from which the primitive variables can be found, and the influence of surfactant enters via the surface tension $\sigma(\Gamma)$ alone.

Information contained in continuity of the fluid velocity across S and the stress-balance boundary condition on S has already been used in the Goursat representation

and formulation of the integral equation, and these conditions do not need to be imposed further.

Update of the moving interface is determined by the kinematic condition $\dot{\boldsymbol{x}} = (\boldsymbol{u}\cdot\boldsymbol{n})\boldsymbol{n}$ of equation (2.12a) but its implementation is combined with construction of the equal arc length frame for update of the computational nodes and the parameterization of S. This was introduced in Section 3.7 and is summarized here.

The fluid velocity components on S are given by equation (3.69), namely

$$\begin{aligned} u_1 + iu_2|_S = &- \frac{1}{2\pi}\int_S \omega(\xi,t)\left(\frac{d\xi}{\xi - z} + \frac{d\overline{\xi}}{\overline{\xi} - \overline{z}}\right) \\ &+ \frac{1}{2\pi}\int_S \overline{\omega(\xi,t)}\, d\left(\frac{\xi - z}{\overline{\xi} - \overline{z}}\right) + (Q + iB)\overline{z} - i\frac{G}{2}z \quad z \in S\,, \end{aligned} \tag{4.2}$$

where G is a component of the imposed flow matrix (2.20), from which the normal and tangential components, u_n and u_s, are derived from knowledge of the normal on S via equations (3.70). At each time step, the interface location is given by the computational nodes or mesh points of the equal arc length frame, which is stored in $\{(s_k, \vartheta_k) : 1 \le k \le N\}$. The points s_k are equally spaced in arc length s, measured counterclockwise along S from a well-defined origin on S, and ϑ_k is the value of the angle ϑ there, which is measured from the positive x_1-axis to the tangent vector, see Figure 2.1 (Section 2.1) or Figure B.1 (Appendix B.1).

Since the total arc length of the interface varies in time, both s and ϑ are parameterized by a linearly rescaled arc length α that has fixed domain $[0, 2\pi)$. Hence, $\partial_\alpha s(t)$ is a function of time alone, independent of α, with

$$\alpha = \frac{s}{\partial_\alpha s(t)} \in [0, 2\pi)\,. \tag{4.3}$$

The location of the nodes is updated at each time step from knowledge of the normal fluid velocity u_n on S and the tangential velocity $\varphi(\alpha, t)$ of equation (3.77) that maintains the equispacing of the nodes in s. This leads to equations (3.78) for the evolution of $\partial_\alpha s(t)$ and $\vartheta(\alpha, t)$ at the corresponding equispaced points $\{\alpha_k : 1 \le k \le$

$N\}$ in α. For the representation of physical data, the Cartesian coordinates of the nodes can be found from equations (3.79).

The discretization of the Sherman-Lauricella integral equation (4.1) uses the equal arc length frame based on the equispaced points $\{\alpha_k : 1 \le k \le N\}$ with the trapezoidal rule for the evaluation of integrals. This quadrature method is used for the evaluation of all other integrals of smooth periodic functions around S, and gives spectral accuracy [35].

Conservation of Surfactant on the Interface.

Evolution of the adsorbed surfactant concentration Γ on the interface is governed by equation (2.15), where the dissolved surfactant C is present only in the drop interior, so that

$$\left.\frac{\partial \Gamma}{\partial t}\right|_{\boldsymbol{\xi}} - \left.\frac{\partial \boldsymbol{X}}{\partial t}\right|_{\boldsymbol{\xi}} \cdot \nabla_s \Gamma + \nabla_s \cdot (\Gamma \boldsymbol{u}_s) + \Gamma \kappa u_n = \frac{1}{Pe_s} \nabla_s^2 \Gamma - J\, \boldsymbol{n} \cdot \nabla C|_S\,, \quad \boldsymbol{x} \in S. \tag{4.4}$$

This, like the Stokes flow solver, is solved in the equal arc length frame with the interface parameterized by the scalar $\xi = \alpha \in [0, 2\pi)$. That is, $\boldsymbol{x} = \boldsymbol{X}(\alpha, t)$, so that the velocity $\partial_t \boldsymbol{X}|_\alpha = \varphi(\alpha, t)\boldsymbol{s}$, where $\varphi(\alpha, t)$ is the same tangential velocity of the interface nodes that maintains the equal arc length frame, as just described, and $\boldsymbol{s}$ is the unit tangent vector on the interface (see, e.g., Figure 2.1).

In equation (4.4) the surface gradient operator ∇_s, for example, is given in terms of α by $\nabla_s = \boldsymbol{s}\partial_s = \boldsymbol{s}\partial_\alpha / \partial_\alpha s(t)$. When parametrized by α, the conservation law becomes

$$\left.\frac{\partial \Gamma}{\partial t}\right|_{\alpha} - \varphi(\alpha, t)\frac{\partial_\alpha \Gamma}{\partial_\alpha s} + \frac{\partial_\alpha (\Gamma u_s)}{\partial_\alpha s} + \Gamma \kappa u_n = \frac{1}{Pe_s}\frac{\partial_\alpha^2 \Gamma}{(\partial_\alpha s)^2} - J\, \left.\frac{\partial C}{\partial n}\right|_S \quad \text{on } S\,. \tag{4.5}$$

In the numerical implementation of equation (4.5), $\Gamma(\alpha, t)$ has a Fourier series representation on S and all derivatives with respect to α are computed by FFTs. In the diffusion term the inverse of the surface Péclet number is small and the Laplacian

$\nabla_s^2\Gamma$ is not large, as noted in Appendix A.2, so that diffusion does not introduce stiffness and can be treated explicitly. In fact the diffusion term can be neglected in the simulations. The normal derivative of the bulk surfactant concentration at the interface, $\frac{\partial C}{\partial n}$, is evaluated explicitly using Chebyshev differentiation via FFTs, in the transition layer for the hybrid method, and using the conformal map and ζ-plane for the traditional method. The time step is addressed in Section 4.3

Further details of the numerical discretization and implementation for the Stokes flow solver and evolution of surface surfactant can be found in [38].

4.2.1 Solution for the Bulk Surfactant Concentration via the Traditional Method

In the traditional numerical method, the conservation law (2.16) for evolution of the bulk surfactant concentration C on the drop interior Ω_1 is solved by first transforming it from the physical domain in the z-plane to the fixed unit disk $|\zeta| < 1$ in the ζ-plane via the conformal map $z = w(\zeta, t)$ or its inverse. It is then solved on the unit disk by a Chebyshev spectral method, and the data is mapped back to the z-plane for presentation and interpretation.

The transformed version of equation (2.16) in the ζ-plane was found in Section 3.6 at equation (3.65), namely

$$\frac{\partial C}{\partial t} + \frac{1}{|\partial_\zeta w|}\hat{\boldsymbol{u}} \cdot \nabla_{(r,\theta)} C = \frac{\kappa}{|\partial_\zeta w|^2}\nabla^2_{(r,\theta)} C\,, \quad \text{on } |\zeta| < 1\,,\ t > 0\,, \tag{4.6}$$

where κ is the inverse of the Péclet number Pe. Here, $\nabla_{(r,\theta)}$ and $\nabla^2_{(r,\theta)}$ are the familiar gradient and Laplacian operators in (r, θ) polar coordinates with $\zeta = re^{i\theta}$, and $\partial_\zeta w(\zeta, t)$ is the map derivative on the disk. The velocity field $\hat{\boldsymbol{u}}$ is needed throughout the disk interior whereas the Stokes flow solver is based on a boundary integral method, so that the construction of $\hat{\boldsymbol{u}}$ away from the boundaries in the z and ζ-planes is a necessary but computationally costly component of the problem.

To find $\hat{\boldsymbol{u}}$ the pre-image of the Goursat functions $f(z)$ and the principal part of $g(z)$ are mapped to the unit circle $|\zeta| = 1$ by the construction of Section 3.5, where their Fourier series and coefficients $\{F_k(t)\}$ and $\{G_k(t)\}$ are found by FFT. Once the Fourier coefficients on the circle are known, analytic continuation onto the interior of the disk requires function evaluation alone, and is numerically stable, see equations (3.39) to (3.43). The Cartesian components of the fluid velocity (u_1, u_2) at z are then given by evaluating the right-hand side of equation (3.44) at ζ, where $z = w(\zeta, t)$, from which the polar velocity components (u_r, u_θ) at ζ are found by the construction of Section 3.6 that leads to equation (3.59). This gives the velocity field $\hat{\boldsymbol{u}} =< u_r, u_\theta >$ of equation (3.64). The Goursat functions, map, and velocity component data on the disk are stored in their Fourier coefficients, and all operations of the construction apart from multiplication and division are carried out in Fourier space.

Written in a more explicit form, we now have the advection-diffusion equation for C on the unit disk $r \in [0, 1)$, $\theta \in [0, 2\pi)$,

$$\frac{\partial C}{\partial t} + \frac{1}{|\partial_\zeta w|}\left(u_r \frac{\partial}{\partial r} + u_\theta \frac{1}{r}\frac{\partial}{\partial \theta}\right) C = \frac{1}{Pe\,|\partial_\zeta w|^2}\left(\frac{1}{r}\frac{\partial}{\partial r} r \frac{\partial}{\partial r} + \frac{1}{r^2}\frac{\partial^2}{\partial \theta^2}\right) C\,, \tag{4.7}$$

in which coefficients of the spatial derivatives can be evaluated as functions of space and time. The transformed boundary condition (3.67) on $r = 1$ is

$$\frac{J}{|\partial_\zeta w|}\left.\frac{\partial C}{\partial r}\right|_{r=1} = -Bi\left(K(1-\Gamma)C|_{r=1} - \Gamma\right)\,. \tag{4.8}$$

The Spectral Method.

The solution in space of the initial boundary value problem (4.7) and (4.8) is found by a 2D polar Chebshev spectral method that is described in the book by Trefethen [34], Chapter 11, and uses a treatment of the radial coordinate attributed to Fornberg [12].

The method uses a Chebyshev discretization in r for $r \in [-1, 1]$ with Chebyshev-Lobatto collocation points at

$$r = r_i = \cos\left(\frac{i\pi}{N_r}\right), \text{ for } i = 0, 1, \ldots, N_r - 1 \text{ with } N_r \text{ odd}. \tag{4.9}$$

These are dense near the boundary $r = 1$, where the transition layer is located, which helps to resolve the large normal gradients that are expected there, and are relatively sparse near the drop center $r = 0$, where the solution is smooth. With N_r an odd integer there is no collocation point at $r = 0$, so that a possible coordinate singularity there is avoided. A complex Fourier discretization is used in the periodic θ-direction for $\theta \in [0, 2\pi)$, with uniformly distributed collocation points

$$\theta = \theta_j = (j-1)h \text{ with } h = \frac{2\pi}{N_\theta}, \text{ for } j = 1, 2, \ldots, N_\theta \text{ with } N_\theta \text{ even}. \tag{4.10}$$

Since the solution for C is to be single-valued on the unit disk $(r, \theta) \in [0, 1) \times [0, 2\pi)$ but the computational domain is the rectangle $(r, \theta) \in [-1, 1] \times [0, 2\pi)$ a symmetry condition

$$u(r, \theta) = u(-r, (\theta + \pi) \text{ modulo } 2\pi) \tag{4.11}$$

must be imposed on the numerical solution. This is done by constructing differentiation matrices that have block tensor product or Kronecker product structure. Whereas spatial derivatives on the rectangle would require a full complement of $(N_r - 1)N_\theta$ mesh points, the mesh of the map frame on the interior of the unit disk consists of

$$\frac{N_r - 1}{2} N_\theta \text{ mesh points with } i = 1, \ldots, \frac{N_r - 1}{2} \text{ and } j = 1, 2, \ldots, N_\theta \tag{4.12}$$

in the radial points r_i of definition (4.9) and azimuthal points θ_j of definition (4.10). Notice that the conformal map and map frame as described in Sections 3.4 and 3.7 is

constructed by mapping only the domain boundary points, for which $i = 0$. For the mesh points closest to the origin, $i = \frac{N_r-1}{2}$, and the radius $r = \cos\frac{\pi}{2}(1 - \frac{1}{N_r}) > 0$.

The azimuthal derivatives of the discretization use the Fourier spectral differentiation matrix D_θ, and the radial derivatives are given by matrices of block Kronecker product structure that are derived from the Chebyshev differentiation matrix D_r [34]. The entries of D_r and D_θ are given in Appendix C.1. This leads to the discretization of equation (4.7) given by

$$\begin{aligned}
&\frac{\partial C}{\partial t} + M\left\{U\left(E_1 \otimes \begin{pmatrix} I & 0 \\ 0 & I \end{pmatrix} + E_2 \otimes \begin{pmatrix} 0 & I \\ I & 0 \end{pmatrix}\right) + V(R \otimes D_\theta)\right\} C \\
&= N\left\{(D_1 + RE_1) \otimes \begin{pmatrix} I & 0 \\ 0 & I \end{pmatrix} + (D_2 + RE_2) \otimes \begin{pmatrix} 0 & I \\ I & 0 \end{pmatrix} + R^2 \otimes D_\theta^2\right\} C\,.
\end{aligned} \tag{4.13}$$

Here, all terms have been written out in the same order, reading from left to right, as they appear in equation (4.7) but the r-derivative term of the Laplacian has been expanded. The Kronecker product is denoted by $\otimes$, and I is the $N_\theta/2 \times N_\theta/2$ identity matrix. The other matrices of the discretized equation (4.13) are defined as follows:

(i) From the $(N_r + 1) \times (N_r + 1)$ differentiation matrix D_r, the first and last rows that correspond to end-points of the interval $r \in [-1, 1]$ are deleted to form the $(N_r - 1) \times (N_r - 1)$ matrix $\tilde{D}_r$ for construction of the r-derivatives of the boundary value problem. Then E_1 and E_2 are the top left and right quadrants of $\tilde{D}_r$ and have size $\frac{N_r-1}{2} \times \frac{N_r-1}{2}$. The terms in E_1 and E_2 correspond to the first derivative $\frac{\partial}{\partial r}$.

(ii) Similarly, from the $(N_r + 1) \times (N_r + 1)$ differentiation matrix D_r^2, the first and last rows are deleted to form the $(N_r - 1) \times (N_r - 1)$ matrix $\tilde{D}_r^2$. Then D_1 and D_2 are the top left and right quadrants of $\tilde{D}_r^2$ and have size $\frac{N_r-1}{2} \times \frac{N_r-1}{2}$. The terms in D_1 and D_2 correspond to the second derivative $\frac{\partial^2}{\partial r^2}$.

(iii) The $N_\theta \times N_\theta$ Fourier differentiation matrices D_θ and D_θ^2 correspond to the derivatives $\frac{\partial}{\partial\theta}$ and $\frac{\partial^2}{\partial\theta^2}$ respectively.

(iv) The remaining matrices are all diagonal. First,

$$R = \text{diag}(r_i^{-1}), \quad i = 1, \ldots, \frac{N_r - 1}{2} \tag{4.14}$$

corresponds to the metric factor $\frac{1}{r}$ in the θ-derivatives, and has size $\frac{N_r-1}{2} \times \frac{N_r-1}{2}$. The other diagonal matrices are

$$\begin{aligned} U = \text{diag}(u_{r,i,j})\,, \quad V = \text{diag}(u_{\theta,i,j})\,, \\ M = \text{diag}\left(\frac{1}{|\partial_\zeta w_{i,j}|}\right), \quad N = \text{diag}\left(\frac{1}{Pe|\partial_\zeta w_{i,j}|^2}\right)\,, \end{aligned} \tag{4.15}$$

where, for example

$$\begin{aligned} &U = \text{diag}(u_{r,i,j}) \text{ is such that } u_{r,i,j} = u_r \text{ at } (r_i, \theta_j) \\ &= \begin{pmatrix} u_{r,1,1} & & & & & & \\ & u_{r,1,2} & & 0 & & & \\ & & \ddots & & & & \\ & & & u_{r,1,N_\theta} & & & \\ & 0 & & & u_{r,2,1} & & \\ & & & & & u_{r,2,2} & \\ & & & & & & \ddots \end{pmatrix} \end{aligned} \tag{4.16}$$

and entries down the diagonal are in increasing values of j for $1 \le j \le N_\theta$ before entries in i for $1 \le i \le \frac{N_r-1}{2}$. These matrices have size $\frac{N_r-1}{2}N_\theta \times \frac{N_r-1}{2}N_\theta$.

At this point the matrices M and N in equation (4.13) can be multiplied into or combined with other matrices in the equation and then omitted from the discussion: M is combined with U and V on the left-hand side, and on the right-hand side N is combined with $D_1 + RE_1$, etc.. The spectral matrices for advection terms on the left and diffusion terms on the right-hand side are of size $\frac{N_r-1}{2}N_\theta \times \frac{N_r-1}{2}N_\theta$ and act on

the $\frac{N_r-1}{2}N_\theta \times 1$ vector array for C. The time step discretization is the same for both the traditional and hybrid methods and is described in Section 4.3.

4.2.2 Solution for the Bulk Surfactant Concentration via the Hybrid Method

The hybrid method is based on a leading order matched asymptotic decomposition of the advection-diffusion equation (2.16) in the limit $Pe \to \infty$. It was first introduced in [4] and has appeared in more recent studies that are listed in the References. This section summarizes the asymptotic model of the hybrid method.

First recall the advection diffusion equation (2.16), which is

$$\frac{\partial C}{\partial t} + \boldsymbol{u} \cdot \nabla C = \frac{1}{Pe}\nabla^2 C\,, \quad \boldsymbol{x} \in \Omega_1\,, \tag{4.17}$$

and the bulk-surface surfactant exchange boundary condition (2.17), which is

$$J\,\boldsymbol{n} \cdot \nabla C|_S = -Bi\,(K(1-\Gamma)C|_S - \Gamma)\,, \quad \boldsymbol{x} \in S \tag{4.18}$$

when bulk surfactant is present in the drop interior alone. In the large bulk Péclet number limit, the small expansion parameter ϵ defined by $0 < \epsilon = Pe^{-1/2} \ll 1$ is introduced with a local transition or boundary layer coordinate $N = \mathcal{O}(1)$ defined by $n = \epsilon N$, where n is the outward normal coordinate on the drop interface S.

The domain Ω_1 of equation (4.17) is decomposed into:

An "Outer" Region.

This is the interior of Ω_1 where the effect of diffusion is small, so that at leading order the dynamics is governed by the diffusion-free version of equation (4.17), namely the transport equation

$$(\partial_t + \boldsymbol{u} \cdot \nabla)C = 0\,, \quad \boldsymbol{x} \in \Omega_1\,, \tag{4.19}$$

with remainder of order $\mathcal{O}(\epsilon)$.

An "Inner" Region.

This is the reduced domain $\Omega_{1r} \subset \Omega_1$ of the transition layer, which is a spatially narrow region of width ϵ adjacent to S, where the normal gradient of C is large like $\mathcal{O}(1/\epsilon)$ and advection and diffusion are both of order $\mathcal{O}(1)$ and balance each other. An intrinsic or surface-fitted coordinate system (ξ_1, ξ_2, n) is introduced that is based on S, in which ξ_1 and ξ_2 are distance coordinates on S and $C = C(\xi_1, \xi_2, N, t)$ depends on the stretched normal coordinate $N = n/\epsilon$. At leading order as $\epsilon \to 0$ the dynamics is governed by the transition layer equation

$$(\partial_t + \boldsymbol{v}_s \cdot \nabla_s + \partial_n v_p|_s N \partial_N) C = \partial_N^2 C \,, \quad \text{in } \Omega_{1r} \,, \tag{4.20a}$$

$$\text{where } \ \partial_n v_p|_s = -(\kappa_1 + \kappa_2) u_n - \nabla_s \cdot \boldsymbol{u}_s \,, \tag{4.20b}$$

with remainder of order $\mathcal{O}(\epsilon)$. Some details of the transformation to the intrinsic frame are given in Appendix C.2. In equation (4.20a), $\boldsymbol{v}_s = \boldsymbol{u}_s - \partial_t \boldsymbol{X}|_{\boldsymbol{\xi}}$, where S has equation $\boldsymbol{x} = \boldsymbol{X}(\xi_1, \xi_2, t)$ and $\boldsymbol{u}_s$ is the tangential fluid velocity on the interface, as in equation (4.4), and the time derivative is taken with (ξ_1, ξ_2) fixed. Equivalent ways of writing these terms are given in Appendix C.2, at equations (C.24). The quantity $\partial_n v_p|_s$ is the rate of extension of a fluid line element normal to S, and is written for an incompressible fluid in terms of surface data in equation (4.20b).

In the 2D context, the transition layer equation can be simplified and expressed with the normalized arc length $\alpha \in [0, 2\pi)$ as the distance coordinate on S, using the same notation and results that led to equation (4.5) for conservation of the surface surfactant concentration. This gives

$$\left(\partial_t|_\alpha + (u_s - \varphi(\alpha, t)) \frac{\partial_\alpha}{\partial_\alpha s} + \partial_n v_p|_s N \partial_N \right) C = \partial_N^2 C \,, \tag{4.21a}$$

$$\text{where } \ \partial_n v_p|_s = -\kappa u_n - \frac{\partial_\alpha u_s}{\partial_\alpha s} \,, \tag{4.21b}$$

and the spatial domain is $\alpha \in [0, 2\pi) \times N \in (-\infty, 0)$.

The bulk-surface surfactant exchange boundary condition (4.18) and exchange term in equation (4.5) need the same ϵ-rescaling for the normal derivative, so that the exchange parameter J is redefined with $J = \epsilon J_0$ and $J_0 = \mathcal{O}(1)$. In the hybrid model, these become

$$J_0\, \partial_N C|_{N=0} = -Bi\, (K(1-\Gamma)C|_{N=0} - \Gamma)\,, \quad \text{on } N = 0\,, \tag{4.22}$$

and

$$\left(\partial_t|_\alpha - \varphi(\alpha,t)\frac{\partial_\alpha}{\partial_\alpha s}\right)\Gamma + \frac{\partial_\alpha(\Gamma u_s)}{\partial_\alpha s} + \Gamma\kappa u_n = \frac{1}{Pe_s}\frac{\partial_\alpha^2\Gamma}{(\partial_\alpha s)^2} - J_0\, \partial_N C|_{N=0} \tag{4.23}$$

on the spatial domain $\alpha \in [0, 2\pi)$.

Matching Conditions.

Asymptotic matching between the solution of equation (4.19) as $n \to 0^-$ on the "outer" region and the solution of equation (4.21) as $N \to -\infty$ on the "inner" region is determined by the sign of $\partial_n v_p|_s$. In physical terms, the matching condition depends on the direction of the normal fluid velocity adjacent to the interface, which is inflow when $\partial_n v_p|_s \leq 0$ and outflow when $\partial_n v_p|_s > 0$. This gives the far-field boundary condition for equation (4.21), that

$$\text{as } N \to -\infty \quad \begin{cases} C(\alpha, N, t) \to C(\alpha, n = 0, t) & \text{when } \partial_n v_p|_s \leq 0 \\ \partial_N C(\alpha, N, t) \to 0 & \text{when } \partial_n v_p|_s > 0\,. \end{cases} \tag{4.24}$$

Here, $C(\alpha, n = 0, t)$ is the local solution of the transport equation (4.19), which is considered known over regions of inflow, and when outflow occurs the solution of the transition layer equation with matching condition $\partial_N C \to 0$ gives data for $C(\alpha, n = 0, t)$ as $N \to -\infty$ which is input to the transport equation.

Summary and Numerical Implementation.

With given equilibrium initial data for C at $t = 0$, the initial boundary value problem of the hybrid method is composed of:

(i) The transport equation (4.19) on Ω_1, where the fluid velocity $\boldsymbol{u}$ is known. This is solved on the unit disk in the ζ-plane using the same spectral solution for the traditional method of Section 4.2.1 but with the diffusion term set to zero.

(ii) The transition layer equation (4.21), with boundary condition (4.22) on the drop interface $N = 0$, matching condition (4.24) as $N \to -\infty$, and periodic boundary conditions in α. The solutions for the surface concentration Γ and bulk concentration C are coupled via the boundary condition and surfactant exchange term in equation (4.23).

The numerical implementation on the rectangle $\alpha \in [0, 2\pi) \times N \in (-\infty, 0)$ uses the same Fourier series representation for C with respect to the tangential coordinate α that is used for the conservation law in forms (4.5) and (4.23) for Γ, with tangential derivatives evaluated by FFT. In the normal direction a Chebyshev spectral method is used with Chebyshev differentiation matrices. This is similar to the spectral solution of the traditional method on the disk, and is the same as the numerical implementation used for solution of the transition layer equation in [38], where bulk surfactant is present in the drop exterior alone.

4.3 The Discretization for the Time Step

Time derivatives are present in the update of the free boundary or drop interface S, which is uniquely determined by $\partial_\alpha s(\alpha, t)$ and $\vartheta(\alpha, t)$, they are present in the evolution of the surfactant concentrations, $\Gamma(\alpha, t)$ on the interface and $C(\boldsymbol{x}, t)$ in the bulk, and are implied in the update of the conformal map $z = w(\zeta, t)$. The time

evolution can be written as

$$\partial_t \begin{pmatrix} \partial_\alpha s \\ \vartheta \\ w \\ \Gamma \end{pmatrix} = \boldsymbol{R}\left(\partial_\alpha s, \vartheta, w, \Gamma, \partial_n C|_S\right) , \tag{4.25a}$$

$$\partial_t C = S(\partial_\alpha s, \vartheta, w, C) + F(\partial_\alpha s, \vartheta, w, C) . \tag{4.25b}$$

Here, $\boldsymbol{R}$ is defined by equations (3.78) and by equation (4.5) for the traditional method or by equation (4.23) for the hybrid method. The operator for the evolution of C, which is given by equation (4.13) for the traditional method or by equations (4.19) and (4.20) for the hybrid method is split into two components. Of these, F contains the second derivatives in the coordinates r (traditional method) or N (hybrid method) of the diffusion term, and S contains the advection terms and all other derivatives in the diffusion term (traditional method).

Explicitly, for the traditional method we have

$$\begin{aligned} S = N \Bigg\{ & RE_1 \otimes \begin{pmatrix} I & 0 \\ 0 & I \end{pmatrix} + RE_2 \otimes \begin{pmatrix} 0 & I \\ I & 0 \end{pmatrix} + R^2 \otimes D_\theta^2 \Bigg\} C \\ & - M \left\{ U \left(E_1 \otimes \begin{pmatrix} I & 0 \\ 0 & I \end{pmatrix} + E_2 \otimes \begin{pmatrix} 0 & I \\ I & 0 \end{pmatrix} \right) + V(R \otimes D_\theta) \right\} C , \end{aligned} \tag{4.26a}$$

$$F = N \left\{ D_1 \otimes \begin{pmatrix} I & 0 \\ 0 & I \end{pmatrix} + D_2 \otimes \begin{pmatrix} 0 & I \\ I & 0 \end{pmatrix} \right\} C . \tag{4.26b}$$

For the hybrid method, the operator for the transport equation (4.19) is given by setting the diffusion terms, which are pre-multiplied by the map matrix N, to zero, leaving the advection terms in S only. The operator for the transition layer equation (4.20) is given by setting F to the differentiation matrix for $\partial_N^2 C$ and setting S to the spectral discretization of the advection terms in the Cartesian geometry. Since

the time step is essentially the same for both methods, it will be presented primarily for the traditional method, with modifications that are needed for the hybrid method for the most part understood.

The notation can be eased by introducing the vector

$$\boldsymbol{z} = (\partial_\alpha s, \vartheta, w, \Gamma)^T \tag{4.27}$$

into the evolution of the surface-based quantities in equations (4.25), to give the version

$$\partial_t \boldsymbol{z} = \boldsymbol{R}(\boldsymbol{z}, \partial_n C|_S)\,, \tag{4.28a}$$

$$\partial_t C = S(\boldsymbol{z}, C) + F(\boldsymbol{z}, C)\,. \tag{4.28b}$$

Here, the second equation represents the evolution of C in both the inner and outer regions of the hybrid method.

Now let $\boldsymbol{z}_i^n$ denote the discretization of $\boldsymbol{z}$, with $i = 1, \ldots, N$ indexing the spatial parameter α, and n the value at the n^{th} time step; let C_{ij}^n denote the discretization of C, with $i = 1, \ldots, N$ indexing the coordinate tangential to the interface and $j = 1, \ldots, P$ indexing the normal coordinate, with time step indexed by n. Then for a time step of size Δt the discretization is given by:

(i) A predictor step, from step n to step $n+1$, using a forward Euler scheme

$$\widetilde{\boldsymbol{z}}_i^{n+1} = \boldsymbol{z}_i^n + \Delta t\, \boldsymbol{R}(\boldsymbol{z}_i^n, \partial_n C|_{S,i}^n)\,, \tag{4.29a}$$

$$\widetilde{C}_{ij}^{n+1} = C_{ij}^n + \Delta t\, (S(\boldsymbol{z}_i^n, C_{ij}^n) + F(\boldsymbol{z}_i^n, \widetilde{C}_{ij}^{n+1}))\,, \tag{4.29b}$$

but where the diffusion term $F(\boldsymbol{z}, C)$ to the new time step is treated implicitly.

(ii) Followed by a corrector step, to step $n+1$, given by

$$\boldsymbol{z}_i^{n+1} = \boldsymbol{z}_i^n + \frac{\Delta t}{2}\left(\boldsymbol{R}(\boldsymbol{z}_i^n, \partial_n C|_{S,i}^n) + \boldsymbol{R}(\widetilde{\boldsymbol{z}}_i^{n+1}, \partial_n \widetilde{C}|_{S,i}^{n+1})\right) , \tag{4.30a}$$

$$C_{ij}^{n+1} = C_{ij}^n + \frac{\Delta t}{2}\Big(S(\boldsymbol{z}_i^n, C_{ij}^n) + S(\widetilde{\boldsymbol{z}}_i^{n+1}, \widetilde{C}_{ij}^{n+1}) + F(\boldsymbol{z}_i^n, C_{ij}^n) + F(\widetilde{\boldsymbol{z}}_i^{n+1}, C_{ij}^{n+1})\Big) , \tag{4.30b}$$

where the diffusion term $F(\boldsymbol{z}, C)$ to the new time step is again treated implicitly.

The notation can be eased further by omitting the subscripts i and j for the spatial dependence. This scheme is second order accurate, as is shown in Appendix C.3. With respect to $\boldsymbol{z}$ the scheme is Heun's method, and for C the implicit treatment of the diffusion term $F(\boldsymbol{z}, C)$ is a two-step variation of the Crank-Nicolson scheme. Matrix inversion for the implicit terms is performed by GMRES.

The numerical method that has been described is spectrally accurate in space and second order accurate in time.

4.4 The Two Coordinate Frames and the Presentation of Data

In the traditional method, for example, the normal derivative $\partial_n C|_S$ is computed using the map frame of the ζ-plane unit disk but needs to be found at points on the equal arc length frame in the z-plane for input to $\boldsymbol{R}(\boldsymbol{z}, \partial_n C|_S)$ for the evolution of $\boldsymbol{z}$, or specifically for the evolution of Γ.

To do so, the conformal map $z = w(\zeta, t)$ is inverted using the Newton-Raphson scheme described at equations (3.83) to (3.85) of Section 3.7 to find the pre-image of the equal arc length frame on $|\zeta| = 1$, see for example Figures 3.5 and 3.6. If this set of points is $\zeta = e^{i\theta_i}$ then, since the solution method for C on the disk is spectral, FFTs are used to evaluate $\partial_n C|_S$ there for input to $\boldsymbol{R}(\boldsymbol{z}, \partial_n C|_S)$. Similarly, FFTs are used to evaluate C and other variables such as the fluid velocity $\boldsymbol{u}$ at additional points $\zeta_{ij} = r_j e^{i\theta_i}$ on the interior of the disk for the same θ_i. The data are then mapped back to the z-plane for presentation. Because of the "crowding" of points induced

by the conformal map when the drop interface is highly deformed this gives greatly improved resolution near the high-curvature drop poles and on radii in toward the drop center.

In the hybrid method, since the transition layer equation is solved on the equal arc length frame in the direction tangential to the drop interface, data for $\partial_n C|_S$ can be input directly into $\boldsymbol{R}(\boldsymbol{z}, \partial_n C|_S)$ without the need for interpolation. However, the transport equation is solved on the ζ-plane unit disk, so that the same FFT-based interpolation procedure is used for the presentation of data and to find the data for C needed in the asymptotic matching condition (4.24).

To present data from the hybrid method graphically, the solution of the transport equation (4.19) is mapped to the z-plane in the same way as it is for the traditional method, but with the last few columns of data set to zero to incorporate the solution data from the transition layer equation (4.21). The number of rows that are zeroed corresponds to the asymptotic width of the transition layer in the z-plane, which is set to $\epsilon = Pe^{-1/2}$, and the transition layer data are written into the zeroed columns. The data from the two regions are found to blend well, with little need for the interpolation in the normal direction that is performed by MATLAB.

CHAPTER 5

RESULTS OF THE NUMERICAL SIMULATIONS

5.1 Overview

The results of the numerical simulations are organized as follows. After this overview, results of simulations where the imposed far-field flow is a pure strain are presented in Section 5.2, and results of simulations where the imposed flow is a simple (linear) shear are presented in Section 5.3. For each type of imposed flow, the flow parameters of the matrix in equation (2.20) of Section 2.3 are fixed as follows:

$$\text{Pure strain:} \quad \text{capillary number } Q = 0.8, \ (B = G = 0), \tag{5.1}$$

$$\text{Simple shear:} \quad \text{parameters } G = 2B = 1, \ (Q = 0) \ . \tag{5.2}$$

Other parameters or dimensionless groups that are kept fixed throughout the simulations are the elasticity number E in the surface equation of state (2.13), the surface Péclet number Pe_s of equation (2.14) or (4.5), the parameters J, Bi, and K in the surfactant exchange boundary condition (2.17) or (4.8), and the bulk Péclet number-dependent parameter $J_0 = J/\epsilon$ of equations (4.22) and (4.23) for the hybrid method. The fixed values are:

$$E = 0.25, \ Pe_s = 10^3, \ \text{and } J = K = Bi = 1 \, , \tag{5.3}$$

where the parameters are defined in Table 2.2.

For all simulations the initial surface and bulk surfactant concentrations are in equilibrium, with

$$\Gamma = \frac{3}{8} \ \text{ and } \ C = \frac{3}{5} \, . \tag{5.4}$$

For all computational runs the number of collocation points and the time step for the spectral method on the unit disk in the ζ-plane, as described in Section 4.2.1,

are kept fixed. The number of Chebyshev collocation points on $r \in [-1, 1]$ is $N_r = 65$, so that the number of points on the disk is $\frac{N_r-1}{2} = 32$, and the number of uniformly distributed Fourier collocation points in the θ-direction is $N_\theta = 512$. A time step $\Delta t = 0.005$ is found to keep the method numerically stable out to time $t = 7.5$. The number of collocation points of the equal arc length frame for the Stokes flow solver is set to $N = 128$ at early times, which is doubled when the drop shape becomes too highly deformed, using the same criteria described in [38]. Similarly, the number of Chebyshev collocation points used in the spectral solution of the hybrid method transition layer equation is set to 20, [38].

Within each flow type (strain or shear) the remaining parameters that are varied are the viscosity ratio λ and the bulk Péclet number Pe. Two general features can be expected to occur during the evolution in each simulation as time t increases from the initial spherical equilibrium state at $t = 0$: (i) the drop shape deforms, and (ii) an internal recirculating flow develops. The overall deformation is often quantified by the deformation number

$$D = \frac{L - B}{L + B}\,, \tag{5.5}$$

where L and B are respectively the largest and smallest drop radii. Since λ is the ratio of the internal to external fluid viscosity, and fluid viscosity is a measure of resistance to shear, drops with small $\lambda < 1$ offer little resistance to the shearing motion induced by the imposed flow. Their deformation or change in shape is relatively small and reaches a near steady state fairly quickly, while an internal recirculating flow develops early in the evolution and has relatively large magnitude. Conversely, drops with large $\lambda > 1$ continue to a more highly deformed state with larger values of D and are slow to reach their final steady shape. Interior recirculation begins slowly and is relatively weak, or has small magnitude relative to the far-field flow, even after the drop shape has reached an almost steady state.

The variation of steady deformation number and internal recirculation with change in λ has been noted in many studies that are reviewed in, for example, [31], and the increase of interior recirculation with decrease in λ is a feature of the classical Hadamard-Rybczynski solution for a spherical drop in a uniform stream [13, 29], see also [22].

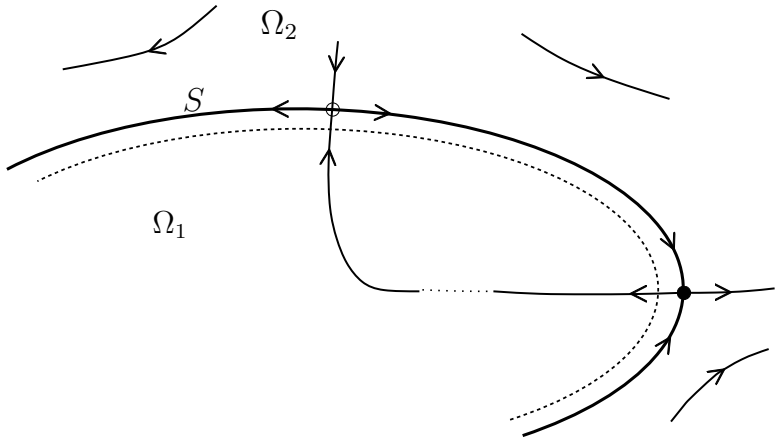

Figure 5.1 Sketch of the flow field in a low viscosity drop at or near steady state in an imposed strain. Part of the drop is shown, which has four-fold symmetry. A recirculating flow is set up with stagnation points on the interface, shown by an open circle at the drop equator and a closed circle at the drop pole. The outer edge of the large Péclet number transition layer is shown dotted. At the outer edge of the transition layer, the flow is incoming near the drop equator and outgoing near the pole.

Based on this reasoning it is anticipated that for a low viscosity drop in an imposed strain with soluble surfactant, the recirculatory flow that begins to develop at early times will continue to redistribute surfactant between the surface and bulk phases via inflow to and outflow from the transition layer long before a spatially uniform surfactant distribution and a true steady state occur. This flow configuration is sketched in Figure 5.1.

At large bulk Péclet number, the hybrid method predicts a drop interior 'core' where the bulk surfactant concentration C satisfies the transport equation $(\partial_t + \boldsymbol{u} \cdot \nabla)C = 0$ with incompressible flow, $\nabla \cdot \boldsymbol{u} = 0$. From Reynolds' transport theorem

this implies that the total amount of bulk surfactant in an arbitrary material or fluid element in the core is conserved. The bulk concentration in the interior core can only change by exchange of fluid elements entering or leaving the transition layer. This is however, a leading order, large Pe model, and at moderate values of Pe bulk surfactant can also enter or leave the core by diffusion.

5.2 Imposed Strain

The imposed strain $\boldsymbol{u} = Q < x_1, -x_2 >$ has no vorticity, but vorticity is generated inside and near the drop by viscous shear stress. The drop shape has four-fold symmetry about the x_1 and x_2-axes and only the part in the first quadrant is shown.

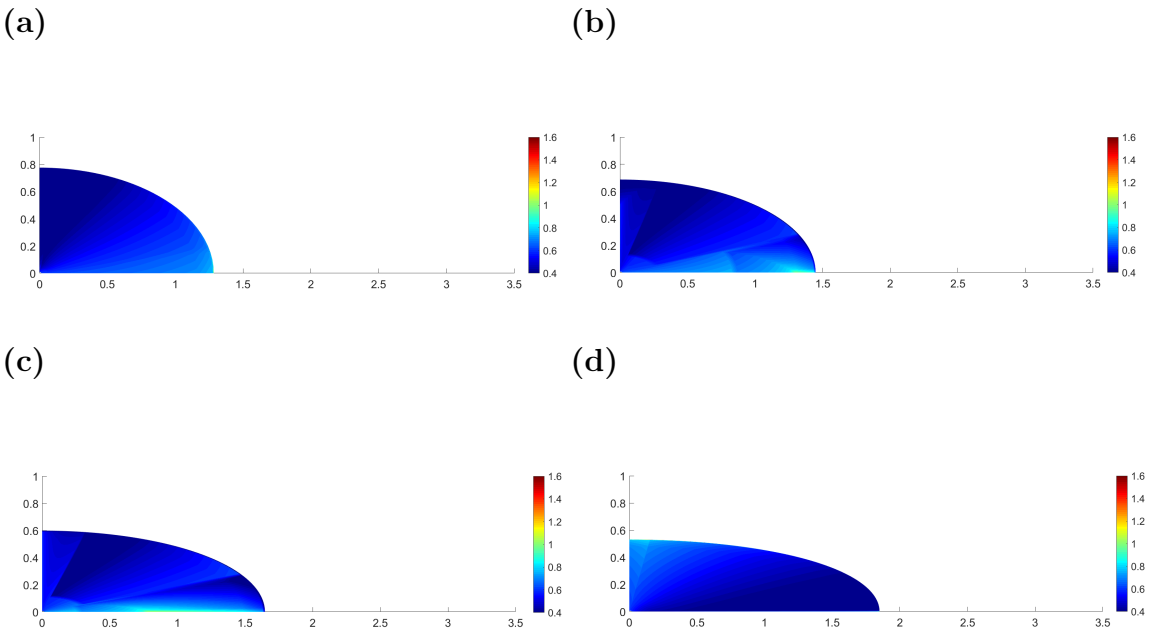

Figure 5.2 A low viscosity drop with $\lambda = 0.2$ is stretched in a pure strain with capillary number $Q = 0.8$ ($B = G = 0$) at Péclet number $Pe = 10^3$. Data for C are shown at a sequence of times: (a) t=1.0, (b) t=2.5, (c) t=5.0, (d) t=7.5. A thin, high surfactant 'plume' emanates from the drop pole in panel (b), then advects into the drop interior along the x_1-axis in panel (c). By the final time of panel (d) it forms a high surfactant region near the drop equator.

Figure 5.2 shows simulation results for a low viscosity drop, with $\lambda = 0.2$, at bulk Péclet number $Pe = 10^3$ at a sequence of times in panels: (a) t=1.0, (b) t=2.5,

(c) t=5.0, and (d) t=7.5. On the drop surface the flow is diverging near the equator (which is on the x_2-axis) and converging near the pole (which is on the x_1-axis) for all times. In panel (a), at $t = 1.0$, the stretching of the interface near the equator causes the surface concentration Γ to decrease, so that bulk surfactant is drawn toward the interface and is depleted from the bulk, which is seen as a nearly triangular sector of low $C \simeq 0.5$ neighboring the x_2-axis. This is complemented near the drop pole, where contraction of the interface causes the surface concentration Γ to increase, so that the local bulk surfactant concentration increases, as seen in a small cap near the pole where $C \simeq 0.8$. At this early time, the interior recirculation near the coordinate axes is about to begin.

By the time of panel (b), $t = 2.5$, interior recirculation has set in and begun to advect a region of $C \simeq 0.6$ from the region near the origin or drop center into a sector neighboring the x_2-axis, while the low $C \simeq 0.5$ sector that it replaces has rotated away from the x_2-axis. Near the drop pole and along the x_1-axis, two regions of high surfactant concentration are seen. One is a broader sector that ends with $C \simeq 0.8$ at $x_1 \simeq 0.8$, while the other is a narrower 'plume' that emanates from the pole to $x_1 \simeq 1.3$ in which $C \simeq 0.9^-$.

The drop deformation continues to increase through the evolution seen in panels (c) and (d) of the figure (i.e., Figure 5.2) but its rate slows. By the time of panel (c), $t = 5.0$, the narrow surfactant plume extends to $x_1 \simeq 0.65$ on the drop interior and is leaving the pole while being stretched and advected toward the origin. A small region of low $C \simeq 0.5$ begins to form near the interface at $x_1 \simeq 1.5$. The sector of high concentration neighboring the x_2-axis strengthens and increases in size, drawing on surfactant that has passed by the drop center. By the time of panel (d), $t = 7.5$, the narrow high concentration plume has also advected into this region. There is now a broad sector of relatively high $C \gtrsim 0.6$ that neighbors the x_2-axis and a sector of nearly the same size that neighbors the x_1-axis where $C \lesssim 0.6$. The position of these

low and high concentration regions has reversed relative to their positions at $t = 1.0$. At $t = 7.5$ the bulk concentration is higher in the region of the equator, and lower in the region of the pole.

Figure 5.3 shows simulation results and data for the bulk concentration C for a high viscosity drop, with $\lambda = 5$, and bulk Péclet number $Pe = 10^3$ at the same sequence of times in panels: (a) t=1.0, (b) t=2.5, (c) t=5.0, and (d) t=7.5. The difference in final deformation and distribution of bulk surfactant compared to the previous data for the low viscosity ($\lambda = 0.2$) drop in the same imposed flow and at the same sequence of times is immediately apparent.

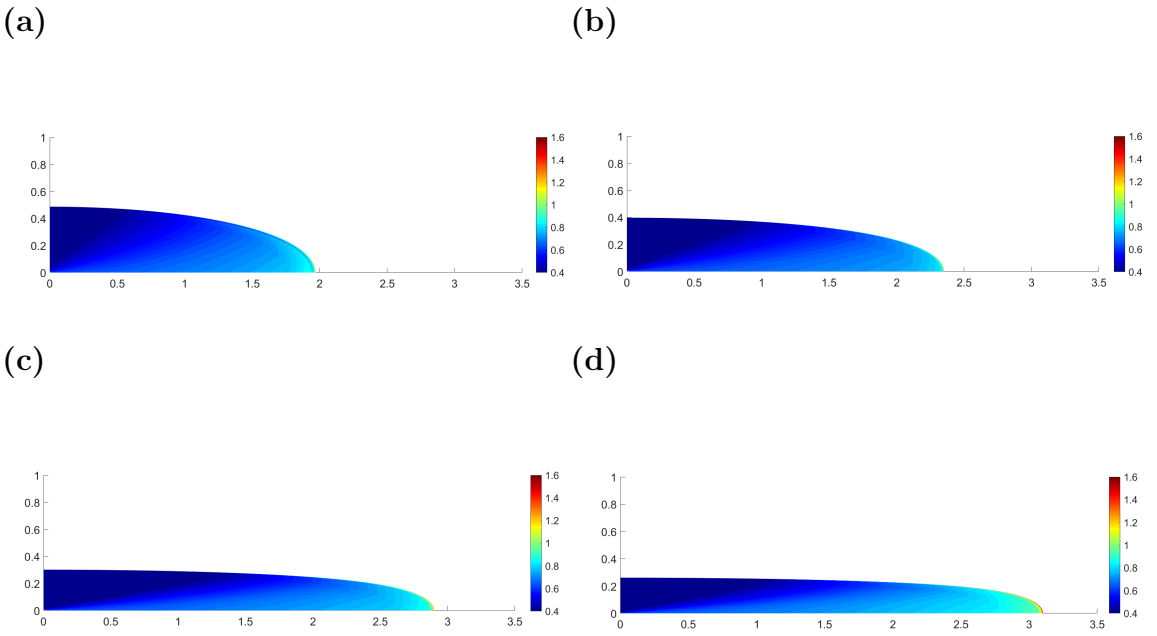

Figure 5.3 A high viscosity drop with $\lambda = 5$ is stretched in a pure strain with capillary number $Q = 0.8$ ($B = G = 0$) at Péclet number $Pe = 10^3$. Data for C are shown at a sequence of times: (a) t=1.0, (b) t=2.5, (c) t=5.0, and (d) t=7.5. The drop becomes highly elongated, with high bulk concentration developing near the drop pole or tip.

When $\lambda = 5$ the drop becomes highly deformed and interior recirculation remains nearly insignificant up to the final time shown. Through the sequence of times of panels (a) to (d) the deformation number continues to increase, and although its rate slows with time, the drop shape at the final time $t = 7.5$ of panel (d) is not

yet close to a steady state. Ultimately, when a steady state is reached, a relatively slow recirculation can be expected to develop in the drop interior but on a greatly elongated domain.

In this simulation the evolution is determined primarily by local expansion and contraction of the interface and how this influences the surface concentration Γ. This mechanism was seen at early times up to $t \lesssim 2.0$ only in the simulation data of Figure 5.2 but holds throughout the duration of this simulation and becomes more clearly defined with time. Near the equator the interface undergoes expansion, leading to a decrease in the surface concentration Γ, away from equilibrium with the local bulk concentration C, so that bulk surfactant is drawn into the interface from the bulk, and the mechanism for this in this simulation appears to be diffusion alone.

Conversely, near the pole the interface contracts, leading to a high local surface concentration, above equilibrium with the bulk concentration, so that surfactant tends to leave the interface and enter the bulk at concentrations that are locally high. Near the drop pole, at the time $t = 5.0$ of panel (c) the bulk concentration immediately next to the interface is $C \simeq 1.4$ over a small cap region and is of the order $C \simeq 0.9$ over a narrow band next to this that extends from $x_1 \simeq 2.75$ to the pole at $x_1 \simeq 2.9$, so that the normal gradient $\partial_n C$ is relatively large. This is where the hybrid method can be expected to resolve the layer structure at large Pe. In this example, it is only in the region around the pole where the gradient $\partial_n C$ is appreciable; elsewhere near the interface the layer structure is not apparent. The layer width, $\epsilon = Pe^{-1/2} \simeq 1/30 \simeq 0.03$..

At the final time $t = 7.5$ of panel (d) the bulk concentration has increased to $C \simeq 1.5$ immediately next to the interface over a larger region at the pole, and the region of high bulk concentration there is larger in size. Surfactant is beginning to be advected away from the pole by a local weak recirculation that has just begun to develop.

The simulation data just reported for Figures 5.2 and 5.3 uses the traditional numerical method, without the large Pe asymptotic reduction of the hybrid method. In the remainder of this section data for ΔC is reported, where

$$\Delta C(\boldsymbol{x}, t) = |C_H(\boldsymbol{x}, t) - C_T(\boldsymbol{x}, t)|\,, \tag{5.6}$$

and $C_H(\boldsymbol{x}, t)$ and $C_T(\boldsymbol{x}, t)$ are the data for the hybrid and traditional methods respectively.

Data for ΔC versus time are shown in Figure 5.4 for simulation data at the same parameter values and sequence of times as in Figure 5.2, i.e., for the low viscosity drop, with $\lambda = 0.2$, and $Pe = 10^3$. The panels show that over almost all of the drop interior: (a) $\Delta C < 0.5{\times}10^{-3}$; (b) $\Delta C < 10^{-3}$; (c) $\Delta C < 0.5{\times}10^{-2}$; and (d) mostly $\Delta C < 10^{-2}$. The difference increases in time, and for example from time $t = 5.0$ (panel (c)) to time $t = 7.5$ (panel (d)) the percentage of the drop area where $\Delta C \gtrsim 0.5 \times 10^{-3}$ increases from approximately 65% to 90%, although $\Delta C < 10^{-4}$ throughout the simulation run near the x_2-axis. The exception to this occurs immediately next to the interface away from the equator, where ΔC approaches 10^{-1}, which is seen as a faint dark line along the interface in panels (b) to (d).

The data for ΔC has a mottled or stippled appearance. When viewed close up, there appears to be a faint band or ribbon near the interface where the pattern of the stippling changes slightly at the drop interior band edge, although ΔC takes the same range of values as the interface is approached across the band. The width of the band is approximately $1/20 = 0.05$ and it marks the region of the transition layer. It contrasts most clearly with the drop interior in panel (a), away from the drop equator. However, note that the stippling of ΔC appears to have no spatial correlation with features noted in the data for C in Figure 5.2, such as the surfactant plume of Figure 5.2 panels (b) and (c), and the spatial distribution of C in Figure 5.2

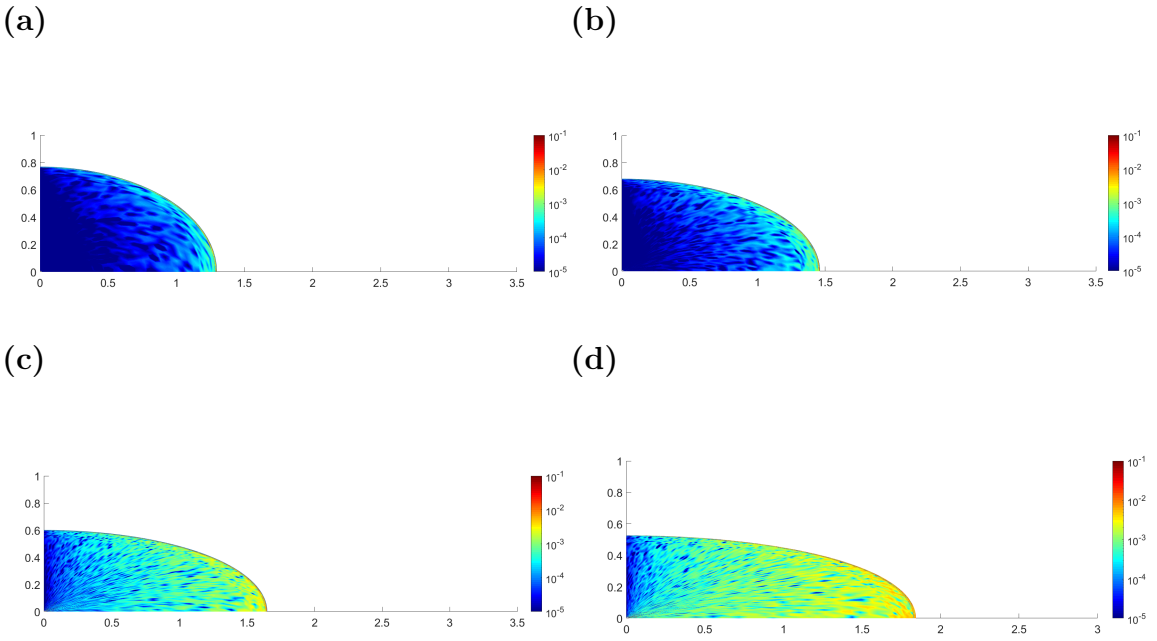

Figure 5.4 Data for the difference ΔC between the hybrid and traditional solution for the bulk surfactant concentration C as it evolves in time. Parameter values and the sequence of times are the same as for the low viscosity ($\lambda = 0.2$) drop simulation of Figure 5.2. The sequence of times shown is: (a) t=1.0, (b) t=2.5, (c) t=5.0, and (d) t=7.5.

panel (d). In other words, these features of the solution for C are resolved equally well by both methods, as separate data for C obtained by the hybrid method shows.

Two examples of how ΔC changes with Pe for a strain flow are shown in Figure 5.5. For the low viscosity ($\lambda = 0.2$) drop, Figure 5.5 panel (b) is the same as Figure 5.4 panel (c), so that $t = 5.0$ and $Pe = 10^3$. This compares with Figure 5.5 panel (a) which shows data at the same time but with the smaller value of $Pe = 10^2$. The comparison between panels (a) and (b) shows that, up to minute details due to the stippling, ΔC has decreased with increase in Pe. This is a positive outcome at this moderately low Pe range - the traditional method has been designed to achieve high accuracy throughout this Péclet number range and can be considered almost exact, whereas the $Pe \to \infty$ hybrid method is becoming more accurate as Pe increases.

A similar trend is shown for the high viscosity ($\lambda = 5$) drop by comparison of Figure 5.5 panels (c) and (d). Panel (d) of this figure shows ΔC data for the

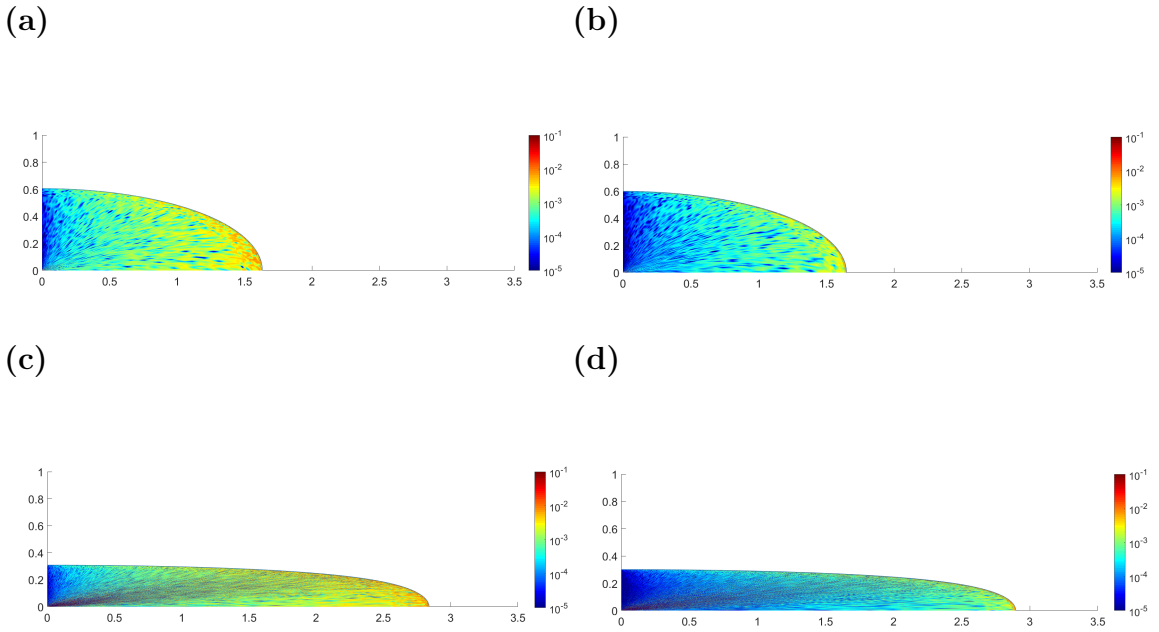

Figure 5.5 Data for ΔC at different values of the bulk Péclet number Pe with all other quantities fixed: Panels (a) and (b), $\lambda = 0.2$ at time $t = 5.0$ with $Pe = 10^2$ in (a) and $Pe = 10^3$ in (b). Panels (c) and (d), $\lambda = 5$ at time $t = 5.0$ with $Pe = 10^2$ in (c) and $Pe = 10^3$ in (d). The drop is stretched in a pure strain with capillary number $Q = 0.8$ ($B = G = 0$).

simulation of Figure 5.3 panel (c), so that $t = 5.0$ and $Pe = 10^3$. This compares with Figure 5.5 panel (a) which shows ΔC at the same time and smaller $Pe = 10^2$. The decrease in ΔC as Pe increases is clearly visible over this Péclet number range at both values of the viscosity ratio.

5.3 Imposed Shear

A major difference between drop deformation when the imposed far-field flow is a pure strain and when it is a simple shear, $\boldsymbol{u} = G < x_2, 0 >$, is caused by the difference in vorticity of the imposed flow. The strain has zero vorticity, whereas the shear has vorticity of magnitude G. Common to both types of imposed flow, the drop shape in an imposed shear has four-fold symmetry.

Figure 5.6 shows simulation results for a low viscosity drop, with $\lambda = 0.2$, at bulk Péclet number $Pe = 10^2$ at the same sequence of times used previously, namely:

(a) t=1.0, (b) t=2.5, (c) t=5.0, and (d) t=7.5. All other parameters are as given at equations (5.1) to (5.4) with the same level of numerical discretization as described there.

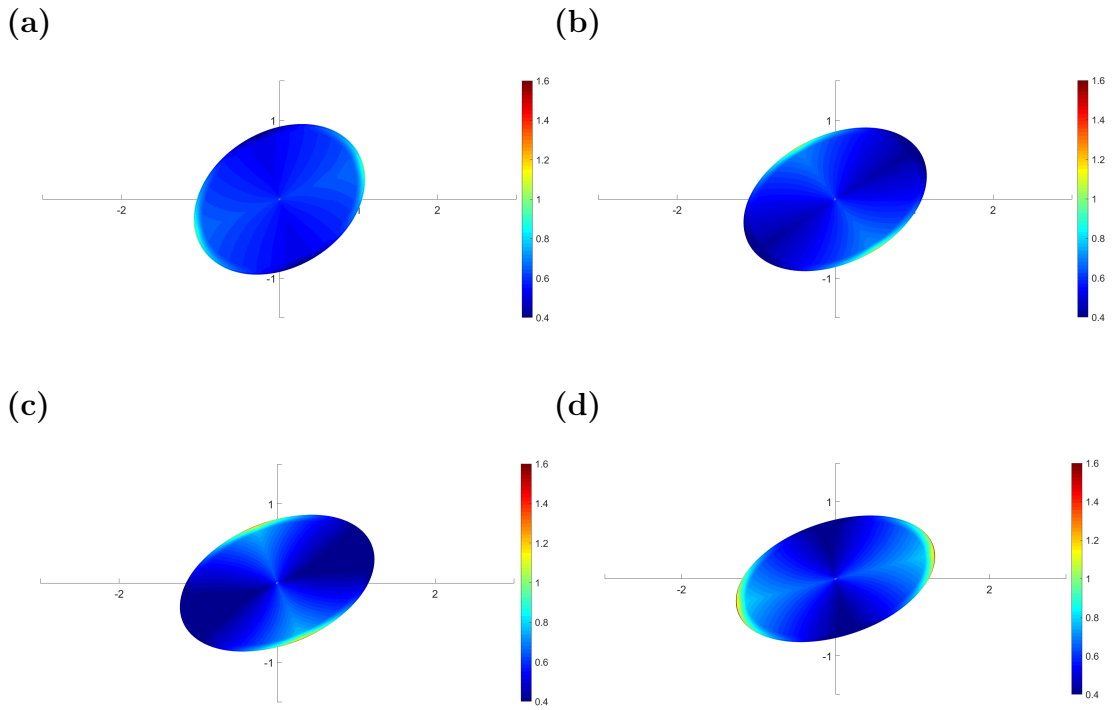

Figure 5.6 A low viscosity drop with $\lambda = 0.2$ is stretched in a simple shear with $G = 2B = 1$ ($Q = 0$) at bulk Péclet number $Pe = 10^2$. The bulk surfactant concentration C is shown at a sequence of times: (a) t=1.0, (b) t=2.5, (c) t=5.0, and (d) t=7.5. After the drop elongates and acquires high surfactant concentration caps along its major axis, as seen in (a), it begins to rotate or tank-tread in the clockwise direction, advecting the caps while continuing to elongate more slowly and align its major axis with the x_1-axis.

In the early stages of the evolution, up to $t \simeq 1.2$ and slightly later than the time of panel (a), the drop begins to elongate and develops a major axis that is aligned with polar angle $\phi \simeq \frac{\pi^-}{4}$. The flow on the interface undergoes contraction near the higher curvature poles, so that the surface concentration Γ is above the bulk equilibrium concentration, and surfactant tends to leave the interface through a developing high concentration transition layer and enters the bulk phase in the drop interior. Near its lower curvature sections, along the minor axis, the flow on the interface expands,

so that the surface surfactant concentration decreases, and surfactant is drawn to the interface from the bulk. Radial sectors of high and low bulk surfactant concentration begin to develop, and are seen in their early stages in panel (a) of Figure 5.6.

At later times, $t \gtrsim 1.2$, the entire drop is set into a circulatory motion that is induced by the vorticity of the imposed flow and viscous stress at the interface. The motion is such that a fluid line element or line of fluid particles that lies along a straight ray emanating from the drop center or origin to the interface remains straight at later times, but rotates in the clockwise direction with angular speed that, because of incompressibility, varies with ϕ, and is relatively slow when the ray points to the elongated high curvature drop poles and fast when it points toward the minor axis low curvature regions. By the time $t = 2.5$ of Figure 5.6 panel (b) the regions of high bulk concentration near the interface have rotated clockwise through an angle $\Delta\phi \simeq \frac{\pi}{2}$ and are aligned with the drop minor axis $\phi \simeq -\frac{\pi}{4}$.

The drop continues to elongate and align its major axis closer to the x_1-axis, but increasingly slowly through the later times of panels (c) and (d). By the final time $t = 7.5$ of Figure 5.6 panel (d), the high surfactant concentration caps have rotated clockwise through an angle $\Delta\phi \simeq \pi$ relative to their initial position and are again aligned with the drop major axis.

The Péclet number for the simulation of Figure 5.6 was chosen to be $Pe = 10^2$ instead of a larger value, such as $Pe = 10^3$, to show the high surfactant concentration transition layer regions more clearly when presenting the data. Figure 5.7 shows the bulk surfactant concentration C for a low viscosity ($\lambda = 0.2$) drop with all parameters and other quantities the same except for the bulk Péclet number, which is 10^2 in panel (a) and 10^3 in panel (b). Panel (a) of this figure is the same as Figure 5.6 panel (d).

The decrease in transition layer thickness $\epsilon = Pe^{-1/2}$ from 0.10 to 0.03 with increase in Pe that is seen in Figure 5.7 and the change in appearance of the bulk surfactant concentration adjacent to the interface is clearly visible near the drop poles.

Other differences such as the drop shape, orientation, and bulk concentration in the drop interior are imperceptible.

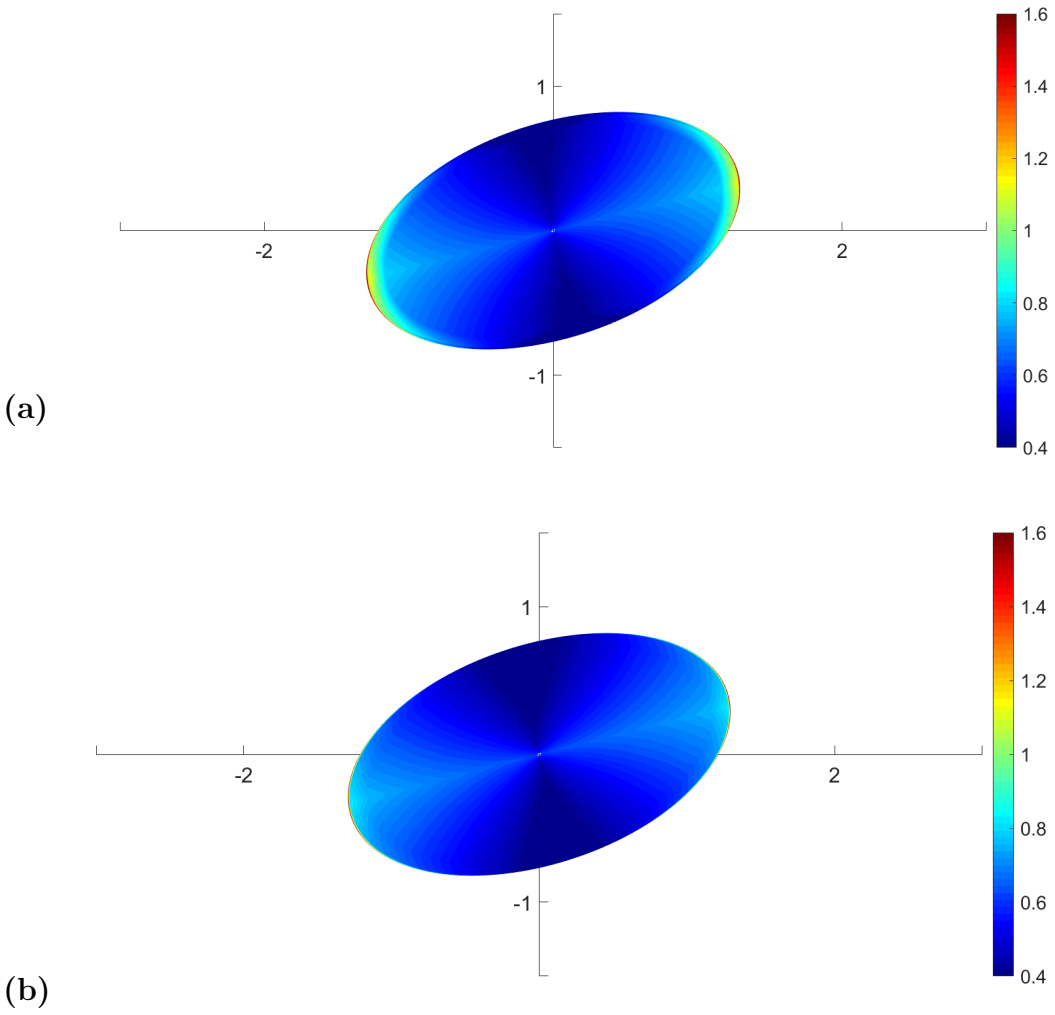

Figure 5.7 Change in bulk surfactant concentration C with increase in Pe for a low viscosity ($\lambda = 0.2$) drop in a shear flow. Panel (a) is a close-up of Figure 5.6(d), while panel (b) shows data for C with all other parameters the same except for increase in bulk Péclet number to $Pe = 10^3$.

Figure 5.8 shows simulation results for a high viscosity drop, with $\lambda = 5$, at bulk Péclet number $Pe = 10^2$, at the same sequence of times chosen throughout this chapter for the presentation of time-dependence: (a) t=1.0, (b) t=2.5, (c) t=5.0, and

(d) t=7.5. All quantities except the drop viscosity are the same as in the low viscosity simulation of Figure 5.6, and the Péclet number is kept at $Pe = 10^2$ to make the data for C near the interface more visible.

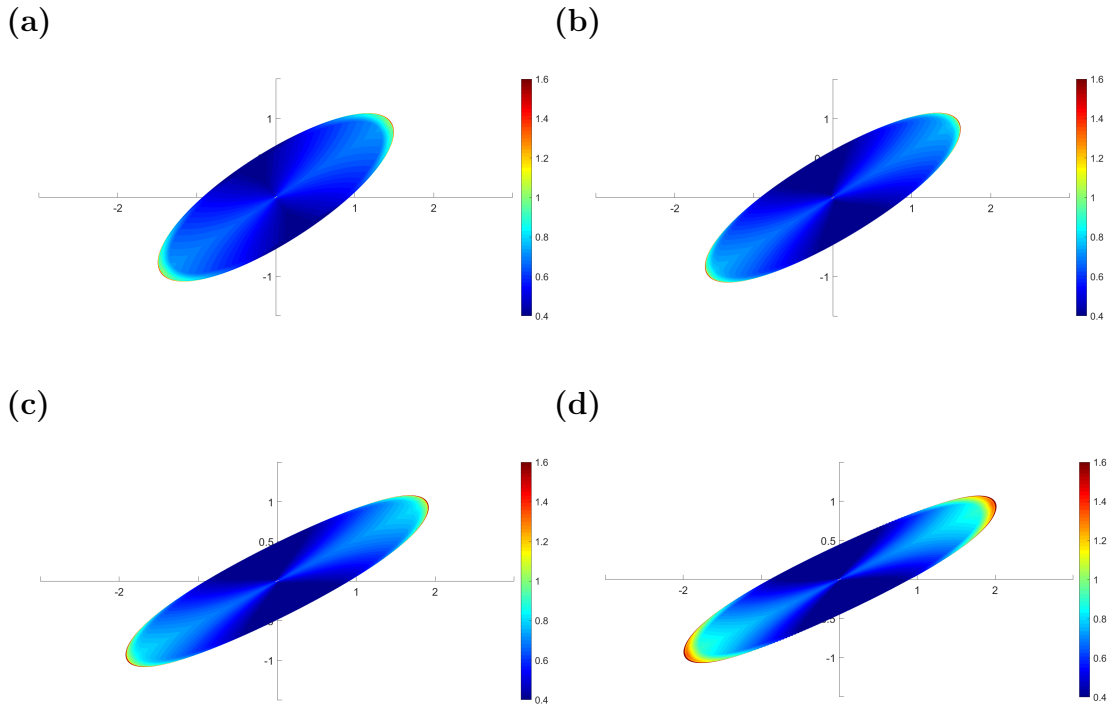

Figure 5.8 A high viscosity drop with $\lambda = 5$ is stretched in a shear with $G = 2B = 1$ ($Q = 0$) at bulk Péclet number $Pe = 10^2$. The drop shape and bulk surfactant concentration C are shown at a sequence of times: (a) t=1.0, (b) t=2.5, (c) t=5.0, and (d) t=7.5. After the drop elongates, the surfactant caps remain at the drop poles throughout the time of the simulation.

In the early stages of the evolution, as seen in panel (a), the drop elongates and acquires high surfactant concentration caps near the drop poles via the same mechanism seen in all examples investigated. Contraction of the interface, that is, convergence of particle paths as they migrate around the drop surface, occurs at the drop poles, inducing a high surface concentration Γ, which then tends to leach into the drop interior across a high bulk surfactant concentration transition layer and enters the drop core by weak diffusion. In contrast, along the low curvature parts of the interface, near the drop minor axis, the surface flow expands, and the reverse surfactant exchange process occurs.

The drop continues to elongate through the later times of panels (b) to (d), while its major axis aligns to a steady inclination closer to the x_1-axis. The drop shape and orientation appear close to a steady state at the times $t = 5.0$ of panel (c) and $t = 7.5$ of panel (d), but there is still a clearly visible increase in surfactant phase exchange occurring near the poles. The high viscosity drop offers more resistance to shear, at its interface and in its interior, so that the tank treading motion of the interface and interior circulation are far weaker than for the previous, low viscosity example of Figure 5.6. The decrease in circulation is sufficiently strong that the high surfactant caps remain at the drop poles throughout the simulation, and are not advected by the vorticity of the imposed flow that was seen previously. At the final time of Figure 5.8 panel (d), the surface and bulk surfactant concentrations are at the highest values encountered throughout this study, with $C \simeq 1.6$ – the pole tips have high curvature and low surface tension.

The simulation results reported above in this section were found using the traditional numerical method, and we now turn to the difference ΔC, defined at equation (5.6), in simulation data for C as found by it and found by the hybrid method.

Figure 5.9 shows simulation results for ΔC for the same conditions as the computational run of Figure 5.6 for a low viscosity drop in a shear except that here the bulk Péclet number is increased to $Pe = 10^3$.

The panels of Figure 5.9 show that, through the sequence of increasing times, over the drop interior: (a) $\Delta C < 0.5 \times 10^{-3}$; (b) $\Delta C < 10^{-3}$; (c) $\Delta C < 0.5 \times 10^{-2}$; and (d) $\Delta C < 0.8 \times 10^{-2}$. These maximum values and their trend are similar to the results seen earlier for a low viscosity drop in an imposed strain flow in Figure 5.4. The difference increases in time, and for example from time $t = 5.0$ (panel (c)) to time $t = 7.5$ (panel (d)) the percentage of the drop area where $\Delta C \gtrsim 0.5 \times 10^{-3}$ increases from approximately 50% to 70%, although $\Delta C < 10^{-4}$ throughout the simulation

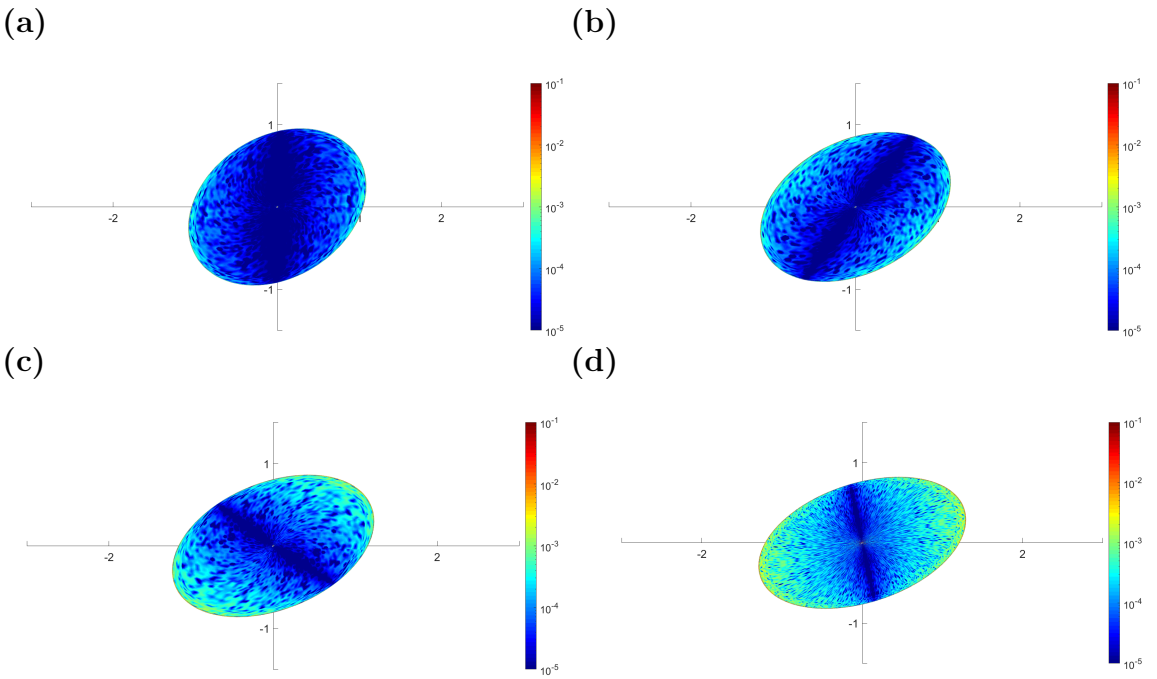

Figure 5.9 The difference ΔC between the hybrid and traditional solution for C evolves over time. Parameter values and the sequence of times are the same as for the low viscosity drop ($\lambda = 0.2$) simulation of Figure 5.6 except that $Pe = 10^3$. The sequence of times is: (a) t=1.0, (b) t=2.5, (c) t=5.0, and (d) t=7.5

along a band that crosses the drop and reorients in time. However, immediately next to the interface away from the equator ΔC approaches 0.5×10^{-1}, which is seen as a faint dark line along the interface in panels (b) to (d). Its width is far less that the transition layer width.

There is a slight change in the stippling of the data for ΔC across the transition layer that is more perceptible when the figure panels are seen in close-up. The layer width, when seen, has width approximately $1/20 = 0.05$. Considering the data for C, there is no discernible change in features such as the position of the high surfactant concentration caps near the interface, that are seen for $Pe = 10^2$ in Figure 5.6 and are advected around the interface for times $t \gtrsim 1.2$, when the Péclet number is increased to 10^3. The lower Pe study is therefore a good point of reference in looking for correlation between ΔC in Figure 5.9 and features of the underlying solution for C.

In this comparison, there appears to be some correlation between the position of larger values of ΔC and the position of the surfactant caps between panels (a) and (d) of Figures 5.9 and 5.6. There is however no such correlation between panels (b) and (c) of the two figures. This suggests that both the hybrid and traditional methods are capable of resolving features of the solution with comparable accuracy.

Figure 5.10 shows two examples of the change in ΔC with increasing Pe for shear flow. Panels (a) and (b) of the figure show ΔC for a low viscosity ($\lambda = 0.2$) drop at time $t = 5.0$ with bulk Péclet number $Pe = 10^2$ in panel (a) and $Pe = 10^3$ in panel (b). Panel (b) of this figure is the same as Figure 5.9 panel (c).

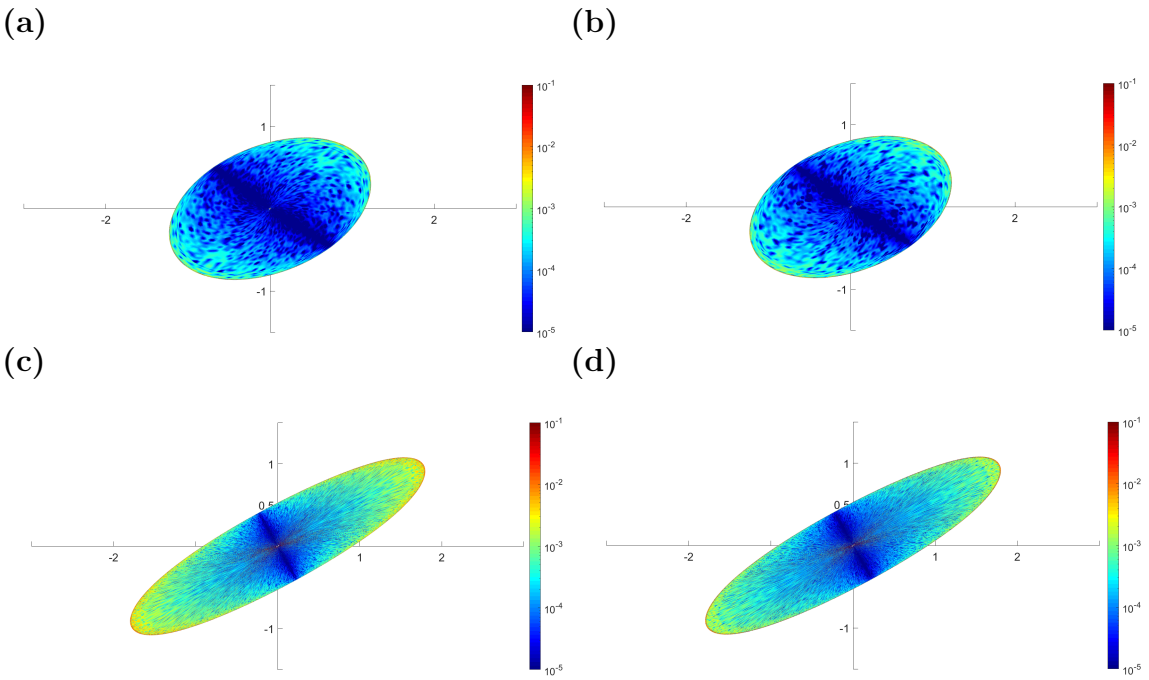

Figure 5.10 Simulation data for ΔC at different values of the bulk Péclet number with all other conditions unchanged. In panels (a) and (b), $\lambda = 0.2$ at time $t = 5.0$ with $Pe = 10^2$ in panel (a) and $Pe = 10^3$ in (b). In panels (c) and (d), $\lambda = 5$ at time $t = 5.0$ with $Pe = 10^2$ in (c) and $Pe = 10^3$ in (d). The drop is stretched in a shear with $G = 2B = 1$ ($Q = 0$).

Over some range of the Péclet number we would expect or hope to see a decrease in ΔC as Pe increases, showing convergence of the two numerical methods, with a possible divergence or failure of the traditional method at very large values of Pe

where the hybrid method is still valid. Over the range shown here, in panels (a) and (b) ΔC remains almost unchanged. Note that, given ΔC is uniformly small at both values of Pe and the error of the leading order $Pe \to \infty$ hybrid method is of order $\mathcal{O}(Pe^{-1/2})$ this is reasonable.

The outcome is more promising in the results for the high viscosity ($\lambda = 5$) drop. Panels (c) and (d) show data at the same time $t = 5.0$, with $Pe = 10^2$ in panel (c) and $Pe = 10^3$ in panel (d). Panel (c) therefore shows data for ΔC that correspond to the data for C of Figure 5.8 panel (c). Larger values of the difference ΔC are found across much of the drop area at this high viscosity setting, with ΔC slightly greater than 10^{-2} near the drop poles when $Pe = 10^2$ in panel (c). However there is a notable decrease in ΔC seen over all regions of the drop area and in particular near the drop poles with increase of Pe to 10^3: compare Figure 5.10 panels (c) and (d).

CHAPTER 6

CONCLUDING REMARKS

The main topic of this dissertation has been the development of numerical methods for investigation of two-phase flow with soluble surfactant in the zero Reynolds number Stokes flow limit that achieve high accuracy at large values of the bulk Péclet number Pe when bulk phase surfactant is present in the drop interior. Two complementary approaches have been developed: one approach uses a traditional numerical method that solves the full set of governing equations using a spectral discretization that is designed to be accurate at values of Pe that are large but finite, and the second approach uses a hybrid method that is derived using techniques of matched asymptotic expansions in the limit $Pe \to \infty$.

To facilitate accuracy of the traditional method the computations have been restricted to two space dimensions (2D), where analytical complex variables methods can be applied. The predictions of the traditional and hybrid methods have been compared for simulations of drop deformation in an imposed flow that is either a pure strain or a simple linear shear, these being the two canonical examples of imposed flow for drop deformation studies.

Two previous studies that use the hybrid approach are [4] and [39]. Of these, the earliest [4] took the drop interior to be inviscid or void and applied both traditional and hybrid solution methods. The second study [39] took the drop interior to be viscous but used the hybrid method alone. In both studies bulk surfactant was present only in the exterior of the drop. The spatial discretization of [4] used finite difference methods, with conformal mapping for its traditional approach. The Stokes flow solver of [39] used a spectral discretization for the Sherman-Lauricella integral equation and a Chebyshev spectral method for spatial discretization of the transition

layer equation in its version of the hybrid method. Both of these spectral methods have been adapted to the present study.

Compared to previous studies that use the hybrid method, the main contribution of this study is its consideration of bulk surfactant on the drop interior. For a single drop in an unbounded surfactant-laden exterior phase, there is an exchange of surfactant between the bulk and surface, with associated changes in surface tension and drop shape, but the exterior phase particle paths pass by the drop and do not encircle it. In the context of the hybrid method, particle paths leaving the transition layer adjacent to the interface carry their bulk concentration away from the drop and do not return. Particle paths entering the transition layer always carry the same uniform ambient bulk concentration into the layer. The interaction between the immediate neighborhood of the drop and the bulk flow is less active than it is when bulk surfactant is present in a continually recirculating interior flow.

In this study a Chebyshev-Fourier spectral discretization has been developed to resolve the evolution of bulk surfactant in the drop interior, which has been described for the traditional method in Section 4.2.1. A diffusion-free version of this has also been used in the hybrid method, which was described in Section 4.2.2. To achieve high accuracy at large Pe in the traditional method, the drop domain in the z-plane was mapped conformally back to the fixed unit disk in the ζ-plane. The map construction via James's method was described in Section 3.4. To find the fluid velocity away from the drop boundary, on the drop interior for evaluation of the bulk surfactant concentration, an analytic continuation method was introduced that enables continuation on the unit disk, where it is fast and numerically stable; this was described in Section 3.5.

The simulation results have been described for both the traditional and hybrid methods, for an imposed pure strain in Section 5.2 and for an imposed simple shear in Section 5.3. In each case results for a low viscosity drop have been compared with

contrasting results for a high viscosity drop. At low drop viscosity the recirculating interior flow is strong, begins early in the deformation process, and advects regions of high and low bulk surfactant concentration at a relatively high rotation rate. At high viscosity the drop can become highly deformed before a weak interior recirculation sets in. At both high and low viscosity, it can be expected that a true steady state is achieved only after multiple interior flow turnover times. How this might scale with material and flow parameters is not yet clear.

Considerations for future study are: (i) an implementation of the map construction that is completely spectral. So far, some steps of the construction are spectral but some polynomial spline interpolation could perhaps be replaced by FFT. (ii) Simulations at increasingly large values of the bulk Péclet number. This would enable a more definitive investigation of the role of the Péclet number in drop deformation as well as comparison of the relative merits of the traditional and hybrid methods. (iii) Comparison of the two numerical methods and validation of the simulation data should be supplemented by presenting systematic convergence studies. (iv) Additional comparison of data found by the traditional and hybrid methods. Differences in the drop shape as found by the two methods was found to be close to round-off error, so it is expected that differences in quantities such as the surface surfactant concentration Γ, for example, will also be small, but a systematic study of this difference and how it varies with change in Péclet number and other parameters has not been included here.

APPENDIX A

DERIVATION OF SOME RESULTS FROM CHAPTER 2

A.1 Derivation of the Capillary Stress and the Marangoni Stress

A derivation of the stress-balance boundary condition (2.3) with spatially varying surface tension can be found in, for example, [22] (pages 200 to 203). The account here includes some technical details that are omitted from [22].

The forces on an arbitrary patch S_c of the interface S are the sum of the forces exerted by the neighboring fluid on the interface, which are expressed in terms of the stress tensor $\boldsymbol{\sigma}$ as S is approached from Ω_1 and from Ω_2 and the outward unit normal $\boldsymbol{n}$, and the surface tension force on the patch S_c due to the rest of the interface $S \setminus S_c$. This acts on the perimeter C of the patch, with force per unit length $\sigma \boldsymbol{t}_s$, where σ is the magnitude of the surface tension and $\boldsymbol{t}_s$ is a unit vector on C that is tangential to S and directed outwards from S_c to $S \setminus S_c$, see Figure A.1. The unit vectors $(\boldsymbol{t}_s, \boldsymbol{t}_c, \boldsymbol{n})$ form a right-handed set at points on C, and $\boldsymbol{t}_c$ is the oriented tangent to C, so that S_c is to its left as C is traversed.

Since the interface has zero mass, the sum of these forces is zero , i.e.,

$$\iint_{S_c} [\boldsymbol{\sigma}]_1^2 \cdot \boldsymbol{n} \, dS + \oint_C \sigma \boldsymbol{t}_s \, ds = 0 \,. \tag{A.1}$$

A generalized form of Stokes' theorem is used to transform the line integral around C to a surface integral over S_c. The approach given here closely follows the generalization of Stokes' theorem of [30] (page 66, theorem 9).

Under sufficient smoothness or regularity conditions, Stokes' theorem transforms the circulation line integral of a vector field $\boldsymbol{v}$ around a closed curve C into a surface

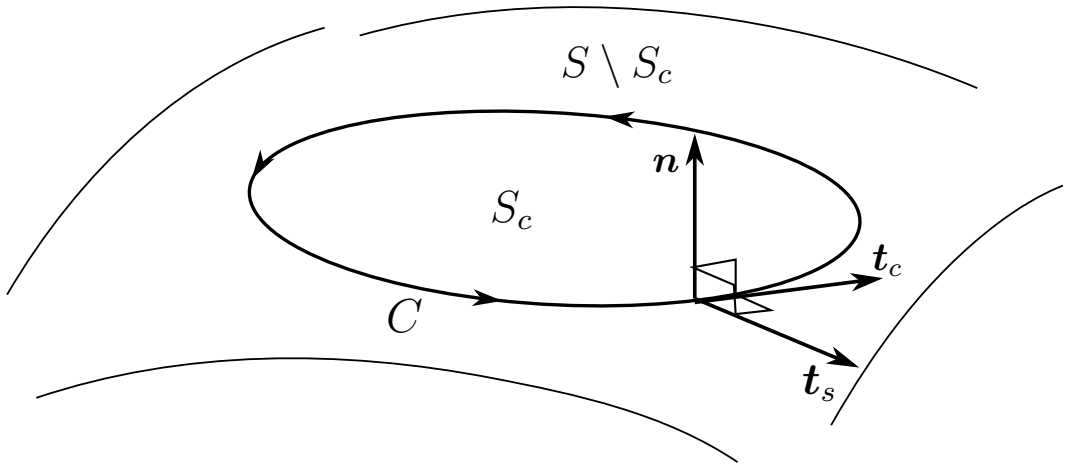

Figure A.1 An arbitrary region or patch S_c of the fluid interface S, with S_c shown simply connected in this illustration, is bounded by a curve C. The curve C has unit tangent vector $\boldsymbol{t}_c$, S has outward unit normal $\boldsymbol{n}$, and the unit vector $\boldsymbol{t}_s$ is in the tangent plane to S such that $(\boldsymbol{t}_s, \boldsymbol{t}_c, \boldsymbol{n})$ form a right-handed set at points on C.

integral over any open surface S that has perimeter C, so that

$$\oint_C \boldsymbol{v} \cdot \boldsymbol{t}\, ds = \iint_S (\nabla \times \boldsymbol{v}) \cdot \boldsymbol{n}\, dS\,, \tag{A.2a}$$

$$\text{or} \quad \oint_C v_i\, t_i\, ds = \iint_S \epsilon_{kli} \frac{\partial v_i}{\partial x_l}\, n_k\, dS \tag{A.2b}$$

in suffix notation. Here $\boldsymbol{t}$ denotes the oriented tangent vector on C and s denotes arc length. If $\boldsymbol{v}$ has only one non-zero component ϕ, let $v_i = \phi\, \delta_{ij}$ where δ_{ij} is the Kronecker delta and j is any one fixed integer $j = 1, 2, 3$. Substitution in (A.2b) gives

$$\oint_C \phi\, t_j\, ds = \iint_S \epsilon_{klj} \frac{\partial \phi}{\partial x_l}\, n_k\, dS = -\iint_S \epsilon_{jlk} \frac{\partial \phi}{\partial x_l}\, n_k\, dS \tag{A.3}$$

or, in vector notation,

$$\oint_C \phi\, \boldsymbol{t}\, ds = -\iint_S \nabla\phi \times \boldsymbol{n}\, dS\,. \tag{A.4}$$

An analogous expression holds when ϕ is replaced by a tensor $\boldsymbol{T}$ of any rank, since each Cartesian component of the tensor is a scalar, for which (A.4) holds. So

$$\oint_C \boldsymbol{T} \otimes \boldsymbol{t}\, ds = -\iint_S (\nabla \otimes \boldsymbol{T}) \times \boldsymbol{n}\, dS\,, \tag{A.5}$$

where $\otimes$ denotes the tensor product, and if $\boldsymbol{T}$ has rank n the integrands of both sides have rank $n+1$.

If $\boldsymbol{T}$ has rank 2, in suffix notation (A.5) is

$$\oint_C T_{ij}\, t_k\, ds = -\iint_S \epsilon_{klm} \frac{\partial T_{ij}}{\partial x_l}\, n_m\, dS\,, \tag{A.6}$$

compare (A.3). To form the contraction of $\boldsymbol{T}$ with $\boldsymbol{t}$, set $k = j$ and let j be the repeated suffix in (A.6), to find

$$\oint_C T_{ij}\, t_j\, ds = -\iint_S \epsilon_{jlm} \frac{\partial T_{ij}}{\partial x_l}\, n_m\, dS\,. \tag{A.7}$$

To write this last, general result in the vector notation of [30], note that $\epsilon_{jlm} = -\epsilon_{mlj}$ in the right-hand side, to find

$$\oint_C \boldsymbol{T} \cdot \boldsymbol{t}\, ds = \iint_S (\nabla \times \boldsymbol{T}) \cdot \boldsymbol{n}\, dS\,. \tag{A.8}$$

This is reminiscent of the familiar statement of Stokes' theorem (A.2a) but with the vector $\boldsymbol{v}$ (of rank 1) generalized to the tensor $\boldsymbol{T}$ (of rank n). There is no ambiguity when the expression is written in suffix notation, as in (A.7).

To transform the circulation integral $\oint_C \sigma \boldsymbol{t}_s ds$ of (A.1) to a surface integral via (A.7), note that $\boldsymbol{t}_s = \boldsymbol{t}_c \times \boldsymbol{n}$. The i-component of the circulation integral therefore becomes

$$\left(\oint_C \sigma \boldsymbol{t}_s ds\right)_i = \oint_C \epsilon_{ijk}\, \sigma\, n_k\, t_{cj}\, ds = -\iint_S \epsilon_{jlm} \frac{\partial}{\partial x_l} (\epsilon_{ijk} \sigma n_k) n_m\, dS\,, \tag{A.9}$$

where in (A.7) $t_j = t_{cj}$ and $T_{ij} = \epsilon_{ijk}\sigma n_k$. Next, since $-\epsilon_{jlm}\epsilon_{ijk} = \epsilon_{lmj}\epsilon_{jik} = \delta_{il}\delta_{km} - \delta_{im}\delta_{kl}$, the integrand in the surface integral of (A.9) is

$$\frac{\partial}{\partial x_i}(\sigma n_k)n_k - \frac{\partial}{\partial x_k}(\sigma n_k)n_i = \frac{\partial \sigma}{\partial x_i} - \sigma\frac{\partial n_k}{\partial x_k}n_i\,, \tag{A.10}$$

which has been simplified: since $\boldsymbol{n}$ is a unit vector, $n_k n_k = 1$ and $n_k \partial_{x_i} n_k = 0$, and since σ is defined only on the surface its derivative in the normal direction $n_k \partial_{x_k}\sigma = 0$. The divergence of the normal field is the sum of the principal curvatures, so that $\partial_{x_k} n_k = \nabla \cdot \boldsymbol{n} = \kappa_1 + \kappa_2$, and in vector notation the integrand becomes

$$\nabla_s \sigma - \sigma(\kappa_1 + \kappa_2)\boldsymbol{n}\,. \tag{A.11}$$

The surface integral that results from this application of Stokes' theorem is substituted in (A.1), the two surface integrals over S_c are then combined, and, since the patch S_c is arbitrary, the integrand, which is assumed to be continuous, is zero. After moving the surface tension terms to the right-hand side, the stress-balance boundary condition (2.3) is found, namely

$$[\boldsymbol{\sigma}]_1^2 \cdot \boldsymbol{n} = \sigma(\kappa_1 + \kappa_2)\boldsymbol{n} - \nabla_s \sigma\,. \tag{A.12}$$

A.2 The Direction of the Marangoni Stress

This section gives an explanation as to why the surface diffusion term in the conservation law for evolution of the surface surfactant concentration Γ can usually be neglected.

In nondimensional form and in the absence of surfactant solubility effects the conservation of surface surfactant Γ is governed by equation (2.14) without the term $\pm J\,\boldsymbol{n} \cdot \nabla C|_S$, that is, for a 2D interface S in 3D space

$$\left.\frac{\partial \Gamma}{\partial t}\right|_{\boldsymbol{n}} + \nabla_s \cdot (\Gamma \boldsymbol{u}_s) + \Gamma(\kappa_1 + \kappa_2)u_n = \frac{1}{Pe_s}\nabla_s^2 \Gamma\,, \quad \boldsymbol{x} \in S. \tag{A.13}$$

where κ_1 and κ_2 are the principal curvatures. To estimate the surface Péclet number $Pe_s = Ua/D_s$, we note that it is widely believed that values of the surface diffusivity D_s and bulk surfactant diffusivity D can be considered nearly equal, and most data is given for D, see for example [6, 10]. We therefore consider $D_s = D$ and $Pe_s = Pe = Ua/D$. The capillary velocity U was introduced in Table 2.2 as $U = \sigma_0/\mu_2$, where σ_0 is the surfactant-free surface tension and μ_2 is the viscosity of the exterior fluid or continuous phase. In practice, surfactant-induced interface velocities are limited by the viscosity of the more viscous fluid and this is observed here.

A two-phase fluid pair of water and a light oil, such as light mineral oil or olive oil, has a surface tension $\sigma_0 \simeq 20$ to 50 mN/m, and oils have the larger viscosity $\mu \simeq 0.04$ to 0.1 kg/m s. This gives a range of the capillary velocity U from about 0.2 to 1.25 m/s, and we choose 0.5 m/s as a typical value. For an air-water interface $\sigma_0 \simeq 73$ mN/m and water has the greater viscosity $\mu \simeq 1.1 \times 10^{-3}$ kg/m s, which gives a larger capillary velocity estimate of 66 m/s.

The quantity D/a is a measure of the velocity at which surfactant can diffuse. Possibly the most comprehensive survey of surfactant data is reference [6], which gives values of D for many surfactants that all lie in the range from 2×10^{-10} to 8×10^{-10} m^2/s. Data for a few larger values of D are considered unreliable. This data is for air-water, with D measured in the water phase, but of the limited data available for D in an oil-water system reference [1], for example, gives a typical value of 4×10^{-10} m$^2/s$. Note that these small diffusivities reflect the fact that surfactant molecules are large, typically of 200 to 2,000 amu, and have long hydrocarbon tails relative to their lighter and more compact host solvent molecules. We take $D = 5 \times 10^{-10}$ m^2/s as a representative value, and a size of $a = 1$ mm, which is larger than the scale of many microfluidic systems but does not overestimate the diffusion velocity D/a of most applications. This gives an estimate for the diffusion velocity in oil-water and air-water systems of 5×10^{-7} m/s.

The result of these estimates is that both the surface and bulk Péclet numbers are of the order of 10^6 for oil-water and 1.3×10^8 for air-water systems. Equivalently, the dimensionless diffusion coefficient, Pe_s^{-1} or Pe^{-1}, is small and of the order of 10^{-6} to 10^{-8}. Because of this, the diffusion term for the evolution of the surface concentration Γ and for the bulk concentration C only needs to be retained if it is needed to resolve large spatial gradients (i.e., near discontinuities or "shocks") in Γ or C.

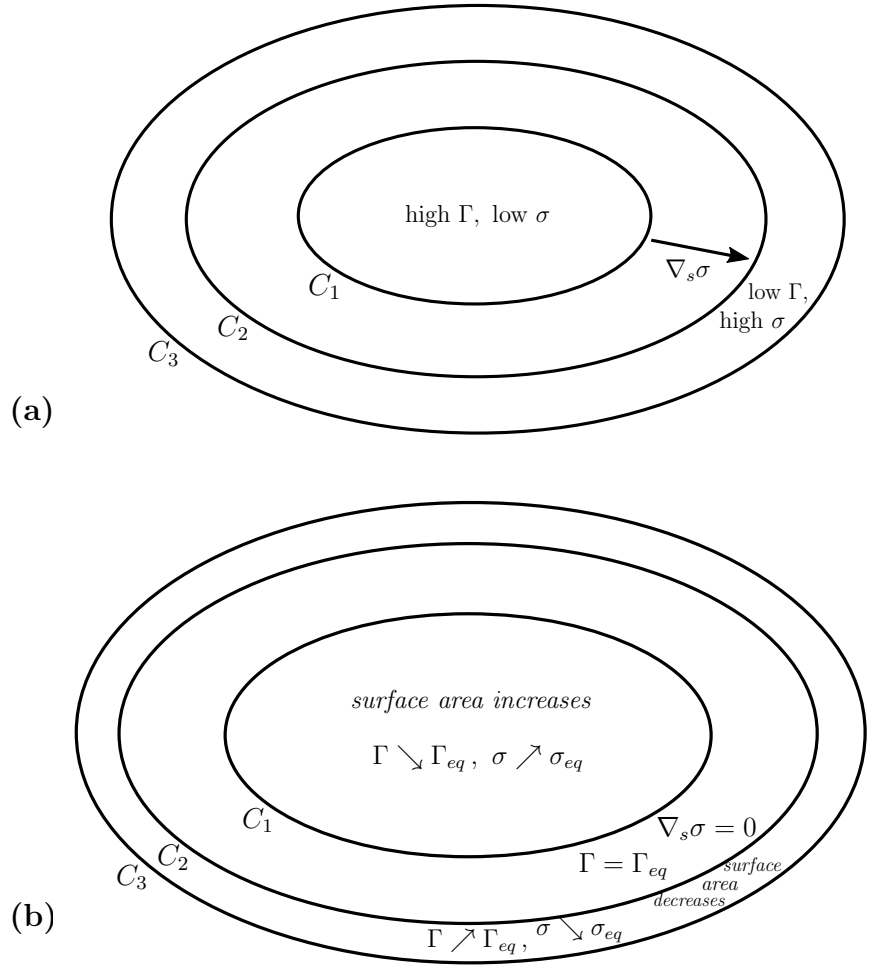

Figure A.2 C_1, C_2, and C_3 are concentric circles of material points or Lagrangian fluid markers on a flat interface. When surfactant is introduced to the area enclosed by C_1 a surface tension gradient with Marangoni stress $\nabla_s\sigma$ is set up that acts outward, as shown. The subsequent flow reduces the gradient and restores equilibrium without diffusion.

However, the direction in which the Marangoni stress acts tends to reduce spatial gradients in the surface concentration Γ. For large spatial gradients of Γ to form, an externally imposed flow or other nonequilibrium condition of sufficient strength must be in place to make it occur. A simple and familiar "kitchen sink" experiment illustrates how Marangoni stress, when it acts on its own, reduces gradients in surface surfactant concentration Γ and surface tension σ to restore a spatially uniform equilibrium: a bounded container of water that is at rest below still air has a flat air-water interface; it is driven away from this initial equilibrium state by placing surfactant on the surface at time $t = 0^+$. A schematic is shown in Figure A.2.

In the figure C_1, C_2, and C_3 are concentric circles of material points or Lagrangian fluid markers on a fluid interface that is initially flat, and remains flat when inertia effects are neglected. So that, in equation (A.14) $\kappa_1 = \kappa_2 = u_n = 0$ and, as shown in Appendix C.2, the time derivative $\partial_t|_n = \partial_t$. The surfactant introduced at time $t = 0^+$ is placed at or near the center of C_1. Surface diffusion on its own would cause this initial distribution to spread out toward a uniform equilibrium state, but at a velocity of order D/a, which is much slower than the capillary velocity $U = \sigma_0/\mu$, as just shown. When the surface diffusion term is neglected (i.e., $Pe_s = \infty$) the evolution equation reduces to conservation of the scalar concentration Γ in the 2D interfacial velocity field $\boldsymbol{u}_s$, namely

$$\frac{\partial \Gamma}{\partial t} + \nabla_s \cdot (\Gamma \boldsymbol{u}_s) = 0\,, \quad \boldsymbol{x} \in S. \tag{A.14}$$

An application of the surface version of Reynold's transport theorem [7, 23] then gives the relations

$$\frac{d}{dt}\int_{A(t)} \Gamma dS = 0\,, \quad \text{or equivalently } \int_{A(t)} \Gamma dS = \text{ constant in time}\,, \tag{A.15}$$

where $A(t)$ is any Lagrangian or material interface area, that is, any area on the interface that moves with the interfacial fluid velocity $\boldsymbol{u}_s$.

The surface equation of state that relates surface surfactant concentration Γ to surface tension σ is monotone decreasing. Thermal effects are neglected here, and this monotinicity is independent of choice of isotherm or a specific surface equation of state. Hence,

$$\sigma = \sigma(\Gamma) > \sigma_{\min} > 0 \quad \text{and } \Gamma \geq 0 \text{ with } \sigma_0 = \sigma(0)\,, \tag{A.16}$$

where $\sigma_{\min}$ is some positive minimum value that can be achieved in practice by use of surfactants.

Suppose that for $t < 0$ the interface has some small initial uniform distribution of surfactant Γ_1 with corresponding equilibrium surface tension $\sigma_1 = \sigma(\Gamma_1)$. When at $t = 0^+$ the surfactant source is supplied inside C_1, the local increase in Γ leads to a local decrease in σ. This sets up a surface gradient of surface tension with Marangoni stress $\nabla_s\sigma$ that is directed away or outward from C_1, see Figure A.2(a). The region of greater surface tension outside C_1, around C_2 and C_3 for example, pulls or draws out the interface within C_1, so that, as sketched in Figure A.2(b), the surface area within C_1 increases. At the same time, the interfacial area bounded by C_2 and C_3 decreases.

Now observe from equation (A.15) that in the flow that develops, since the area enclosed by C_1 increases the surfactant concentration there decreases, and conversely the surfactant concentration enclosed between C_2 and C_3 increases. The spatial gradient of both Γ and σ therefore decreases, with the interface velocity beginning to decrease until finally a new spatially uniform equilibrium is reached with $\boldsymbol{u}_s = 0$ and $\sigma_{eq} = \sigma(\Gamma_{eq})$ constant on the interface.

If the initial surfactant concentration $\Gamma_1 = 0$, then $\int_{C_3 \setminus C_2} \Gamma dS = 0$ and in a bounded container the area enclosed between C_2 and C_3 tends to zero as the final equilibrium is reached. Also, the reasoning above would still apply to a non planar interface that could somehow remain static throughout the motion, since then $u_n = 0$.

For example, a spherical interface that retains its shape because the force balance is dominated by capillary pressure, σ/a.

APPENDIX B

DERIVATION OF SOME RESULTS FROM CHAPTER 3

B.1 Physical Quantities in Terms of Goursat Functions

This section gives the expressions for the primitive variables $\boldsymbol{u}$ and p and the other physical quantities that are derived from them in terms of the Goursat functions, $f(z)$ and $g(z) = h'(z)$. Since the time dependence of these quantities only enters parametrically, it is suppressed here; i.e., the independent variable t is omitted from the argument of all functions.

As noted in Section 3.3 of the main text, in fact the interior domain (Ω_1) and exterior domain (Ω_2) each have distinct pairs of Goursat functions, and, because of the viscosity mismatch, the expressions for the physical quantities in terms of their respective Goursat functions differs. However, the difference is slight. Inspection of the governing equations shows the only difference is that the expression for the pressure on the interior domain is given by replacing the pressure p on the exterior domain by p/λ, while noting the difference in Goursat functions. Cognizant of this, the results listed here are given for the exterior domain Ω_2 alone.

Equation (3.6) for the representation of the stream function ψ in terms of $f(z)$ and $h(z)$ can be rewritten as

$$\psi = \frac{1}{2}\left(\overline{z}f(z) + z\overline{f(z)} + h(z) + \overline{h(z)}\right) . \tag{B.1}$$

In general, if $w(z) = u(x_1, x_2)+iv(x_1, x_2)$ is analytic, from the definition of analyticity and with a prime denoting a derivative with respect to the argument

$$w'(z) = \partial_{x_1}(u + iv) = -i\partial_{x_2}(u + iv) . \tag{B.2}$$

Now $\overline{w(z)}$, like $\overline{z}$, is not analytic, but it follows from equation (B.2) that

$$\partial_{x_1}\overline{w(z)} = \partial_{x_1}u - i\partial_{x_1}v = \overline{w'(z)}\,, \tag{B.3a}$$

$$\text{and} \quad -i\partial_{x_2}\overline{w(z)} = -i\partial_{x_2}u - \partial_{x_2}v = -\overline{w'(z)}\,. \tag{B.3b}$$

With $g(z) \equiv h'(z)$, the first and second derivatives of the stream function are therefore,

$$\partial_{x_1}\psi(x_1,x_2) = \frac{1}{2}\left(f(z) + \overline{z}f'(z) + \overline{f(z)} + z\overline{f'(z)} + g(z) + \overline{g(z)}\right)\,, \tag{B.4a}$$

$$\partial_{x_2}\psi(x_1,x_2) = \frac{i}{2}\left(-f(z) + \overline{z}f'(z) + \overline{f(z)} - z\overline{f'(z)} + g(z) - \overline{g(z)}\right)\,, \tag{B.4b}$$

$$\partial^2_{x_1}\psi(x_1,x_2) = \frac{1}{2}\left(2f'(z) + \overline{z}f''(z) + 2\overline{f'(z)} + z\overline{f''(z)} + g'(z) + \overline{g'(z)}\right)\,, \tag{B.4c}$$

$$\partial^2_{x_2}\psi(x_1,x_2) = \frac{1}{2}\left(2f'(z) - \overline{z}f''(z) + 2\overline{f'(z)} - z\overline{f''(z)} - g'(z) - \overline{g'(z)}\right)\,, \tag{B.4d}$$

$$\partial^2_{x_1x_2}\psi(x_1,x_2) = \frac{i}{2}\left(\overline{z}f''(z) - z\overline{f''(z)} + g'(z) - \overline{g'(z)}\right)\,. \tag{B.4e}$$

The velocity components are given in terms of the stream function by equation (3.1), namely

$$u_1 = \partial_{x_2}\psi \quad \text{and} \quad u_2 = -\partial_{x_1}\psi\,. \tag{B.5}$$

A 2D vector, and here the fluid velocity is the relevant example, can be written in terms of its Cartesian components as $\boldsymbol{u} = (u_1, u_2)$ or associated with its complex counterpart $u = u_1 + iu_2$. So, for the complex velocity u, $iu = -u_2 + iu_1 = \partial_{x_1}\psi + i\partial_{x_2}\psi$, and hence, from equations (B.4a,b), in terms of the Goursat functions,

$$iu = -u_2 + iu_1 = f(z) + z\overline{f'(z)} + \overline{g(z)}\,, \tag{B.6}$$

which is equation (3.7).

In Cartesian 2D Stokes flow the fluid vorticity can be represented by a scalar q, where $\boldsymbol{\omega} = \nabla\times\boldsymbol{u} = q\boldsymbol{e}_3$, and in terms of the velocity components and stream function

the vorticity scalar $q = \partial_{x_1} u_2 - \partial_{x_2} u_1 = -\nabla^2 \psi$. Hence, from equations (B.4c,d),

$$q = -2(f'(z) + \overline{f'(z)}) = -4Re\, f'(z)\,. \tag{B.7}$$

The conjugate harmonic function of q is the pressure p in Ω_2. In terms of its Cartesian components, the Stokes momentum equation can be written as

$$\nabla^2(u_1, u_2) = (\partial_{x_2}, -\partial_{x_1})\nabla^2\psi = (-\partial_{x_2}, \partial_{x_1})q = (\partial_{x_1}, \partial_{x_2})p\,, \tag{B.8}$$

where sufficient smoothness to commute derivatives has been assumed. Hence, q and p satisfy the Cauchy-Riemann equations

$$\partial_{x_1} q = \partial_{x_2} p \quad \text{and} \quad \partial_{x_2} q = -\partial_{x_1} p\,, \tag{B.9}$$

and since their first partial derivatives are assumed to be continuous $q + ip$ is an analytic function of z. From (B.7), we have

$$q + ip = -4f'(z) \quad \text{and} \quad p = -4\, Im\, f'(z)\,. \tag{B.10}$$

The components of the rate of strain tensor for a Newtonian fluid are

$$e_{ij} = \frac{1}{2}\left(\frac{\partial u_i}{\partial x_j} + \frac{\partial u_j}{\partial x_i}\right) \quad i, j = 1, 2\,. \tag{B.11}$$

When these are written in terms of the stream function, via equations (B.5), and relations (B.4c-e) are used, it is found that

$$e_{11} = \partial^2_{x_1 x_2}\psi = \frac{i}{2}\left(\overline{z} f''(z) - z\overline{f''(z)} + g'(z) - \overline{g'(z)}\right)\,, \tag{B.12a}$$

$$e_{12} = \frac{1}{2}(\partial^2_{x_2} - \partial^2_{x_1})\psi = -\frac{1}{2}\left(\overline{z} f''(z) + z\overline{f''(z)} + g'(z) + \overline{g'(z)}\right)\,, \tag{B.12b}$$

from which it follows that

$$e_{11} + ie_{12} = -i\left(z\overline{f''(z)} + \overline{g'(z)}\right)\,, \tag{B.13}$$

and since $e_{21} = e_{12}$ and $e_{11} = -e_{22}$, we have

$$e_{11} + ie_{12} = -e_{22} + ie_{21}\,. \tag{B.14}$$

The Stress-Balance Boundary Condition on S

The stress exerted by the fluid in the exterior domain Ω_2 on the interface S appears as the terms on the left-hand side of the stress-balance boundary condition (2.12b) with a 2-subscript. The subscript is dropped here, and in terms of its Cartesian components the stress contribution is $\boldsymbol{f} = (f_1, f_2)$, where

$$f_i = -pn_i + 2e_{ij}n_j\,, \quad i = 1, 2\,. \tag{B.15}$$

In complex form this is $f = f_1 + if_2$, and the outward unit normal is $n = n_1 + in_2$, so that from equations (B.10), (B.13), and (B.14),

$$f = 4\,Im\,(f'(z))n - 2i\left(z\overline{f''(z)} + \overline{g'(z)}\right)\overline{n}\,, \tag{B.16}$$

where $z \in S$.

With the convention that S is traversed with arc length s increasing in the counter-clockwise direction, at an arbitrary point z on S we have

$$\text{unit tangent } z_s = \frac{dz}{ds} \text{ and outward unit normal } n = -iz_s\,, \tag{B.17}$$

as sketched in Figure B.1 (compare with Figure 2.1 of Section 2.1 and Figure 3.1 of Section 3.4 of the main text). So that in terms of z_s,

$$f = -2\left\{(f'(z) - \overline{f'(z)})z_s - (z\overline{f''(z)} + \overline{g'(z)})\overline{z}_s\right\}\,. \tag{B.18}$$

In general, if $w(z)$ is an analytic function of z then along a smooth path in the complex plane $\frac{dw}{ds} = \frac{dw}{dz}\frac{dz}{ds} = w'(z)z_s$, and by forming the complex conjugate, $\frac{d\overline{w}}{ds} = \overline{w'(z)}\overline{z}_s$. From this, we have the exterior fluid stress

$$f = -2\frac{d}{ds}\left\{f(z) - z\overline{f'(z)} - \overline{g(z)}\right\} \quad z \in S\,, \tag{B.19}$$

which is a perfect derivative with respect to the arc length s.

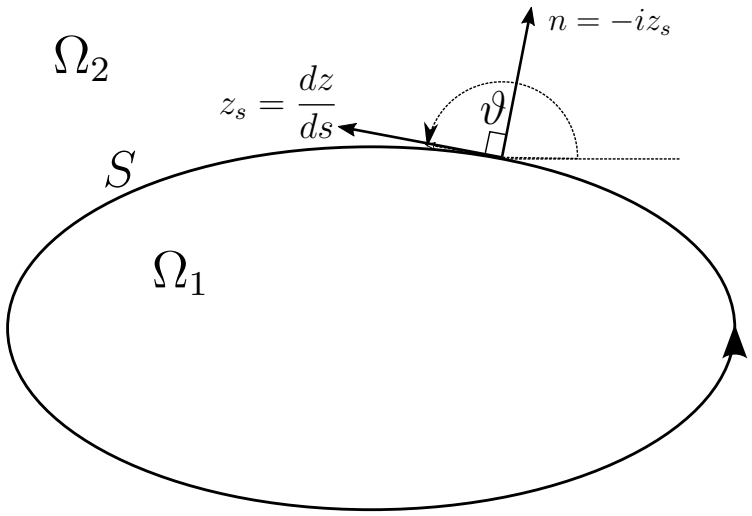

Figure B.1 The interface S is traversed with arc length s increasing in the counter-clockwise direction, so that the unit tangent $z_s = \frac{dz}{ds}$, outward normal $n = -i\, z_s$, and angle ϑ from the positive x_1-axis to the tangent are as shown.

An analogous result holds for the stress exerted by the fluid in the interior domain Ω_1 on the interface, except that: (i) since p is replaced by p/λ in equation (B.10) and the interior viscous stress carries a factor λ, the interior fluid stress is multiplied by a factor of λ, and (ii) the direction of the normal is reversed.

The contribution of the surface tension σ to the stress-balance boundary condition, at equations (A.12) or (2.12b), was derived with the convention that the principal curvatures κ_1 and κ_2 in 3D or the curvature κ in 2D are positive when S is viewed from Ω_2, i.e., from the side of S to which n points, which in 2D gives the complex version of the Frenet-Serret formula

$$\frac{d^2 z}{ds^2} = -\kappa n\,. \tag{B.20}$$

In passing, we note that if the angle between the positive x_1 axis and the unit tangent z_s measured counter-clockwise positive is denoted by ϑ, as sketched in Figure B.1,

then $z_s = e^{i\vartheta}$ and the outward unit normal is $n = -ie^{i\vartheta}$. Hence, $z_{ss} = ie^{i\vartheta}\vartheta_s = -\vartheta_s n$, and from equation (B.20) the relation $\kappa = \frac{\partial \vartheta}{\partial s}$ follows.

When written on the right-hand side of the stress-balance boundary condition (2.12b) in vector form, the contribution of surface tension forces to the net stress is $\sigma\kappa\boldsymbol{n} - \nabla_s\sigma$, or in complex form

$$\sigma\kappa n - \frac{d\sigma}{ds}z_s = -\sigma z_{ss} - \frac{d\sigma}{ds}z_s = -\frac{d}{ds}(\sigma z_s)\,, \tag{B.21}$$

where the simplification to a perfect derivative has used relation (B.20).

Recall that the interior and exterior fluid domains each have a distinct pair of Goursat functions, in the sense that the pair that are analytic on Ω_1 are not given by analytic continuation of the pair that are analytic on Ω_2 and vice-versa. Therefore, to evaluate the fluid stress on S due to the fluid in the exterior domain Ω_2 from relation (B.19), the limit is taken as z approaches an arbitrary point on S, which we now call τ, as z tends to $\tau \in S$ from Ω_2. This is written $\lim z \to \tau^+$ and termed an exterior limit. Similarly, for the contribution to the interior fluid stress, the limit $\lim z \to \tau^-$ from Ω_1 is taken and termed an interior limit.

When the fluid stress and surface tension contributions to the stress-balance (2.12b), each of which is a perfect derivative with respect to s, are pieced together, an integration with respect to s gives the relation

$$\lim_{z\to\tau^+}\left\{f(z) - z\overline{f'(z)} - \overline{g(z)}\right\} - \lambda \lim_{z\to\tau^-}\left\{f(z) - z\overline{f'(z)} - \overline{g(z)}\right\} = \frac{1}{2}\sigma\frac{\partial \tau}{\partial s} \tag{B.22}$$

for all $\tau \in S$. Here, a sign has been absorbed and freedom of choice in specifying the Goursat functions allows a function of time that results from the integration over s to be set to zero.

B.2 Derivation of the Sherman-Lauricella Integral Equation

In this section, the time dependence of quantities such as the Goursat functions is restored.

From equation (2.20) for the far-field velocity, the pressure p and vorticity scalar q have the behavior

$$p = p_\infty + \mathcal{O}(|z|^{-3})\,, \tag{B.23a}$$

$$q = -G + \mathcal{O}(|z|^{-3})\,, \tag{B.23b}$$

as $|\boldsymbol{x}| \to \infty$ and equivalently $|z| \to \infty$. The leading terms here are given by consideration of the imposed linear flow and the remainder terms correspond to the presence of the drop. Also, since p_∞ is a constant it can be set to zero without loss of generality, i.e., $p_\infty = 0$. The far-field behavior of the quantity $q + ip$ on the left-hand side of equation (B.10) is therefore $q + ip = -G + \mathcal{O}(|z|^{-3})$, from which

$$f(z,t) = \frac{G}{4} z + H(t) + \mathcal{O}(|z|^{-2})\,, \tag{B.24}$$

where $H(t)$ is an as yet arbitrary function of time. Similarly, the far-field velocity of equation (2.20) implies that the quantity $-u_2 + iu_1$ on the left-hand side of equation (B.6) has the behavior

$$-u_2 + iu_1 = (-B + iQ)\overline{z} + \frac{G}{2} z + \mathcal{O}(|z|^{-2})\,, \tag{B.25}$$

as $|z| \to \infty$, from which

$$g(z,t) = -(B + iQ)z - \overline{H(t)} + \mathcal{O}(|z|^{-2}) \;\text{ as } |z| \to \infty\,. \tag{B.26}$$

In the Sherman-Lauricella formulation, the Goursat functions on both Ω_1 and Ω_2 contain Cauchy-type integrals over S that contain a single complex density $\omega(z,t)$ and represent the disturbance to the imposed flow caused by the presence of the drop

exactly. To be specific, on Ω_1 and Ω_2,

$$f(z,t) = \frac{1}{2\pi i}\int_S \frac{\omega(\xi,t)}{\xi - z}d\xi + \frac{G}{4}z + H(t)\,, \tag{B.27a}$$

$$g(z,t) = \frac{1}{2\pi i}\int_S \frac{-\overline{\omega(\xi,t)}d\xi + \omega(\xi,t)\overline{d\xi}}{\xi - z} - \frac{1}{2\pi i}\int_S \frac{\overline{\xi}\,\omega(\xi,t)}{(\xi - z)^2}d\xi$$
$$- (B + iQ)z - \overline{H(t)}\,, \tag{B.27b}$$

where the density $\omega(z,t)$ is to be found.

To find the density $\omega(z,t)$, expressions (B.27) for the Goursat functions $f(z,t)$ and $g(z,t)$ are substituted into the integrated form of the stress-balance boundary condition (B.22), and evaluated at a general point $\tau \in S$ in the limits $z \to \tau^+$ and $z \to \tau^-$ described near the end of Section B.1. The first step toward this is to substitute expressions (B.27) into the terms of the first limit of equation (B.22). For a general point z in Ω_1 or Ω_2 this gives

$$\begin{aligned} &f(z) - z\overline{f'(z)} - \overline{g(z)} \\ &= \frac{1}{2\pi i}\int_S \frac{\omega(\xi,t)}{\xi - z}d\xi - \frac{1}{2\pi i}\int_S \frac{\omega(\xi,t)}{\overline{\xi} - \overline{z}}d\overline{\xi} + \frac{1}{2\pi i}\int_S \frac{\overline{\omega(\xi,t)}}{\overline{\xi} - \overline{z}}d\xi \\ &+ \frac{1}{2\pi i}\int_S \frac{(z - \xi)\overline{\omega(\xi,t)}}{(\overline{\xi} - \overline{z})^2}d\overline{\xi} + (B - iQ)\overline{z} + 2H(t)\,. \end{aligned} \tag{B.28}$$

The Cauchy-type integrals on the right-hand side of this relation have apparent singularities that are integrable as z approaches $\tau \in S$ from either side of the contour, i.e., in the limit $z \to \tau^{\pm}$. To evaluate these limits, the contour S is deformed by introducing a small semi-circular indentation, centered on $z = \tau$ with radius r and orientation consistent with the counterclockwise orientation around the remainder of S, as shown in Figure B.2. On the indentation $\xi = \tau + re^{i\phi}$ with τ fixed, so that

$$\frac{d\xi}{\xi - \tau} = i\,d\phi \quad \text{and} \quad \frac{d\overline{\xi}}{\overline{\xi} - \overline{\tau}} = -i\,d\phi\,, \tag{B.29a}$$

$$\text{while} \quad \frac{d\xi}{\overline{\xi} - \overline{\tau}} = i\,e^{2i\phi}d\phi \quad \text{and} \quad \frac{(\tau - \xi)d\overline{\xi}}{(\overline{\xi} - \overline{\tau})^2} = i\,e^{2i\phi}d\phi\,. \tag{B.29b}$$

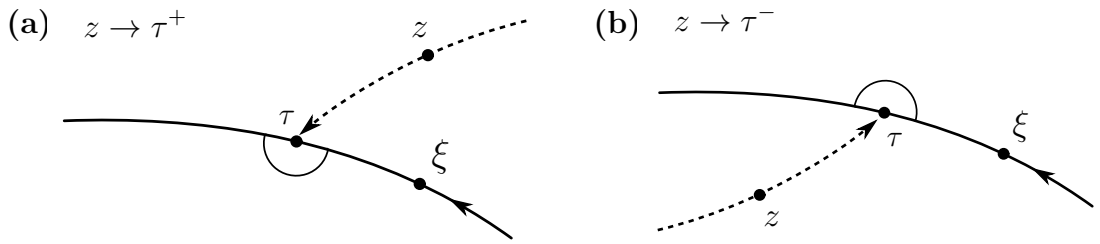

Figure B.2 The contour of integration S is indented as shown: (a) for the exterior limit $z \to \tau^+$, and (b) for the interior limit $z \to \tau^-$. Since all integrals are taken with S traversed counter-clockwise in the complex plane, the orientation on the indentation is clockwise relative to τ when $z \to \tau^+$ and is counter-clockwise relative to τ when $z \to \tau^-$.

On the indentation, ϕ either increases or decreases by π, depending on the orientation of the path in ξ around $z = \tau$. Assuming continuity of $\omega(z,t)$, it follows that of the integrals on the right-hand side of relation (B.28), the first two have local contributions from the indentation of $\pm\omega(\tau,t)/2$ in the limit $r \to 0^+$, per equations (B.29a), while the last two, per equations (B.29b), have zero local contribution since the change in argument of the exponential is $2\pi i$. The results for the first two integrals are summarized by the Plemelj formulae

$$\lim_{z\to\tau^+} \frac{1}{2\pi i}\int_S \frac{\omega(\xi,t)}{\xi - z}d\xi = -\frac{\omega(\tau,t)}{2} + \frac{1}{2\pi i}\fint_S \frac{\omega(\xi,t)}{\xi-\tau}d\xi \tag{B.30a}$$

$$\lim_{z\to\tau^-} \frac{1}{2\pi i}\int_S \frac{\omega(\xi,t)}{\xi - z}d\xi = \frac{\omega(\tau,t)}{2} + \frac{1}{2\pi i}\fint_S \frac{\omega(\xi,t)}{\xi-\tau}d\xi \tag{B.30b}$$

$$\lim_{z\to\tau^+} \frac{1}{2\pi i}\int_S \frac{\omega(\xi,t)}{\overline{\xi} - \overline{z}}d\overline{\xi} = \frac{\omega(\tau,t)}{2} + \frac{1}{2\pi i}\fint_S \frac{\omega(\xi,t)}{\overline{\xi}-\overline{\tau}}d\overline{\xi} \tag{B.30c}$$

$$\lim_{z\to\tau^-} \frac{1}{2\pi i}\int_S \frac{\omega(\xi,t)}{\overline{\xi} - \overline{z}}d\overline{\xi} = -\frac{\omega(\tau,t)}{2} + \frac{1}{2\pi i}\fint_S \frac{\omega(\xi,t)}{\overline{\xi}-\overline{\tau}}d\overline{\xi} \tag{B.30d}$$

where $\fint_S$ denotes a Cauchy principal value integral.

The exterior limit $z \to \tau^+$ of relation (B.28) can now be expressed as

$$\begin{aligned}\lim_{z\to\tau^+} f(z) - z\overline{f'(z)} - \overline{g(z)} \\ = -\,\omega(\tau,t) + \frac{1}{2\pi i}\int_S \omega(\xi,t)\, d\ln\left(\frac{\xi-\tau}{\overline{\xi}-\overline{\tau}}\right) + \frac{1}{2\pi i}\int_S \overline{\omega(\xi,t)}\, d\left(\frac{\xi-\tau}{\overline{\xi}-\overline{\tau}}\right) \\ + (B-iQ)\overline{\tau} + 2H(t)\,, \end{aligned} \tag{B.31}$$

where the integrals of (B.28) that contain $\omega(z,t)$ and the integrals that contain its conjugate $\overline{\omega(z,t)}$ have been grouped together via the identities

$$d\ln\frac{\xi-\tau}{\overline{\xi}-\overline{\tau}} = \frac{d\xi}{\xi-\tau} - \frac{d\overline{\xi}}{\overline{\xi}-\overline{\tau}}\,, \tag{B.32a}$$

$$d\,\frac{\xi-\tau}{\overline{\xi}-\overline{\tau}} = \frac{d\xi}{\overline{\xi}-\overline{\tau}} + \frac{(\tau-\xi)d\overline{\xi}}{(\overline{\xi}-\overline{\tau})^2}\,. \tag{B.32b}$$

Similarly, the interior limit $z \to \tau^-$ of relation (B.28) is

$$\begin{aligned}\lim_{z\to\tau^-} f(z) - z\overline{f'(z)} - \overline{g(z)} \\ = \omega(\tau,t) + \frac{1}{2\pi i}\int_S \omega(\xi,t)\, d\ln\left(\frac{\xi-\tau}{\overline{\xi}-\overline{\tau}}\right) + \frac{1}{2\pi i}\int_S \overline{\omega(\xi,t)}\, d\left(\frac{\xi-\tau}{\overline{\xi}-\overline{\tau}}\right) \\ + (B-iQ)\overline{\tau} + 2H(t)\,. \end{aligned} \tag{B.33}$$

As an aside, we verify that the integrals around S on the right-hand side of relations (B.31) and (B.33) are regular as $\xi \to \tau$, that is, the apparent singularity at $\xi = \tau$ is removable. Introduce an arbitrary parameterization $z = z(\alpha) = x_1(\alpha) + ix_2(\alpha)$ of S in the z-plane. Then $\tau \in S$ is fixed with $\tau = z(\alpha_*)$ and α_* fixed, while $\xi \in S$ traverses the contour with $\xi = z(\alpha)$ and the limit of interest is $\alpha \to \alpha_*$. Then, from equation (B.32a)

$$\lim_{\alpha\to\alpha_*} d\ln\frac{\xi-\tau}{\overline{\xi}-\overline{\tau}} = \lim_{\alpha\to\alpha_*} \frac{2i\,\mathrm{Im}\left((\overline{z(\alpha)}-\overline{z(\alpha_*)})z'(\alpha)\right)}{|z(\alpha)-z(\alpha_*)|^2}d\alpha = \frac{i\,\mathrm{Im}(\overline{z}'z'')|_{\alpha_*}}{|z'|^2_{\alpha_*}}d\alpha\,,$$

where $' \equiv \frac{d}{d\alpha}$ and the limit has been evaluated by applying L'Hôpital's rule twice. In terms of components, this becomes

$$\lim_{\alpha\to\alpha_*} d\ln\frac{\xi-\tau}{\overline{\xi}-\overline{\tau}} = i\,\frac{x_1'x_2''-x_2'x_1''}{x_1'^2+x_2'^2}\bigg|_{\alpha_*} d\alpha = i\,\kappa(\alpha_*)\,\frac{ds}{d\alpha}\bigg|_{\alpha_*} d\alpha = i\kappa ds\,. \tag{B.34}$$

From equation (B.32b)

$$\lim_{\alpha\to\alpha_*} d\frac{\xi-\tau}{\overline{\xi}-\overline{\tau}} = \lim_{\alpha\to\alpha_*} \frac{2i\,\mathrm{Im}\left((\overline{z(\alpha)}-\overline{z(\alpha_*)})z'(\alpha)\right)}{(\overline{z(\alpha)}-\overline{z(\alpha_*)})^2}d\alpha = \frac{i\,\mathrm{Im}(\overline{z'}z'')|_{\alpha_*}}{\overline{z'}^2|_{\alpha_*}}d\alpha\,,$$

after applying L'Hôpital's rule twice. In terms of components, this becomes

$$\lim_{\alpha\to\alpha_*} d\frac{\xi-\tau}{\overline{\xi}-\overline{\tau}} = i\,\frac{x_1'x_2''-x_2'x_1''}{(x_1'^2+x_2'^2)^{3/2}}\bigg|_{\alpha_*}\frac{(x_1'+ix_2')^2}{(x_1'^2+x_2'^2)^{1/2}}\bigg|_{\alpha_*} d\alpha = i\frac{\kappa(\alpha_*)(\frac{d\xi}{d\alpha})^2_{\alpha_*}}{(\frac{ds}{d\alpha})_{\alpha_*}}d\alpha\,. \tag{B.35}$$

The integral equation is found by substituting the exterior limit (B.31) and the interior limit (B.33) into the integrated form of the stress-balance boundary condition (B.22). After minor re-arrangement and restoring z instead of τ as a general point on the interface contour S, this gives

$$\begin{aligned}\omega(z,t) - \frac{\beta}{2\pi i}\int_S \omega(\xi,t)\,d\ln\frac{\xi-z}{\overline{\xi}-\overline{z}} - \frac{\beta}{2\pi i}\int_S \overline{\omega(\xi,t)}\,d\frac{\xi-z}{\overline{\xi}-\overline{z}} \\ -\beta(B-iQ)\overline{z} - 2\beta H(t) = -\frac{\gamma}{2}\sigma(\Gamma)\frac{\partial z}{\partial s}\,.\end{aligned} \tag{B.36}$$

On the right-hand side here, the dependence of the surface tension σ on the surface surfactant concentration Γ has been emphasized, and the parameters β and γ are defined in terms of the viscosity ratio λ by

$$\beta = \frac{1-\lambda}{1+\lambda}\,, \qquad \gamma + \frac{1}{1+\lambda}\,. \tag{B.37}$$

A Note on the Choice of Contour Orientation

Accounts of the Sherman-Lauricella integral equation often choose a clockwise orientation for the integration around S as opposed to the counter-clockwise

orientation chosen here. However, if the same definitions at equations (B.27) are used for the Goursat functions $f(z,t)$ and $g(z,t)$, independently of the choice of contour orientation, then reversal of contour orientation causes a change in sign of the density $\omega(z,t)$. In other words, under the map $s \mapsto -s$ also $\omega(z,t) \mapsto -\omega(z,t)$. When this change of contour orientation and sign of the density are implemented in equation (B.36), and the equation is multiplied throughout by -1, the net effect is that the first term on the left-hand side and the only term on the right-hand side remain unchanged, while all other terms, i.e., the four terms on the left that are multiplied by β, have their sign reversed.

B.3 Construction of the Cauchy Principal Value Integrals

This section gives a description of the numerical method used to evaluate the Cauchy principal value integrals of equations (3.35) and (3.38). The method is usually described as Van de Vooren desingularization, and the account here is based on that by Hou, Lowengrub, and Krasny [15].

Both integrals have the form

$$I(z) = \frac{1}{2\pi i} \int\!\!\!\!\!\!- _S \frac{f(\xi)}{\xi - z} d\xi \,, \tag{B.38}$$

where $f(z)$ is analytic on and in a neighborhood of the closed contour S. The definition of the principal value integral is that it is the limit

$$I(z) = \frac{1}{2\pi i} \lim_{\epsilon \to 0^+} \int_{S \setminus D_\epsilon(z)} \frac{f(\xi)}{\xi - z} d\xi \,, \tag{B.39}$$

where $S \setminus D_\epsilon(z)$ denotes that the same ϵ-neighborhood to both sides of the point z is excised or removed from the domain or path of integration before the limit is formed.

The desingularization method of [15] consists of two parts. First, a function is subtracted from the integrand that: (i) has a simple pole at $\xi = z$ of the same pole strength as the integrand, (ii) is an odd function of $\xi - z$ about the pole location

$\xi = z$, and (iii) is periodic on S. These properties ensure that the subtraction does not alter the value of the integral as defied at (B.39). The desingularization also ensures that near the pole the integrand has modulus of order $\mathcal{O}(1)$, not $\mathcal{O}(|\xi - z|^{-1})$, which reduces numerical error. A suitable elementary function for the subtraction is a scaled cotangent.

To implement the first step, the local behavior of the integrand near $\xi = z$ is needed. To evaluate it, an arbitrary parameterization of the contour S is introduced, namely

$$S: \ \xi = \xi(\alpha)\,, \ \alpha \in [0, 2\pi)\,. \ \text{At } \alpha = a\,, \ \xi(\alpha = a) = z\,. \tag{B.40}$$

In terms of the parameterization, the integral is

$$I(z) = \frac{1}{2\pi i}\oint_S \frac{f(\xi(\alpha))}{\xi(\alpha) - z}\,\frac{d\xi}{d\alpha}\,d\alpha\,. \tag{B.41}$$

The components of the integrand have the following expansions about $\alpha = a$:

$$f(\xi(\alpha)) = f(\xi(a)) + (\alpha - a)\xi'(a)f'(\xi(a)) + \mathcal{O}((\alpha - a)^2)\,, \tag{B.42a}$$

$$\frac{d\xi}{d\alpha}(\alpha) = \xi'(a) + (\alpha - a)\xi''(a) + \mathcal{O}((\alpha - a)^2)\,, \tag{B.42b}$$

$$\frac{1}{\xi(\alpha) - z} = \frac{1}{\xi(\alpha) - \xi(a)} = \frac{1}{(\alpha - a)\xi'(a)} - \frac{\xi''(a)}{2\xi'^2(a)} + \mathcal{O}((\alpha - a))\,, \tag{B.42c}$$

from which

$$\frac{f(\xi(\alpha))}{\xi(\alpha) - z}\,\frac{d\xi}{d\alpha} = \frac{f(\xi(a))}{\alpha - a} + \left(\frac{f(\xi(a))\xi''(a)}{2\xi'(a)} + f'(\xi(a))\xi'(a)\right) + \mathcal{O}(\alpha - a)\,. \tag{B.43}$$

The desingularized integrand is therefore,

$$\frac{f(\xi(\alpha))\xi'(\alpha)}{\xi(\alpha) - \xi(a)} - \frac{f(\xi(a))}{2}\cot\left(\frac{\alpha - a}{2}\right)\,. \tag{B.44}$$

The trapezoidal rule is used to evaluate the integral, with N points $\{\alpha_k : k = 1, 2, \ldots N\}$ evenly distributed in α, so that $\alpha_k = (k-1)h$ with step size $h = 2\pi/N$.

If the pole is located at the mesh point where $k = j$ then $\alpha_j = a$ and $z = \xi(\alpha_j)$, and this mesh point is excluded from the sum in the trapezoidal rule. Instead, at this point the desingularized integrand (B.44) is approximated by the leading $\mathcal{O}(1)$ term in its expansion, which is given by the second group of terms on the right-hand side of equation (B.43). This gives the following expression for the trapezoidal rule approximation of the integral (B.38)

$$J_h(z) = \frac{h}{2\pi i} \sum_{\substack{k=1 \\ k\neq j}}^{N} \left\{ \frac{f(\xi(\alpha_k))\xi'(\alpha_k)}{\xi(\alpha_k) - \xi(\alpha_j)} - \frac{f(\xi(\alpha_j))}{2} \cot\left(\frac{\alpha_k - \alpha_j}{2}\right) \right\} + \frac{h}{2\pi i} \mathcal{F}(f(\xi), \xi(\alpha_j))$$

$$\text{where } \mathcal{F}(f(\xi), \xi(\alpha_j)) = \frac{f(\xi(\alpha_j))\xi''(\alpha_j)}{2\xi'(\alpha_j)} + f'(\xi(\alpha_j))\xi'(\alpha_j)\,. \tag{B.45}$$

Since the local term $\mathcal{F}(f(\xi), \xi(\alpha_j))$ contains higher order derivatives it may be difficult to compute accurately. However, it can be eliminated by using the same quadrature with twice the step size, $2h$, and half of the N mesh points. This is the second part of the desingularization method of [15]. With N even, the sum over k excludes the mesh point α_j at which the pole $z = \xi(\alpha_j)$ occurs, and is taken over even integer k only when j is even and is taken over odd integer values of k only when j is odd. This gives

$$J_{2h}(z) = \frac{2h}{2\pi i} \sum_{\substack{k \text{ even or} \\ k \text{ odd}, k\neq j}}^{N} \left\{ \frac{f(\xi(\alpha_k))\xi'(\alpha_k)}{\xi(\alpha_k) - \xi(\alpha_j)} - \frac{f(\xi(\alpha_j))}{2} \cot\left(\frac{\alpha_k - \alpha_j}{2}\right) \right\}$$

$$+ \frac{2h}{2\pi i} \mathcal{F}(f(\xi), \xi(\alpha_j))\,. \tag{B.46}$$

The linear combination $2J_h(z) - J_{2h}(z)$ eliminates the local term and gives the numerical approximation to the principal value integral

$$I(z) \simeq 2J_h(z) - J_{2h}(z) = \frac{h}{\pi i} \begin{cases} \sum_{k=1}^{N/2} A(\xi(\alpha_{2k-1})) & j \text{ even} \\ \sum_{k=1}^{N/2} A(\xi(\alpha_{2k})) & j \text{ odd}\,, \end{cases} \tag{B.47a}$$

$$\text{where } A(\xi(\alpha_k)) = \frac{f(\xi(\alpha_k))\xi'(\alpha_k)}{\xi(\alpha_k) - \xi(\alpha_j)} - \frac{f(\xi(\alpha_j))}{2} \cot\left(\frac{\alpha_k - \alpha_j}{2}\right)\,. \tag{B.47b}$$

It is pointed out in [15] that the end result (B.47) is a mid-point rule quadrature method with step size $2h$, and that, like the trapezoidal rule, since the integrand is periodic for $\alpha \in [0, 2\pi)$ it is spectrally accurate.

APPENDIX C

DERIVATION OF SOME RESULTS FROM CHAPTER 4

C.1 The Fourier and Chebyshev Spectral Differentiation Matrices D_r and D_θ

The Fourier spectral differentiation matrix D_θ of Section 4.2.1 is the matrix D_N of [34], page 5 equation (1.5), or page 21 equation (3.10). It is dense and has banded diagonal, circulant or Toeplitz structure, and is of size $N_\theta \times N_\theta$.

It can be written as

$$D_\theta = \begin{pmatrix} & \vdots & \\ \ddots & \frac{1}{2}\cot(\frac{3h}{2}) & \\ \ddots & \frac{-1}{2}\cot(\frac{2h}{2}) & \\ \ddots & \frac{1}{2}\cot(\frac{1h}{2}) & \\ & 0 & \\ & \frac{-1}{2}\cot(\frac{1h}{2}) & \ddots \\ & \frac{1}{2}\cot\left(\frac{2h}{2}\right) & \ddots \\ & \frac{-1}{2}\cot\left(\frac{3h}{2}\right) & \ddots \\ & \vdots & \end{pmatrix} \tag{C.1}$$

where $h = 2\pi/N_\theta$ and N_θ (even) is the number of points in the azimuthal direction.

The Chebyshev spectral differentiation matrix D_r of Section 4.2.1 is the matrix D_N of [34], Theorem 7 page 53, with N_r substituted for N, and with the radial coordinate r and Chebyshev-Lobatto points r_i substituted for x and x_i. It is of size

$(N_r+1)\times(N_r+1)$ and has entries indexed from 0 to N_r as follows:

$$
\begin{aligned}
&(D_r)_{00} = (2N_r^2+1)/6\,, \qquad (D_r)_{N_rN_r} = -(2N_r^2+1)/6\,,\\
&(D_r)_{jj} = \frac{-r_j}{2(1-r_j^2)}\,, \quad j = 1,2,...,N_r-1\,,\\
&(D_r)_{ij} = \frac{c_i}{c_j}\frac{(-1)^{i+j}}{(r_i-r_j)}\,,\ i\neq j,\ i,j = 0,1,...,N_r\,,\\
&\text{where } c_i = \begin{cases} 2 & i = 0 \text{ or } N_r \\ 1 & \text{otherwise} \end{cases}
\end{aligned}
\tag{C.2}
$$

C.2 Expression of the Material Derivative in the Eulerian and Intrinsic Coordinate Frames

This section describes construction of the material derivative in the intrinsic or surface-fitted coordinate frame, given the material derivative in the Eulerian frame. The expression in the intrinsic frame is needed for the narrow ϵ-layer analysis to find the bulk surfactant concentration C in the transition layer of the hybrid method. The final result is that in the intrinsic frame the material derivative is

$$\partial_t + \boldsymbol{v}_s\cdot\nabla_s + \partial_n v_p|_S N\partial_N + \mathcal{O}(\epsilon)\,. \tag{C.3}$$

To be more specific, the terms of expression (C.3) that are written out explicitly are the leading order terms with respect to ϵ, where $0<\epsilon\ll 1$, of the material derivative in the ϵ-layer adjacent to an evolving interface S, and $\boldsymbol{v}_s$ and $\partial_n v_p|_S n$, where $n=\epsilon N$, are leading order quantities in ϵ that are defined below. However, ϵ-expansions and related subscripts are omitted, and we concentrate first on the change of variables or change of coordinate frame in three space dimensions. The last term, $\partial_n v_p|_S N\partial_N$, can be recast but still contains $\partial_n v_p|_S$.

1) The Eulerian (or lab) frame has origin O, Cartesian coordinates (x_1,x_2,x_3), and the position vector of a point P relative to O in this frame is $\boldsymbol{x}$. The independent

variables are therefore (x_1, x_2, x_3, t).

2) The intrinsic or surface-fitted frame, based on a patch of the surface S, has origin O' and orthogonal curvilinear coordinates (ξ_1, ξ_2, n). The origin O' is any point of S that is well-defined (i.e., chosen with no ambiguity) and remains on S for all time. The parametric surface coordinates ξ_1 and ξ_2 are along the principal directions on the surface S (i.e., they are aligned with the principal directions of curvature) and n is normal distance from S, with $n > 0$ in the direction of the unit outward normal $\boldsymbol{n}$ on S. This frame has independent variables (ξ_1, ξ_2, n, t) and time t is the same in both frames.

The surface S has parametric equation $\boldsymbol{x} = \boldsymbol{X}(\xi_1, \xi_2, t)$ in the Eulerian frame, and the position vector of an arbitrary point P can be written in both the Eulerian and surface-fitted coordinate systems as

$$\boldsymbol{x} = \boldsymbol{X}(\xi_1, \xi_2, t) + n\boldsymbol{n}(\xi_1, \xi_2, t)\,, \tag{C.4}$$

which defines the coordinate transformation between the two frames. The notation and terminology are the same as in, for example, [4]. Let Q be the projection of P onto S in the normal direction. Then Q has position vector given by the equation of S in the Eulerian frame, $\boldsymbol{x} = \boldsymbol{X}(\xi_1, \xi_2, t)$, while in the surface fitted frame Q has coordinates $(\xi_1, \xi_2, n = 0)$ and P has coordinates (ξ_1, ξ_2, n). A sketch of the Eulerian and surface-fitted frames together with their coordinates is shown in Figure C.1.

In the Eulerian frame, the material derivative (i.e., the time derivative following the path of a fluid particle) is

$$\frac{D}{Dt} = \left.\frac{\partial}{\partial t}\right|_{\boldsymbol{x}} + \boldsymbol{u} \cdot \nabla\,. \tag{C.5}$$

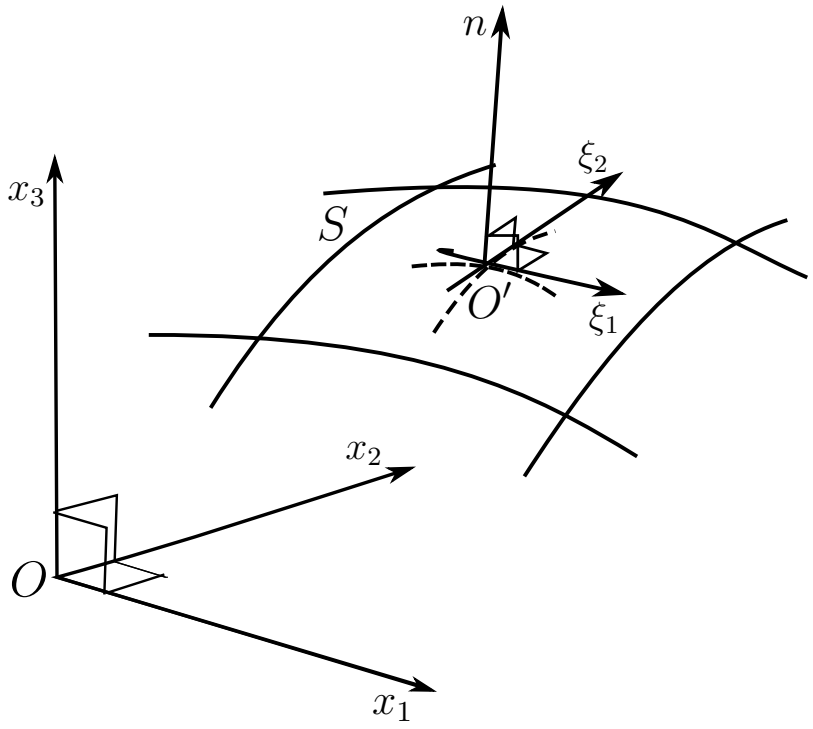

Figure C.1 The (fixed) Eulerian frame has origin O and Cartesian coordinates (x_1, x_2, x_3). A patch of the surface S is shown, with the origin O' of the intrinsic or surface-fitted frame, which lies on S for all time. This frame has orthogonal curvilinear coordinates (ξ_1, ξ_2, n), and the sketch shows the directions of the associated surface-fitted unit vector triad $(\boldsymbol{e}_1, \boldsymbol{e}_2, \boldsymbol{n})$ at O'.

Here and elsewhere, a bar and subscript are used to indicate quantities that are held fixed when a partial derivative is taken. So that $\partial_t|_{\boldsymbol{x}}$ is the familiar partial derivative with respect to time t with the position $\boldsymbol{x}$ of P fixed in space, and the $\boldsymbol{u} \cdot \nabla$ term accounts for its modification to become the time derivative along the path of a fluid particle, which is given by $\frac{d}{dt}\boldsymbol{x} = \boldsymbol{u}(\boldsymbol{x}, t)$.

In the surface-fitted frame, the time derivative $\partial_t|_{\boldsymbol{x}}$ is given by application of the chain rule as

$$\left.\frac{\partial}{\partial t}\right|_{\boldsymbol{x}} = \left.\frac{\partial}{\partial t}\right|_{\boldsymbol{\xi},n} + \left.\frac{\partial \xi_1}{\partial t}\right|_{\boldsymbol{x}} \frac{\partial}{\partial \xi_1} + \left.\frac{\partial \xi_2}{\partial t}\right|_{\boldsymbol{x}} \frac{\partial}{\partial \xi_2} + \left.\frac{\partial n}{\partial t}\right|_{\boldsymbol{x}} \frac{\partial}{\partial n}\,. \tag{C.6}$$

On the right-hand side, bars and subscripts have been omitted on partial derivatives that are taken in the surface-fitted frame except for the first term, $\partial_t|_{\boldsymbol{\xi},n}$, which is multiplied by $\frac{\partial t}{\partial t}|_{\boldsymbol{x}} = 1$. So, for example, ∂_{ξ_1} is taken with ξ_2, n, and t fixed, and ∂_n is taken with ξ_1, ξ_2, and t fixed.

The terms $\partial_t \xi_i|_{\boldsymbol{x}}$ $(i = 1, 2)$ on the right-hand side of (C.6) are found by taking the partial derivative of (C.4) with respect to time keeping the position $\boldsymbol{x}$ of P fixed. This gives

$$\mathbf{0} = \frac{\partial \boldsymbol{X}}{\partial \xi_1} \left.\frac{\partial \xi_1}{\partial t}\right|_{\boldsymbol{x}} + \frac{\partial \boldsymbol{X}}{\partial \xi_2} \left.\frac{\partial \xi_2}{\partial t}\right|_{\boldsymbol{x}} + \left.\frac{\partial \boldsymbol{X}}{\partial t}\right|_{\boldsymbol{\xi}} + \left.\frac{\partial n}{\partial t}\right|_{\boldsymbol{x}} \boldsymbol{n} + n \left(\frac{\partial \boldsymbol{n}}{\partial \xi_1} \left.\frac{\partial \xi_1}{\partial t}\right|_{\boldsymbol{x}} + \frac{\partial \boldsymbol{n}}{\partial \xi_2} \left.\frac{\partial \xi_2}{\partial t}\right|_{\boldsymbol{x}} + \left.\frac{\partial \boldsymbol{n}}{\partial t}\right|_{\boldsymbol{\xi}} \right). \tag{C.7}$$

Since ξ_1 and ξ_2 are aligned with the principal directions on the patch of the surface S, they define an orthogonal coordinate system on it, with orthogonal unit vectors $\boldsymbol{e}_1$ and $\boldsymbol{e}_2$, tangential to S, that are given by

$$\frac{\partial \boldsymbol{X}}{\partial \xi_i} = a_i \, \boldsymbol{e}_i \quad \text{where} \quad a_i = \left| \frac{\partial \boldsymbol{X}}{\partial \xi_i} \right| \quad \text{and } i = 1 \text{ or } 2\,. \tag{C.8}$$

The orthogonal unit vector triad of the surface-fitted frame is given by including the unit normal $\boldsymbol{n} = \boldsymbol{e}_1 \times \boldsymbol{e}_2$. Rodrigues' formula gives the principal curvatures κ_i via

$$\frac{\partial \boldsymbol{n}}{\partial \xi_i} = \kappa_i \frac{\partial \boldsymbol{X}}{\partial \xi_i} = a_i \, \kappa_i \, \boldsymbol{e}_i\,, \quad i = 1, 2\,. \tag{C.9}$$

The relations (C.8) and (C.9) imply that equation (C.7) can be recast as

$$\mathbf{0} = a_1(1 + \kappa_1 n)\, \boldsymbol{e}_1 \left.\frac{\partial \xi_1}{\partial t}\right|_{\boldsymbol{x}} + a_2(1 + \kappa_2 n)\, \boldsymbol{e}_2 \left.\frac{\partial \xi_2}{\partial t}\right|_{\boldsymbol{x}} + \left.\frac{\partial \boldsymbol{X}}{\partial t}\right|_{\boldsymbol{\xi}} + \left.\frac{\partial n}{\partial t}\right|_{\boldsymbol{x}} \boldsymbol{n} + n \left.\frac{\partial \boldsymbol{n}}{\partial t}\right|_{\boldsymbol{\xi}}. \tag{C.10}$$

Since the differential relation for change in position between the two frames is

$$d\boldsymbol{x} = l_1 d\xi_1 \, \boldsymbol{e}_1 + l_2 d\xi_2 \, \boldsymbol{e}_2 + dn \, \boldsymbol{n} \quad \text{where } l_i = a_i(1 + \kappa_i n)\,, \quad i = 1, 2\,, \tag{C.11}$$

equation (C.10) can be rewritten as

$$l_1 \boldsymbol{e}_1 \left.\frac{\partial \xi_1}{\partial t}\right|_{\boldsymbol{x}} + l_2 \boldsymbol{e}_2 \left.\frac{\partial \xi_2}{\partial t}\right|_{\boldsymbol{x}} = - \left.\frac{\partial \boldsymbol{X}}{\partial t}\right|_{\boldsymbol{\xi}} - n \left.\frac{\partial \boldsymbol{n}}{\partial t}\right|_{\boldsymbol{\xi}} - \boldsymbol{n} \left.\frac{\partial n}{\partial t}\right|_{\boldsymbol{x}} . \tag{C.12}$$

On the right-hand side, $\partial_t \boldsymbol{X}|_{\boldsymbol{\xi}}$ has both normal and tangential components in general, and since $\boldsymbol{n}$ is a unit normal $\partial_t \boldsymbol{n}|_{\boldsymbol{\xi}}$ is in the tangent plane.

In the surface-fitted frame the gradient operator is

$$\nabla = \nabla_t + \frac{\partial}{\partial n}\boldsymbol{n} \quad \text{where} \quad \nabla_t = \frac{1}{l_1}\boldsymbol{e}_1 \frac{\partial}{\partial \xi_1} + \frac{1}{l_2}\boldsymbol{e}_2 \frac{\partial}{\partial \xi_2} . \tag{C.13}$$

and ∇_t is the tangential gradient operator. When the dot product of ∇_t and equation (C.12) has been formed, the right-hand side of (C.6) can be written as

$$\left.\frac{\partial}{\partial t}\right|_{\boldsymbol{x}} = \left.\frac{\partial}{\partial t}\right|_{\boldsymbol{\xi},n} + \left(- \left.\frac{\partial \boldsymbol{X}}{\partial t}\right|_{\boldsymbol{\xi}} - n \left.\frac{\partial \boldsymbol{n}}{\partial t}\right|_{\boldsymbol{\xi}} \right) \cdot \nabla_t + \left.\frac{\partial n}{\partial t}\right|_{\boldsymbol{x}} \frac{\partial}{\partial n} . \tag{C.14}$$

Since the position $\boldsymbol{x}$ of P is fixed in the Eulerian frame, $\partial_t n|_{\boldsymbol{x}} = -u_n$ where u_n is the normal speed of S in the Eulerian frame, and if S is the interface between immiscible fluids this is also the normal speed of the fluid on S. The fluid velocity $\boldsymbol{u}$ at P can be expressed in terms of its tangential and normal projections as $\boldsymbol{u} = \boldsymbol{u}_t + u_p \boldsymbol{n}$, where $\boldsymbol{u}_t$ is the tangential projection and u_p is the normal component. Hence, from relation (C.13), $\boldsymbol{u} \cdot \nabla = \boldsymbol{u}_t \cdot \nabla_t + u_p \partial_n$ with the derivatives on the right-hand side taken in the surface-fitted frame. The material derivative (C.5), with all derivatives expressed in the surface-fitted frame, is therefore

$$\frac{D}{Dt} = \left.\frac{\partial}{\partial t}\right|_{\boldsymbol{\xi},n} + \left(\boldsymbol{u}_t - \left.\frac{\partial \boldsymbol{X}}{\partial t}\right|_{\boldsymbol{\xi}} - n \left.\frac{\partial \boldsymbol{n}}{\partial t}\right|_{\boldsymbol{\xi}} \right) \cdot \nabla_t + (u_p - u_n) \frac{\partial}{\partial n} , \tag{C.15}$$

which is exact. Here, $u_p - u_n \equiv v_p$ is the normal component of the fluid velocity at P relative to S or, more specifically, relative to the normal projection Q of P onto S.

Now construct a leading order approximation when the material derivative acts on a scalar quantity that has a large $\mathcal{O}(\epsilon^{-1})$ gradient in the normal direction adjacent

to S. First consider the normal derivative term $(u_p - u_n)\partial_n = v_p\partial_n$ of relation (C.15), and put $n = \epsilon N$ with the rescaled normal coordinate $N = \mathcal{O}(1)$. If S is a material interface then v_p is zero on S and can be approximated by the first non-zero term of its Taylor expansion near S, which is $\partial_n v_p|_s n = \mathcal{O}(\epsilon)$ with error $\mathcal{O}(\epsilon^2)$, and $\partial_n v_p|_s$ is evaluated on S, i.e., where $n = 0$. The quantitiy $\partial_n v_p|_s n = \epsilon\partial_n v_p|_s N$ multiplies the large normal gradient $\partial_n = \epsilon^{-1}\partial_N$, and the product is $\partial_n v_p|_s N\partial_N$, which is of order $\mathcal{O}(1)$. Next consider the term in relation (C.15) that contains the tangential gradient operator ∇_t. If the tangential fluid velocity $\boldsymbol{u}_t$ does not have a large normal gradient it can be approximated by its value $\boldsymbol{u}_s$ on S with error $\mathcal{O}(\epsilon)$, and the term containing $\partial_t \boldsymbol{n}|_{\boldsymbol{\xi}}$ is small like ϵ since n is too. From definition (C.13), the tangential gradient operator ∇_t can also be expanded, as $\nabla_t = \nabla_s + \mathcal{O}(\epsilon)$, where the surface gradient ∇_s is defined by

$$\nabla_s = \frac{1}{a_1}\frac{\partial}{\partial\xi_1}\boldsymbol{e}_1 + \frac{1}{a_2}\frac{\partial}{\partial\xi_2}\boldsymbol{e}_2\,. \tag{C.16}$$

This gives the leading order approximation of the material derivative (C.15), namely

$$\frac{D}{Dt} = \left.\frac{\partial}{\partial t}\right|_{\boldsymbol{\xi},n} + \boldsymbol{v}_s\cdot\nabla_s + \left.\frac{\partial v_p}{\partial n}\right|_S N\frac{\partial}{\partial N} + \mathcal{O}(\epsilon)\,,\ \text{where}\ \ \boldsymbol{v}_s \equiv \boldsymbol{u}_s - \left.\frac{\partial \boldsymbol{X}}{\partial t}\right|_{\boldsymbol{\xi}}\,. \tag{C.17}$$

Here $\boldsymbol{v}_s$ and $\partial_n v_p|_s$ are both functions of $\boldsymbol{\xi} = (\xi_1, \xi_2)$ and t alone. Recall that $\boldsymbol{u}_s$ is tangential to S, and since $\partial_t \boldsymbol{X}|_{\boldsymbol{\xi}}$ and $\boldsymbol{v}_s$ are projected onto ∇_s only their tangential components contribute to the material derivative. As shown in [4], $\partial_n v_p|_s$, which is the rate of extension of an infinitesimal fluid line element based on S that is normal to S, can be evaluated in terms of surface data by using the incompressibility condition, $\nabla\cdot\boldsymbol{u} = 0$. To be specific, in three space dimensions,

$$\left.\frac{\partial v_p}{\partial n}\right|_S = -(\kappa_1 + \kappa_2)u_n - \nabla_s\cdot\boldsymbol{u}_s\,. \tag{C.18}$$

Comparison with the Material Derivative and Evolution on a Surface.

To compare component terms in the material derivative (C.17) to terms in the conservation law for evolution of a quantity that is confined to S, such as the surface concentration of surfactant Γ when it is insoluble and therefore has no bulk-interface exchange, we refer to [36].

It is shown in [36] (at equation (7)) that the time derivative $\partial_t\Gamma|_n$ along a path that is normal to S is related to the time derivative $\partial_t\Gamma|_{\boldsymbol{\xi}}$ in an arbitrary system of orthogonal surface coordinates along a path with $\boldsymbol{\xi} = (\xi_1, \xi_2)$ fixed by

$$\left.\frac{\partial\Gamma}{\partial t}\right|_n = \left.\frac{\partial\Gamma}{\partial t}\right|_{\boldsymbol{\xi}} - \left.\frac{\partial \boldsymbol{X}}{\partial t}\right|_{\boldsymbol{\xi}} \cdot \nabla_s\Gamma\,, \tag{C.19}$$

or as an operator

$$\left.\frac{\partial}{\partial t}\right|_n = \left.\frac{\partial}{\partial t}\right|_{\boldsymbol{\xi}} - \left.\frac{\partial \boldsymbol{X}}{\partial t}\right|_{\boldsymbol{\xi}} \cdot \nabla_s\,. \tag{C.20}$$

To cross-refer, what we have just called a path that is normal to S is referred to in [36], first paragraph, as a path with ("fixed") surface coordinates that advance only normal to the surface. Also, in [36] the notation $[\partial_t\Gamma]_n$ is used to denote the time derivative along the normal path, and the surface coordinates are denoted by $\bar{u}_1$ and $\bar{u}_2$, so that equation (7) of [36] is in fact

$$\left[\frac{\partial\Gamma}{\partial t}\right]_n = \left[\frac{\partial\Gamma}{\partial t}\right]_{\overline{u}} - \dot{\boldsymbol{X}} \cdot \nabla_s\Gamma\,, \tag{C.21}$$

where $\dot{\boldsymbol{X}} \equiv \partial_t \boldsymbol{X}|_{\overline{\boldsymbol{u}}}$.

In the present notation, of equation (C.19), the conservation law for Γ in a form that includes reference to the surface parameterization is (see [36], equation (8))

$$\left.\frac{\partial\Gamma}{\partial t}\right|_{\boldsymbol{\xi}} - \left.\frac{\partial \boldsymbol{X}}{\partial t}\right|_{\boldsymbol{\xi}} \cdot \nabla_s\Gamma + \Gamma(\kappa_1+\kappa_2)u_n + \nabla_s\cdot(\Gamma\boldsymbol{u}_s) = D_s\nabla_s^2\Gamma\,, \tag{C.22}$$

or equivalently in coordinate-free form via (C.19)

$$\left.\frac{\partial\Gamma}{\partial t}\right|_n + \Gamma(\kappa_1+\kappa_2)u_n + \nabla_s\cdot(\Gamma\boldsymbol{u}_s) = D_s\nabla_s^2\Gamma \;\text{ on } S\,. \tag{C.23}$$

We can now compare terms in the material derivative (C.17), which holds for a volumetric quantity in a boundary layer adjacent to S, to derivative terms acting on Γ on the left-hand side of equations (C.22) and (C.23). First, to recover the material derivative of a surface quantity from (C.17) the normal coordinate $n = \epsilon N = 0$ is fixed and variation in the normal direction is removed, so that $\partial_N = 0$, the $\mathcal{O}(\epsilon)$ remainder is absent, and the time derivative $\partial_t|_{\boldsymbol{\xi},n} = \partial_t|_{\boldsymbol{\xi}}$. The material derivative of a surface quantity can therefore be expressed in equivalent ways as

$$\frac{D}{Dt} = \left.\frac{\partial}{\partial t}\right|_{\boldsymbol{\xi}} + \boldsymbol{v}_s \cdot \nabla_s \,, \tag{C.24a}$$

$$= \left(\left.\frac{\partial}{\partial t}\right|_{\boldsymbol{\xi}} - \left.\frac{\partial \boldsymbol{X}}{\partial t}\right|_{\boldsymbol{\xi}} \cdot \nabla_s \right) + \boldsymbol{u}_s \cdot \nabla_s \,, \tag{C.24b}$$

$$= \left.\frac{\partial}{\partial t}\right|_{n} + \boldsymbol{u}_s \cdot \nabla_s \,. \tag{C.24c}$$

Of these expressions (C.24a) has been recovered directly from the material derivative at (C.17), (C.24b) follows from the definition that $\boldsymbol{v}_s \equiv \boldsymbol{u}_s - \partial_t \boldsymbol{X}|_{\boldsymbol{\xi}}$, and (C.24c) follows from the equivalence at (C.20).

This can be used to confirm our interpretation of the conservation law (C.22) or (C.23) for Γ. From the form of the surface material derivative at (C.24c) and the vector identity for the surface divergence that $\nabla_s \cdot (\phi \boldsymbol{u}_s) = \boldsymbol{u}_s \cdot \nabla_s \phi + \phi \nabla_s \cdot \boldsymbol{u}_s$ for a scalar ϕ and surface vector field $\boldsymbol{u}_s$, the conservation law can be written as

$$\frac{D\Gamma}{Dt} + \Gamma \left(\nabla_s \cdot \boldsymbol{u}_s + (\kappa_1 + \kappa_2) u_n \right) = D_s \nabla^2 \Gamma \,. \tag{C.25}$$

Here, the quantity $\nabla_s \cdot \boldsymbol{u}_s + (\kappa_1 + \kappa_2) u_n$ represents the net time rate of change of area of an infinitesimal Lagrangian surface element, i.e., an infinitesimal area element that consists of material particles on the interface. It is caused by 'sources' or the surface divergence of the tangential fluid velocity $\boldsymbol{u}_s$ and by the motion of the interface along its normal when the mean curvature $(\kappa_1 + \kappa_2)/2$ is non-zero. As seen from equation (C.18), for a fluid that is incompressible this rate of area change is of equal magnitude

and opposite sign to the rate of extension of a Lagrangian line element that is normal to the interface.

C.3 The Order of Accuracy of the Time Step

The time evolution of $\boldsymbol{z}$ and C is given by equation (4.28) of Section 4.3, which are

$$\partial_t \boldsymbol{z} = \boldsymbol{R}(\boldsymbol{z}, \partial_n C|_S)\,, \tag{C.26a}$$

$$\partial_t C = S(\boldsymbol{z}, C) + F(\boldsymbol{z}, C)\,. \tag{C.26b}$$

The discretization for the time step is given by equation (4.29) for the first or predictor step, which are

$$\widetilde{\boldsymbol{z}}^{n+1} = \boldsymbol{z}^n + \Delta t\, \boldsymbol{R}(\boldsymbol{z}^n, \partial_n C|_S^n)\,, \tag{C.27a}$$

$$\widetilde{C}^{n+1} = C^n + \Delta t\, (S(\boldsymbol{z}^n, C^n) + F(\boldsymbol{z}^n, \widetilde{C}^{n+1}))\,, \tag{C.27b}$$

and by equations (4.30) for the second or corrector step, which are

$$\boldsymbol{z}^{n+1} = \boldsymbol{z}^n + \frac{\Delta t}{2}\left(\boldsymbol{R}(\boldsymbol{z}^n, \partial_n C|_S^n) + \boldsymbol{R}(\widetilde{\boldsymbol{z}}^{n+1}, \partial_n \widetilde{C}|_S^{n+1})\right)\,, \tag{C.28a}$$

$$C^{n+1} = C^n + \frac{\Delta t}{2}\Big(S(\boldsymbol{z}^n, C^n) + S(\widetilde{\boldsymbol{z}}^{n+1}, \widetilde{C}^{n+1}) + F(\boldsymbol{z}^n, C^n) + F(\widetilde{\boldsymbol{z}}^{n+1}, C^{n+1})\Big)\,, \tag{C.28b}$$

where the indices i and j of the spatial coordinates have been omitted, as they will be throughout this section since they are fixed for each mesh point during the time step.

As noted in the main text, the time step for $\boldsymbol{z}$ uses Heun's method, which is second order accurate in time [3]. It turns out that the same result holds for the time step for C, which follows similar reasoning. Both results are shown here.

Taylor expansion of the functionals $\boldsymbol{R}$, S, and F using the predictor step (C.27) shows that for the following components that appear in the corrector step, we have

$$\begin{aligned}
\boldsymbol{R}(\widetilde{\boldsymbol{z}}^{n+1}, \partial_n \widetilde{C}|_S^{n+1}) &= \boldsymbol{R}(\boldsymbol{z}^n, \partial_n C|_S^n) + \boldsymbol{R}(\boldsymbol{z}^n, \partial_n C|_S^n) \cdot \nabla_{\boldsymbol{z}} \boldsymbol{R}|_{\boldsymbol{z}_n, C_n} \Delta t \\
&\quad + \partial_C \boldsymbol{R}|_{\boldsymbol{z}_n, C_n} (S(\boldsymbol{z}^n, C^n) + F(\boldsymbol{z}^n, C^n)) \Delta t + O(\Delta t^2) \\
&= \boldsymbol{R}(\boldsymbol{z}^n, \partial_n C|_S^n) + \left. \frac{\partial^2 \boldsymbol{z}}{\partial t^2} \right|_{t_n} \Delta t + O(\Delta t^2)\,, \qquad \text{(C.29a)} \\
S(\widetilde{\boldsymbol{z}}^{n+1}, \widetilde{C}^{n+1}) &= S(\boldsymbol{z}^n, C^n) + \boldsymbol{R}(\boldsymbol{z}^n, \partial_n C|_S^n) \cdot \nabla_{\boldsymbol{z}} S|_{\boldsymbol{z}_n, C_n} \Delta t \\
&\quad + \partial_C S|_{\boldsymbol{z}_n, C_n} (S(\boldsymbol{z}^n, C^n) + F(\boldsymbol{z}^n, C^n)) \Delta t + O(\Delta t^2) \\
&= S(\boldsymbol{z}^n, C^n) + \left. \frac{\partial S}{\partial t} \right|_{t_n} \Delta t + O(\Delta t^2)\,, \qquad \text{(C.29b)} \\
\text{and } F(\widetilde{\boldsymbol{z}}^{n+1}, C^{n+1}) &= F(\boldsymbol{z}^n, C^n) + \left. \frac{\partial F}{\partial t} \right|_{t_n} \Delta t + O(\Delta t^2)\,, \qquad \text{(C.29c)}
\end{aligned}$$

where equation (C.26a) has been used to simplify the result at equation (C.29a). When these expressions are substituted into the corrector step (C.28), and the exact equations (C.26) and their time derivatives are used, we have

$$\begin{aligned}
\boldsymbol{z}^{n+1} &= \boldsymbol{z}^n + \left. \frac{\partial \boldsymbol{z}}{\partial t} \right|_{t_n} \Delta t + \left. \frac{\partial^2 \boldsymbol{z}}{\partial t^2} \right|_{t_n} \frac{\Delta t^2}{2} + O(\Delta t^3)\,, \qquad \text{(C.30a)} \\
C^{n+1} &= C^n + \left. \frac{\partial C}{\partial t} \right|_{t_n} \Delta t + \left. \frac{\partial^2 C}{\partial t^2} \right|_{t_n} \frac{\Delta t^2}{2} + O(\Delta t^3)\,. \qquad \text{(C.30b)}
\end{aligned}$$

Here the terms on the right-hand side up to and including order $O(\Delta t^2)$ are the same as those of the Taylor expansion of the exact solution at time $t_{n+1} = t_n + \Delta t$ about $t = t_n$, so the method is shown to have local accuracy of second order at each time step.

BIBLIOGRAPHY

[1] N. J. Alvarez, W. Lee, L. M. Walker, and S. L. Anna. The effect of alkane tail length of C_iE_8 surfactants on transport to the silicone oil-water interface. *Journal of Colloid and Interface Science.*, 355:231–236, 2011.

[2] S. L. Anna. Droplets and bubbles in microfluidic devices. *Annual Review of Fluid Mechanics*, 48:285–309, 2016.

[3] K. E. Atkinson. *An Introduction to Numerical Analysis.* 2nd Edition, New York, NY: Wiley, 1998.

[4] M. R. Booty and M. Siegel. A hybrid numerical method for interfacial fluid flow with soluble surfactant. *Journal of Computational Physics*, 229:3864–3883, 2010.

[5] G. F. Carrier, M. Krook, and C. E. Pearson. *Functions of a Complex Variable: Theory and Technique.* Classics in Applied Mathematics, Vol. 49. Philadelphia, PA: SIAM, 2005. Originally published by McGraw-Hill, New York, 1966.

[6] C.-H. Chang and E. I. Franses. Adsorption dynamics of surfactants at the air/water interface: A critical review of mathematical models, data, and mechanisms. *Colloids and Surfaces A*, 100:1–45, 1995.

[7] A. J. Chorin and J. E. Marsden. *A Mathematical Introduction to Fluid Mechanics.* Texts in Applied Mathematics, Vol. 4. (3rd Edition) New York, NY: Springer, 1993.

[8] P.-G. de Gennes, F. Brochard-Wyatt, and D. Quéré. *Capillarity and Wetting Phenomena; Drops, Bubbles, Pearls, Waves.* New York, NY and Heidelberg, Germany: Springer, 2004.

[9] T. K. Delillo. The accuracy of numerical conformal mapping methods: a survey of examples and results. *SIAM Journal of Numerical Analysis*, 31(3):788–812, 1994.

[10] J. Eastoe and J. S. Dalton. Dynamic surface tension and adsorption mechanisms of surfactants at the air/water interface. *Advances in Colloid and Interface Science*, 85:103–144, 2000.

[11] D. A. Edwards, H. Brenner, and D. T. Wasan. *Interfacial Transport Processes and Rheology.* Boston, MA: Butterworth-Heinemann, 1991.

[12] B. Fornberg. *A Practical Guide to Pseudospectral Methods.* Cambridge, UK: Cambridge University Press, 1996.

[13] J. S. Hadamard. Mouvement permanent lent d'une sphere liquide et visqueuse dans un liquide visqueux. *Comptes Rendus de l'Académie des Sciences*, 152:1735–1738, 1911.

[14] N. D. Halsey. Comparison of the convergence characteristics of two conformal mapping methods. *AIAA Journal*, 20:724–726, 1982.

[15] T. Y. Hou, J. Lowengrub, and R. Krasny. Convergence of a point vortex method for vortex sheets. *SIAM Journal of Numerical Analysis*, 28(2):308–320, 1991.

[16] T. Y. Hou, J. S. Lowengrub, and M. J. Shelley. Removing the stiffness from interfacial flows with surface tension. *Journal of Computational Physics*, 114:312–338, 1994.

[17] R. M. James. A new look at two-dimensional incompressible airfoil theory. *Douglas Aircraft Co., Long Beach, CA., Technical Report*, J0918/01, 1971.

[18] J. J. M. Janssen, A. Boon, and W. G. M. Agterof. Influence of dynamic interfacial properties on droplet breakup in simple shear flow. *AIChE Journal*, 40(12):1929–1939, 1994.

[19] M. C. A. Kropinski. An efficient numerical method for studying interfacial motion in two-dimensional creeping flows. *Journal of Computational Physics*, 171:479–508, 2001.

[20] P. K. Kythe. *Computational Conformal Mapping*. Boston, MA: Birkhäuser, 1998.

[21] W. E. Langlois and M. O. Deville. *Slow Viscous Flow*. 2nd Edition, New York, NY: Springer International Publishing, 2014. First edition (W. E. Langlois) published by MacMillan, New York, 1964.

[22] L.G. Leal. *Laminar flow and convective transport processes: scaling principles and asymptotic analysis*. Boston, MA: Butterworth-Heinemann, 1992.

[23] C. C. Lin and L. A. Segel. *Mathematics Applied to Deterministic Problems in the Natural Sciences*. Classics in Applied Mathematics, Vol. 1. Philadelphia, PA: SIAM, 1988. Originally published by MacMillan Publishing Co., New York, 1974.

[24] S. G. Mikhlin. *Integral Equations and Their Applications to Certain Problems in Mechanics, Mathematical Physics, and Technology*. New York, NY: Pergamon Press, 1957.

[25] N. I. Muskhelishvili. *Some Basic Problems of the Mathematical Theory of Elasticity*. 2nd Edition, Groningen, The Netherlands: P. Noordhof, 1963.

[26] C. Pozrikidis. *Boundary Integral and Singularity Methods for Linearized Viscous Flow*. Cambridge, UK: Cambridge University Press, 1992.

[27] J. M. Rallison. The deformation of small viscous drops and bubbles in shear flows. *Annual Review of Fluid Mechanics*, 16:45–66, 1984.

[28] Ceresana Research. *Market Study on Surfactants*. 3rd Edition, Konstanz, Germany: Ceresana Publications, 2017.

[29] W. Rybczynski. Über die fortschreitende bewegung einer flüssigen kugel in einem zähen medium. *Bulletin International de l'Académie des Sciences de Cracovie, A*, pages 40–46, 1911.

[30] L. A. Segel. *Mathematics Applied to Continuum Mechanics*. Classics in Applied Mathematics, Vol. 52. Philadelphia, PA: SIAM, 2007. Originally published by MacMillan Publishing Co., New York, 1977.

[31] H. A. Stone. Dynamics of drop deformation and breakup in viscous fluids. *Annual Review of Fluid Mechanics*, 26:65–102, 1994.

[32] G. I. Taylor. The formation of emulsions in definable fields of flow. *Proceedings of the Royal Society of London, Series A*, 146:501–523, 1934.

[33] T. Theodorsen and I. E. Garrick. General potential theory of arbitrary wing sections. *National Advisory Committee for Aeronautics, Technical Report*, 452, 1933.

[34] L. N. Trefethen. *Spectral Methods in MATLAB*. Philadelphia, PA: SIAM, 2000.

[35] L. N. Trefethen and J. A. C. Weideman. The exponentially convergent trapezoidal rule. *SIAM Review*, 56(3):385–458, 2014.

[36] H. Wong, D. Rumschitzki, and C. Maldarelli. On the surfactant mass balance at a deforming fluid interface. *Physics of Fluids*, 8(11):3203–3204, 1996.

[37] J. K. Wrobel, M. R. Booty, M. Siegel, and Q. Wang. Simulation of surfactant-mediated tipstreaming in a flow-focusing geometry. *Physical Review Fluids*, 3(114003):1–29, 2018.

[38] K. Xu. *Computational Methods for Two-Phase Flow with Soluble Surfactant*. Ph.D. dissertation, Mathematical Sciences, New Jersey Institute of Technology, Newark, New Jersey, 2010.

[39] K. Xu, M. R. Booty, and M. Siegel. Analytical and computational methods for two-phase flow with soluble surfactant. *SIAM Journal of Applied Mathematics*, 73(1):523–548, 2013.